Doctorate Dissertation

博士論文

Demonstration of the muon acceleration with Radio-Frequency Quadrupole linac

(RFQ線形加速器を用いたミューオン加速の実証実験)

A Dissertation Submitted for Degree of Doctor of Philosophy
July 2018

平成 30 年 7 月博士（理学）申請

Department of Physics, Graduate School of Science
The University of Tokyo

東京大学大学院理学系研究科物理学専攻

Ryo Kitamura

北村　遼

Demonstration of the muon acceleration with Radio-Frequency Quadrupole linac

Ryo Kitamura

Department of Physics
University of Tokyo
July, 2018

Dissertation Committee:

S. Yamashita
T. Koseki
T. Mori
I. Tsutsui
and M. Yokoyama

Abstract

A low-emittance muon beam is expected to provide many attractive applications and to develop new scientific fields. For example, a precision measurement of the muon dipole moments using the low-emittance muon beam is proposed to search a new physics beyond the standard model. In this proposed measurement, both magnetic and electric moments are measured at the same time thanks to the low emittance of the muon beam in the storage field.

To realize the low-emittance muon beam, the cooling from a conventional muon beam with the large emittance and the subsequent radio-frequency (RF) acceleration are necessary. We developed a low-energy muon source to demonstrate this acceleration scheme in a timely manner.

A negative muonium ion (Mu^-, μ^+ e^-e^-) source satisfies the requirement of this low-energy muon source, because the initial kinetic energy of the Mu^- is sufficiently small to demonstrate the acceleration from the zero energy. In addition, the Mu^- is easily produced with a thin aluminum foil target (Al target). However, the production yield of the Mu^- should be measured to estimate the event rate of the accelerated Mu^- in the muon acceleration experiment. Then, a new measurement system was developed to identify the Mu^- beam clearly with a Time-Of-Flight (TOF) measurement. A lot of backgrounds are suppressed with the TOF measurement, considering the pulsed muon beam in the Japan Proton Accelerator Research Complex (J-PARC).

The production efficiency of the Mu^- from the Al target was measured with the developed measurement system. The Mu^- was extracted from the Al target with an electrostatic accelerator and transported with a beam line including an electrostatic deflector and a bending magnet, then detected with a micro-channel plate (MCP) detector. The time difference between the collision time of the incident muon at the Al target and the detection time of the Mu^- at the MCP was defined as the TOF. The clear signal of the Mu^- was obtained with the TOF measurement and the kinetic-energy and momentum selections using the electrostatic deflector and the bending magnet to suppress the backgrounds. The measured event rate of the Mu^- was $(1.7 \pm 0.3) \times 10^{-3}$ /s. From these results the well-defined Mu^- source was developed for the muon RF acceleration.

Next, the demonstration of the muon RF acceleration with an radio-frequency quadrupole (RFQ) linac was carried out using this developed Mu^- source. The RFQ is an accelerating structure dedicated to low-energy particles. The accelerated Mu^- was clearly identified with the TOF measurement and the momentum selection with the bending magnet to suppress the backgrounds. The clear signal was observed with the TOF measurement, when the RF power of the RFQ was turned on. On the other hand, no significant signal was observed, when the RF power was turned off. The measured event rate of the accelerated Mu^- was $(5.1 \pm 0.8) \times 10^{-4}$ /s, while the expected event rate of the accelerated Mu^- was $(6.8 \pm 1.2) \times 10^{-4}$ /s from the result of the Mu^- production experiment. Therefore, the measured event rate of the accelerated Mu^- was consistent with the expectation. From these results, we conclude that the Mu^- was exactly accelerated with the RFQ. This is the first muon RF acceleration in the world.

This result is the important milestone to realize the low-emittance muon beam and the precision measurement of the muon dipole moments. The successful demonstration of the muon RF acceleration opens the door for the many interesting applications using the low-emittance muon beam in the various scientific fields.

Acknowledgements

This work was achieved thanks to a great deal of supports from many people. I would like to acknowledge them.

I would like to express my sincere appreciation to Dr. Masashi Otani for his tremendous supports for my research and academic life through these five years. This work was impossible without his many kind efforts and patience. I would like to express my gratitude to Dr. Yasuhiro Kondo for his invaluable advice and contributions to my education.

I am deeply thankful to my supervisor, Prof. N. Saito for providing me with the opportunity to study at this exciting experiment to open a door for the new physics. My thanks to go to Prof. Tsutomu Mibe, Prof. Naritoshi Kawamura, Dr. Takayuki Yamazaki, Prof. Yasuhiro Miyake, Prof. Koichiro Shimomura, Dr. Masahiko Iwasaki, Dr. Katsuhiko Ishida, Dr. Shinji Okada, Dr. Takatoshi Morishita, Dr. Kenta futatsukawa, Dr. Hiromi Iinuma, Dr. Yoshinori Fukao, Dr. Glen Marshall, Dr. Kazuki Ueno and Dr. Ken Sakashita for their many supports and educational advice. I am thankful to Dr. Bongho Kim, Mr Sunghan Bae, Mr. Gosha Razuvaev, Prof. Seonho Choi, Mr. yuki Sue and Mr. Yuuga Nakazawa for their many significant supports and advice for the execution of the experiment. I would like to also thank the J-PARC MUSE and J-PARC linac staffs for the kind supports.

I thanks to Dr. Sotaro Kanda, Mr. Shoichiro Nishimura, Mr. Kohei Hanzawa, Mr. Hiromasa Yasuda, Mr. Sirui Li, Mr. Takahiro Ushizawa, Dr. Yosuke Watanabe, Dr. Taihei Adachi, Dr. Yuuya Komatsu, Mr. Shinichi Masumoto, Mr. Wataru Nakai, Mr. Koki Kanno, Mr. Obara Yuuki, Mr. Takuya Sibukawa, Ms. Hikari Murakami, Mr. Seiya Miyata, Ms. Tomoko Iida, Ms. Kuniko Ohata and Ms. Mayumi Suehiro for the a lot of helps in my academic life.

I thanks her for our good days.

At last but not the least, I would like to express the deepest application to my parents for giving the all their helps and supports.

Contents

Chapter 1

Introduction

1.1 Significance of this dissertation

Significances in this dissertation are following two points;

- We focused on the production of a negative muonium ion (Mu^-, μ^+ e^- e^-) [1] [2] as a low-energy muon source for the muon radio-frequency (RF) acceleration. The measurement system of the Mu^- was developed to measure the event rate of the Mu^-. With this measurement system, the Mu^- was identified using a Time-Of-Flight (TOF) method, considering the feature of the pulsed muon beam. Then the production yield of the Mu^- was measured.

- Using above developed Mu^- source, the RF acceleration of the Mu^- was demonstrated. Since the backgrounds can be suppressed by introducing the TOF measurement, the accelerated Mu^- was clearly identified. The measured event rate of the accelerated Mu^- was consistent with the expectation from the measurement of the Mu^- source.

The RF acceleration of the Mu^- beam was confirmed with above two measurements. In summary, the world first muon RF acceleration is successful [3].

1.2 Low-emittance muon beam

A low-emittance muon beam with the emittance of less than a few π mm mrad is expected to be a powerful tool for researches in various scientific fields. As for the materials and life science such as the condensed matter physics and the chemistry, the method of the muon spin rotation, relaxation and resonance (μSR) has been used for the basic studies [4] [5] [6]. By introducing the muon beam with the lower beam emittance, the more detailed information is expected to be obtained in the studies of the magnetic systems around the surface boundary through this μSR method. For further applications of the muon beam, the muon tomography gathers attention in studies of a homeland security [7] and the radiography for the volcano and the nuclear reactor [8]. For these fields, the low-emittance muon beam is expected to be useful to explore the inner-structures of the large objects.

In the particle physics, a precision measurement of the muon dipole moments [9] and a muon collider [10] [11] are expected to be realized with such the low-emittance muon beam to search for a new physics beyond the standard model (BSM). Particularly, this precision measurement of the muon dipole moments using the low-emittance muon beam is expected to play an important role to explore the BSM. Recently, the discovery of the Higgs boson at the large hadron collider provided the last piece of the puzzle to complete the standard model (SM) [12] [13]. However, unresolved issues in the particle physics still remain as follows; the large CP violation to describe

the matter-antimatter asymmetry of the universe, the hierarchy problem between the weak scale and the plank scale and the dark matter. Considering these issues, the SM is not the ultimate theory and the BSM exists explicitly.

1.3 Measurement of the muon dipole moments

In this section, the importance of the measurement of the muon dipole moments is explained. The non-relativistic Hamiltonian for the spin 1/2 particle in the external electromagnetic fields is described as

$$H = -\vec{\mu} \cdot \vec{B} - \vec{d} \cdot \vec{E}, \tag{1.1}$$

where

$$\vec{\mu} = g\left(\frac{q}{2m}\right)\vec{s} \text{ and} \tag{1.2}$$

$$\vec{d} = \eta\left(\frac{q}{2mc}\right)\vec{s}. \tag{1.3}$$

Here, $\vec{\mu}$ and $\vec{d}$ are magnetic and electric dipole moments of the muon, $\vec{B}$ and $\vec{E}$ are external magnetic and electric fields, g is the muon g factor, η is the dimensionless constant, which is analogous to g, q is the charge, m is the muon mass, c is the speed of light and $\vec{s}$ is the muon spin vector. Although this muon g factor is calculated with the Dirac equation and equal to 2, it is slightly different from 2 because of contributions from the quantum loop effects. This anomalous magnetic moment of the muon $(g-2)_\mu$ is defined as

$$a_\mu \equiv \frac{g-2}{2}. \tag{1.4}$$

On the other hand, the muon electric dipole moment (EDM) is calculated as

$$d_\mu = \left(\frac{\eta}{2}\right)\left(\frac{e\hbar}{2mc}\right), \tag{1.5}$$

where e is the elementary charge and $\hbar$ is the reduced Planck constant. These a_μ and d_μ are derived in the measurement of the muon dipole moments.

The $(g-2)_\mu$ is one of the quantities theoretically predicted with the high precision [14]. The E821 experiment at the Brookhaven National Laboratory (BNL) measured $(g-2)_\mu$ with the precision of 0.54 ppm and reported the discrepancy of more than three standard deviations between the experimental value and the prediction with the SM [15]. Since this discrepancy can be explained to indicate the evidence of the BSM, the more precision measurement has been strongly desired.

As for the EDM, the EDM violates the CP symmetry assuming the CPT invariance, where C, P and T are charge conjugation, parity reversal and time reversal symmetries, respectively. Since the electron EDM in the SM is evaluated as 2×10^{-38} e·cm [16], the muon EDM in the SM will be $\sim 10^{-35}$ e·cm by scaling the ratio of the muon to the electron mass [17]. The muon EDM predicted in the SM is so small that it is difficult to detected experimentally for the foreseeable future. Therefore, the discovery of the any nonzero experimental value for the muon EDM indicates the explicit evidence of the BSM.

Next, the method of the measurement for the $(g-2)_\mu$ and the muon EDM in the BNL E821 is explained. The equation of the angular frequency of the muon spin precession in the electromagnetic fields is described as

$$\vec{\omega} = -\frac{q}{m}\left[a_\mu \vec{B} - \left(a_\mu - \frac{1}{\gamma^2-1}\right)\frac{\vec{\beta}\times\vec{E}}{c} + \frac{\eta}{2}\left(\vec{\beta}\times\vec{B} + \frac{\vec{E}}{c}\right)\right], \tag{1.6}$$

where $\beta = v/c$ and v is the velocity and γ is the Lorentz factor. In equation (1.6), first and second terms represent contributions of the spin precession for the $(g-2)_\mu$ and third and fourth terms represent those for the EDM. In the BNL E821, the muons with the momentum of $p = 3.09$ GeV/c were stored in the storage ring of 14 meters in diameter, applying an uniform storage magnetic field. With this experimental condition, the second term in equation (1.6) vanished because of $a_\mu \simeq 1/(\gamma^2 - 1)$ with this momentum. As for the contributions from the EDM, the third term in equation (1.6) is a dominant contribution for the EDM. This term contributes to the spin precession in the transverse plane with respect to the storage field B. It means that this contribution is the vertical oscillation on the plane of the muon storage ring. To measure the vertical oscillation, the decay positron (or the electron) was measured. The muon decays by the weak interaction which breaks the parity symmetry and emits the decay positron. Since the emission angle of the decay position depends on the direction of the muon spin vector, this vertical oscillation is estimated from the time spectra of up-going and down-going decay positrons. From the measurement of the vertical oscillation, the search for the muon EDM found the null result and obtained a limit of $|d_\mu| < 1.8 \times 10^{-19}$ e·cm (95% C.L.) [18]. Then, when the contribution of the spin precession for the EDM is small, the equation of the angular frequency of the muon spin precession in the BNL E821 is described as

$$\overrightarrow{\omega} = -\frac{q}{m} a_\mu \overrightarrow{B}. \tag{1.7}$$

From the measurement of the time spectrum for the number of the decay positrons, this angular frequency of the muon spin precession ω was measured. Since measures in the BNL E821 were the angular frequency ω and the storage magnetic field B, the a_μ was finally derived from these two measures.

In the measurement of the spin precession, the nonzero muon EDM increases the total angular frequency of the muon spin precession. This total angular frequency of the muon spin precession in the storage field is described as $\overrightarrow{\omega} = \overrightarrow{\omega}_a + \overrightarrow{\omega}_{\mathrm{EDM}}$, where $\overrightarrow{\omega}_a$ and $\overrightarrow{\omega}_{\mathrm{EDM}}$ are contributions of the angular frequencies of the spin precession for the $(g-2)_\mu$ and the EDM, respectively. Therefore, the observed angular frequency enlarges with the muon EDM present and is modified as

$$\omega = \sqrt{\omega_a^2 + \left(\frac{q\eta\beta B}{2m}\right)^2}. \tag{1.8}$$

Equation (1.8) implies that the discrepancy of the $(g-2)_\mu$ can be caused by the muon EDM. This ambiguity can be resolved by the sufficiently precision measurements of both $(g-2)_\mu$ and EDM.

To this end, a new experiment to measure the muon dipole moments more precisely is proposed at the Japan Proton Accelerator Research Complex (J-PARC). This J-PARC E34 experiment aims to measure the $(g-2)_\mu$ with the statistical precision of 0.46 ppm and the muon EDM with the sensitivity of 1.5×10^{-21} e·cm, respectively [9]. When the muons are stored in the storage field without the focusing electric field, second and fourth terms in equation (1.6) vanish. Therefore, with this experimental condition, the total angular frequency of the muon spin precession in the J-PARC E34 is described as

$$\overrightarrow{\omega} = -\frac{q}{m}\left[a_\mu \overrightarrow{B} + \frac{\eta}{2}\left(\overrightarrow{\beta} \times \overrightarrow{B}\right)\right]. \tag{1.9}$$

In equation (1.9), the first and second terms indicate the horizontal and vertical oscillations of the spin precession with respect to the muon storage plain, respectively. These oscillations of the muon spin describe the contributions for the $(g-2)_\mu$ and the muon EDM, respectively. Then, the horizontal and vertical oscillations of the time spectra for the number of the decay positrons are measured to derive the ω_a and the ω_{EDM}. Finally, the a_μ and the d_μ are derived from the

ω_a and the $\omega_{\rm EDM}$. The realization of this new measurement will be the important milestone to search for the BSM. This approach, that is the muon storage without the focusing electric field is achieved using the low-emittance muon beam. Then, the muon beam with the 100 % emittance of less than 1.5 π mm mrad is assumed in the J-PARC E34.

1.4 Earlier studies of the muon cooling

Since the conventional muon beam is produced as the tertiary beam from the proton beam through pion decays, the emittance of this muon beam is intrinsically large. As an earlier study of the muon cooling, for example, the international Muon Ionization Cooling Experiment (MICE) [19] [20] was proposed to cool the muon beam by the energy loss through the ionization in the absorber and restoring the lost energy with the RF acceleration. With the MICE approach, the normalized rms transverse emittance at its equilibrium is about 100π mm mrad, assuming the longitudinal momentum is 200 MeV/c [21] [22]. It is equivalent to the transverse momentum of 7 MeV/c. However, the cooling power is limited with this method to reach the emittance of less than 100π mm mrad, because of the contribution from the multiple scattering. To obtain the low-emittance muon beam with less than a few π mm mrad, the additional cooling is required with this approach.

If the muons can be once cooled to the thermal temperature and then re-accelerated, the lower-emittance muon beam is obtained. This re-acceleration should be rapid, because the muon decays with the mean life time of about 2.2 μs. Then, the linear accelerator is best for the fast acceleration. The low-energy muon source to be acceptable to the RF accelerator is required. As such a cooling method, the production of an ultra-slow positive muon (USM) with the kinetic energy of 0.2 eV has been developed by the KEK group [23]. The conventional muons are converted to a muonium atom (Mu, μ^+ e^-) and subsequently the USM is produced with the laser resonant ionization. If the USM is accelerated with the accelerator to 300 MeV/c, the low-emittance muon beam is obtained with the 100 % transverse emittance of 1.5π mm mrad, that is the transverse momentum of 3 keV/c [9]. Nevertheless, the high-power ionization laser is being developed to realize this USM source, the time is still required, until the muon RF acceleration using the USM can be carried out.

1.5 Muon RF acceleration and the Mu^- production

To accelerate the muon almost at rest, an radio-frequency quadrupole (RFQ) linac [25] is used as the initial RF accelerator. While the short structure of the drift-tube linac is difficult to fabricate in the low velocity region, the fine vane structure in the RFQ can be fabricated to accelerate the low-energy muons. Figure 1.1 shows the schematic drawing of a vane-tip geometry and the longitudinal electric field distribution in a cell for the RFQ. The longitudinal electric field on axis obtained with this modulation geometry enables the acceleration. Since the intensity of the accelerated muon beam is quite lower than that of the ordinary electron or proton beam, the method of the measurement for the accelerated muon beam should be developed. Therefore, the demonstration of the muon RF acceleration must be carried out in a timely manner to develop the low-emittance muon beam.

As the low-energy muon source to carry out the muon RF acceleration in a timely manner, the production of the Mu^- with a thin aluminum foil target (Al target) is used in this study. Since the mean initial kinetic energy of the Mu^- is in vicinity of 0.2 keV, the Mu^- beam extracted with the electrostatic acceleration can match the input energy acceptance of the RFQ. The input energy is 5.6 keV in this study.

Towards the demonstration of the muon RF acceleration, the production yield of the Mu^-

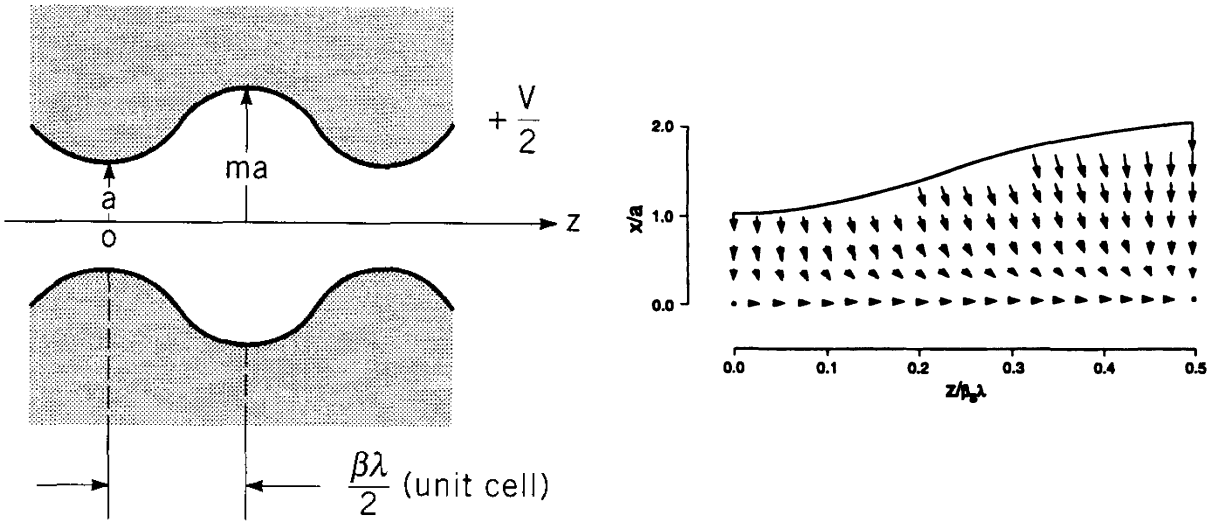

Figure 1.1: Schematic drawing of a pole-tip geometry (left) and longitudinal electric field distribution in a cell (right) for the RFQ. In the left figure, a is the minimum radius of the electrode tip and m is a parameter which is called as the modulation parameter. The length of the unit cell is $\beta\lambda/2$, where β is a velocity of the charged particle and λ is the RF wavelength. These figures are taken from reference [24].

should be measured to estimate the event rate of the accelerated Mu^- with the RFQ. The signal-to-noise ratio of the Mu^- beam is so small that the measurement system should be developed to identify the Mu^- beam. Then, the new measurement system has been developed using the TOF measurement, considering the feature of the pulsed muon beam supplied from the J-PARC. The TOF measurement can suppress the backgrounds such as incident positive muons, decay positrons and low-energy electrons from the field emission. This measurement system consists of the Al target, an electrostatic accelerator, an electric deflector and a bending magnet to reduce the backgrounds and a micro-channel plate (MCP) to detect the Mu^-. The time difference between the collision time of the incident muon at the Al target and the detection time at the MCP is defined as the TOF. With this measurement system, the clear signal of the Mu^- is obtained and the production yield of the Mu^- is measured. As a result, the well-defined Mu^- source is developed for the muon RF acceleration.

Next, the demonstration of the muon acceleration with the RFQ was carried out using the developed Mu^- source. The most difficulty of this experiment is the identification of the signal of the accelerated Mu^-, because the accelerated Mu^- beam contains many backgrounds such as the positive muons which are decelerated at the Al target and the decay positrons. Then, to reduce these backgrounds, the TOF measurement is also introduced as well as the momentum selection with the bending magnet. As a result, since these backgrounds are drastically reduced, the clear signal of the accelerated Mu^- is observed. Furthermore, the measured event rate of the Mu^- is consistent with the expectation from the result in the Mu^- production experiment. This result confirms that the Mu^- beam is exactly accelerated with the RFQ.

1.6 Outline of this dissertation

In this dissertation, the Mu^- source is developed as the low-energy muon source towards the muon RF acceleration. At first, the measurement system is developed to reduce the backgrounds and clearly identify the Mu^- using the TOF measurement, considering the feature of the pulsed

muon beam. Then, the production yield of the Mu^- source is measured with this developed measurement system. The experimental setup, the simulation and the analysis of the Mu^- production experiment are described in chapter 2, 3 and 4, respectively.

Next, the demonstration of the muon RF acceleration is carried out using this developed Mu^- source and the RFQ. With the TOF measurement, the accelerated Mu^- is identified. The event rate of the accelerated is also measured. The experimental setup, the simulation and the analysis of the muon acceleration experiment are described in chapter 5, 6 and 7, respectively. The discussion about the result of the muon acceleration experiment is described in chapter 8. The measured event rate of the accelerated Mu^- is consistent with the expectation from the result of the Mu^- production experiment. Finally, the conclusion of this dissertation is described in chapter 9.

The author mainly contributed to the construction of the measurement system for the Mu^- beam and took all of the data for the both of experiments; the Mu^- production experiment and the muon acceleration experiment. All of the data analyses and beam transport simulations were also carried out by the author.

Chapter 2

Experimental setup of the Mu^- production experiment

2.1 Overview of the setup

The Mu^- production experiment was carried out at the Japan proton accelerator research complex (J-PARC), materials and life science experimental facility (MLF). In the J-PARC MLF, the primary proton beam with 3 GeV energy penetrates through the muon production target made of the graphite produce the intense muon beam via the pion decay. When the positive pions stop near the surface of the muon production target and decay, the muons with 4 MeV are produced. These muons are called as the surface muons. Since the kinetic energy surface muon is higher than the input energy of 5.6 keV in the RFQ, the surface muons are cooled by producing the Mu^- using a thin aluminum foil target (Al target).

Figures 2.1 and 2.2 show the schematic and the experimental setup of the Mu^- production experiment which was carried in the Muon D2 experimental area, respectively. An electrostatic accelerator called as "Soa lens" is used for the extraction. Some of incident muons capture two electrons in the Al target and produce Mu^-'s. The transport beam line consists of a electrostatic defector (ED), five electrostatic quadrupoles (EQ's) and a bending magnet (BM). The Soa lens, the ED and the EQ's had been originally designed for the USM beam line in the RIKEN-RAL (Rutherford Appleton Laboratory) facility, UK [26] and are reused for this Mu^- production experiment. The Mu^- is detected with a micro-channel plate (MCP) [27] located at the downstream end of the transport beam line. Prior to the Mu^- production experiment, a commissioning of the transport beam line was carried out using a H^- beam produced with the ultra-violet light (UV light). In the Mu^- production experiment, the decelerated μ^+ with the degrader and the Al target was also observed, when the polarities of the Soa lens and the apparatuses in the transport beam line are flipped. This decelerated μ^+ is used for the cross-check of the TOF measurement. The Mu^- was observed with the negative polarity of the Soa lens and transport beam line.

2.2 Incident muon beam

Figure 2.3 shows the schematic drawing of the Muon D-line. The D-line transports the muon beam to two experimental areas; D1 and D2. The D-line consists of three bending magnets (DB1-3), fifteen quadrupole magnets (DQ1-15), one solenoid magnet and one wien filter (DSEP), which is used to eliminate the decay positrons. The momentum of the extracted surface muon beam can be changed by tuning the applied current of the magnets. In the Mu^- production experiment, the momentum of the surface muon beam was set to 25 MeV/c. Table 2.1 shows

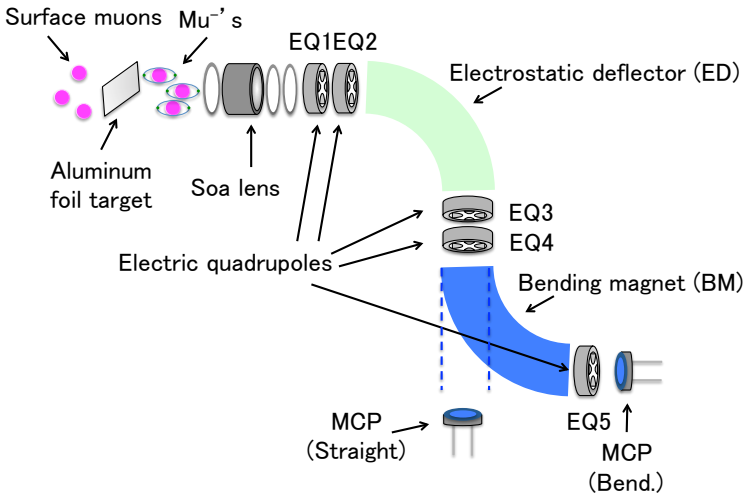

Figure 2.1: Schematic of the Mu^- production experiment.

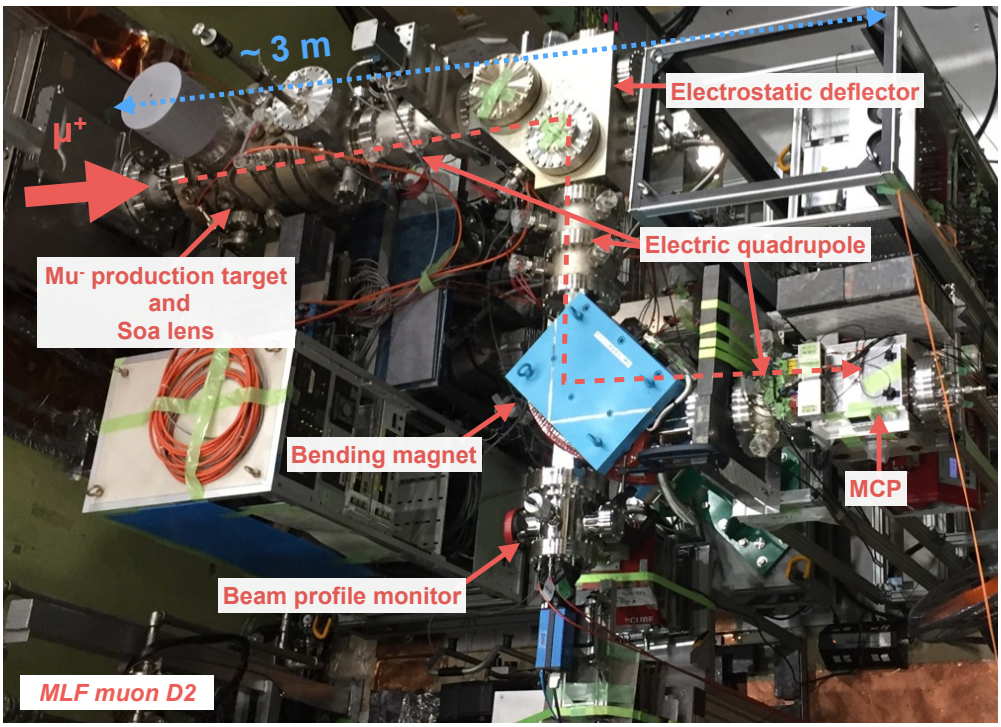

Figure 2.2: Experimental setup of the Mu^- production experiment.

the experimental condition of the incident surface muon beam. One pulse contains one bunch (single pulse) or two bunches (double pulse). It depends on the operating mode of the proton accelerator.

Table 2.1: Parameters of the incident surface muon beam in the Mu^- production experiment.

Proton beam power [kW]	153
Muon beam intensity [μ^+/s]	1.3×10^6
Momentum [MeV/c]	25
Reputation [Hz]	25
Pulse mode	Single

2.3 Mu^- production target and electrostatic accelerator

Figure 2.4 shows the schematic view of the the degraders, Al target and the Soa lens. The SUS foil window separates the vacuum region between the target chamber and the D-line. A thickness and a diameter of the SUS foil window are 50 μm and 8 cm,respectively. The Kapton degrader is used to decelerate the incident μ^+ and consists of two pieces of the Kapton foils with the thickness of 75 μm. The Al target consists of two pieces of aluminum foils with the thickness of 100 μm and is made of the aluminum with a 99 % purity. The total thicknesses of the Kapton degrader and Al target are 150 μm and 200 μm, respectively. The size of the Kapton degrader and the Al target is 43×35 mm^2. Figure 2.5 shows the Al target installed on the target holder.

An electrostatic lens shown in figure 2.4 is used as the electrostatic accelerator. These series of electrodes were known as the "*modified Soa immersion lens*", and primary utilized for the positron studies for the solid physics [29] [30] [31]. The Soa lens has five cylindrical electrodes; T (target including the target holder), S1, S2, S3, and S4 (ground). Voltages are applied to accelerate and focus the Mu^- beam. The maximum applied voltage to the Soa lens was limited to be 20 kV, due to the withstanding voltage of the cables for the Soa lens. The energy acceptance of the transport beam line is increased and the high transport efficiency is obtained, when the accelerating voltage is increased. Since the open aperture ratio of the mash for the S1 electrode is 85 %, the transmission efficiency of the S1 electrode is estimated to be 85 %.

2.4 Beam counter

Three plastic scintillation counters (beam counter) are located near the Mu^- production target to determine the arrival time of the muon beam. Figure 2.6 shows the schematic of the beam counter which consists of a plastic scintillator, a light guide and a photomultiplier tube (PMT), Hamamatsu Photonics Co. H3690-02. The lead blocks are located to eliminate the decay positrons which come from outside the target. Distances between the Mu^- production target, counter A, B, and C are 563 mm, 35 mm 30 mm, respectively. Table 2.2 shows the specifications of the scintillation counters in the Mu^- production experiment. A digital signal of the coincidence event of the three counters was recorded to measure the arrival time of the incident muon beam to the Mu^- production target.

2.5 Transport beam line

The extracted Mu^- is transported to the MCP with the transport beam line. The transport beam line consists of the ED, EQ's and the BM. The decay positron from the incident muon or

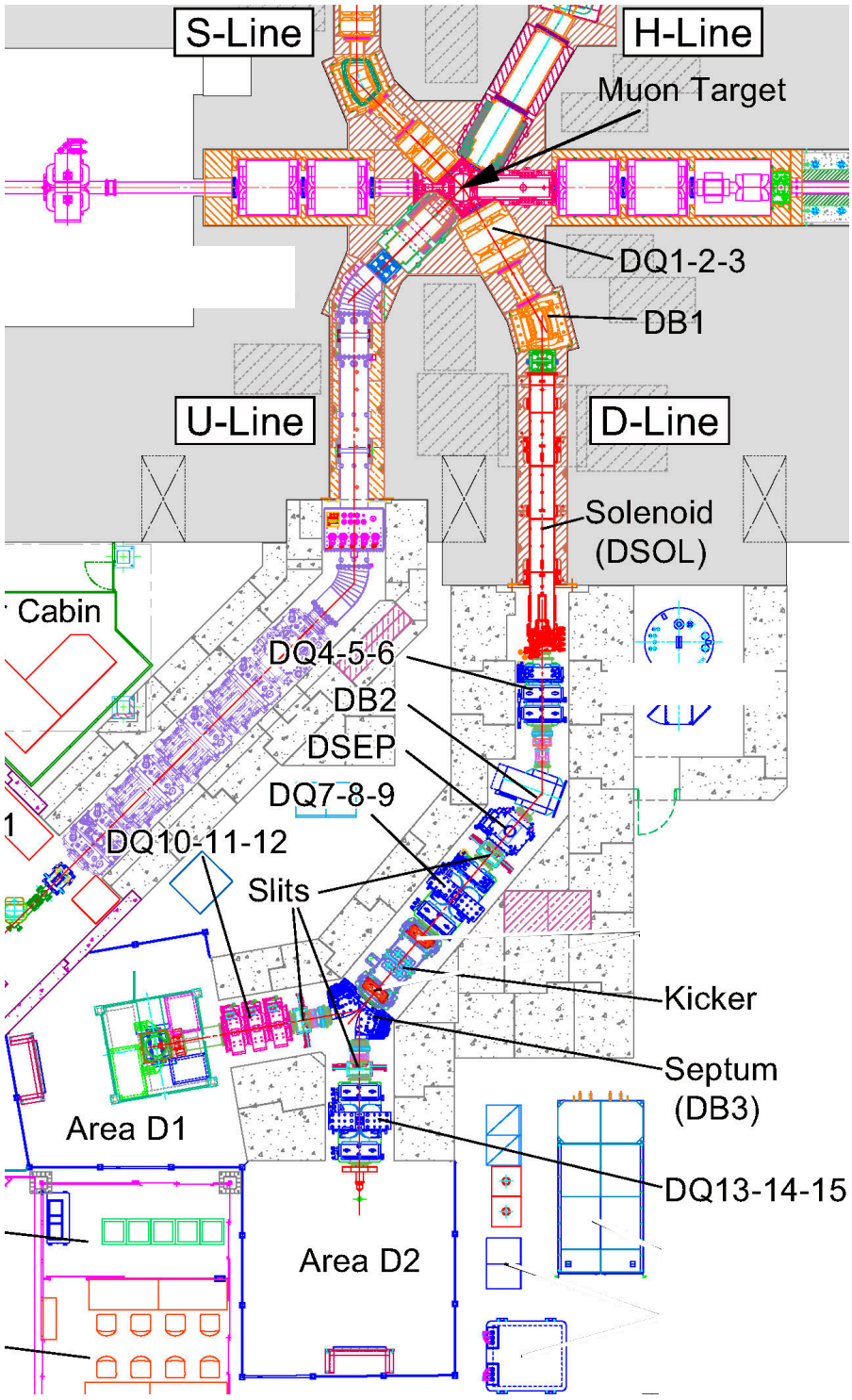

Figure 2.3: Schematic drawing of the Muon D-line. This figure is taken from reference [28].

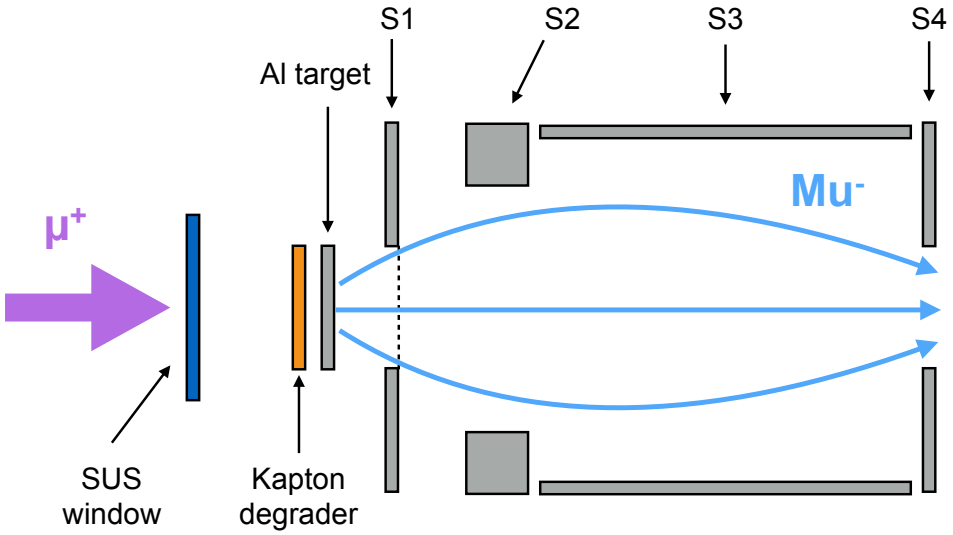

Figure 2.4: Schematic view of the the degraders, Mu^- production target and the Soa lens [29]. S1, S2, S3 and S4 are electrodes of the Soa lens.

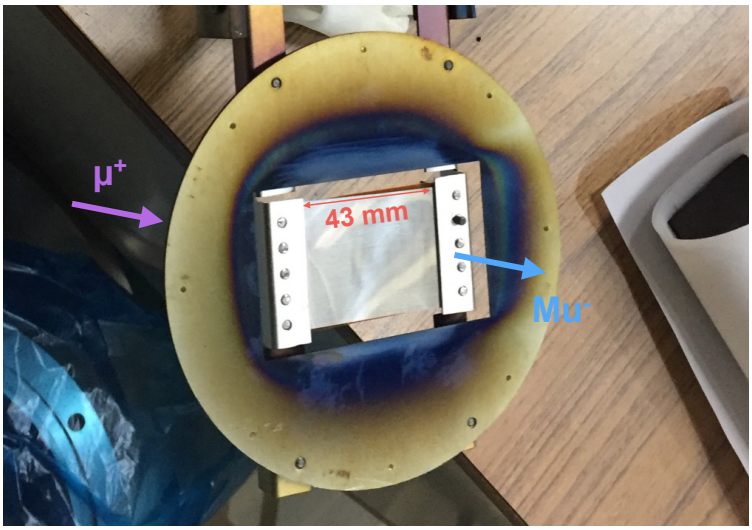

Figure 2.5: Mu^- production target installed on the target holder. The Kapton degrader was overlaid on the Al target.

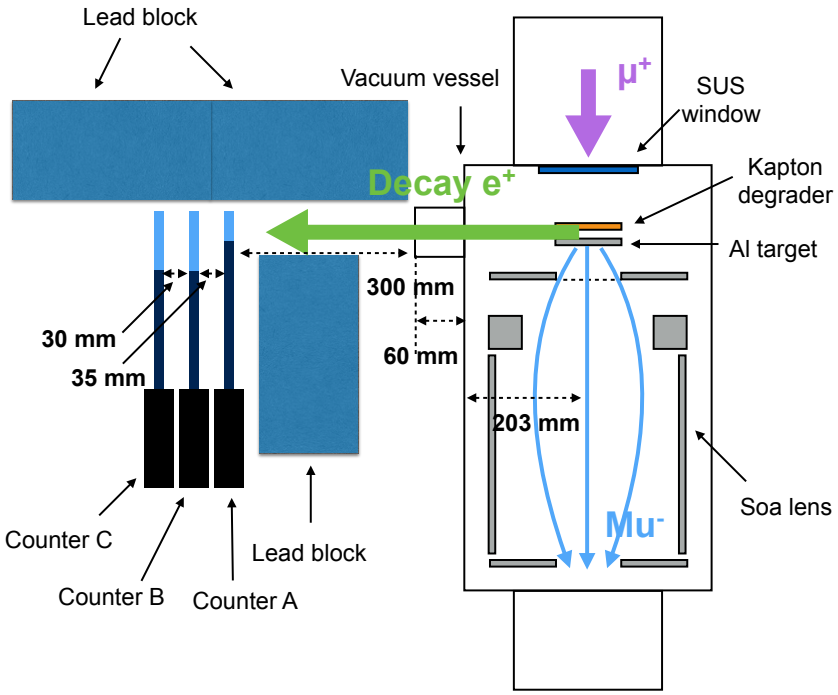

Figure 2.6: Schematic of the beam counter.

Table 2.2: Specification of the beam counter.

	Size of the scintillator	Applied voltage [V]
Counter A	$3 \times 3.5 \times 0.5$ cm^3	-1300
Counter B	$6 \times 6.5 \times 0.5$ cm^3	-1300
Counter C	$6 \times 5.5 \times 1$ cm^3	-1300

the electron produced by the field emission at the Soa lens are eliminated by the selections of the kinetic energy and the momentum using the ED and the BM in the beam line.

Five EQ's are located to transport the Mu$^-$ beam effectively with the transverse focusing. All EQ's are identical. One doublet (EQ1 and EQ2) is located between the Soa lens and the ED and the other doublet (EQ3 and EQ4) is located between the ED and the BM. The last quadrupole (EQ5) is located in front of the detector chamber. Figure 2.7 and table 2.3 show the photograph and the specification of the EQ, respectively. The EQ focuses the beam in one plane but defocus the beam in the other plane. Table 2.4 shows transverse focusing directions of EQ's in the μ^+ and Mu$^-$ measurements. The polarities of the EQ's are flipped, when the setting was changed from the measurement of the μ^+ to that of the Mu$^-$.

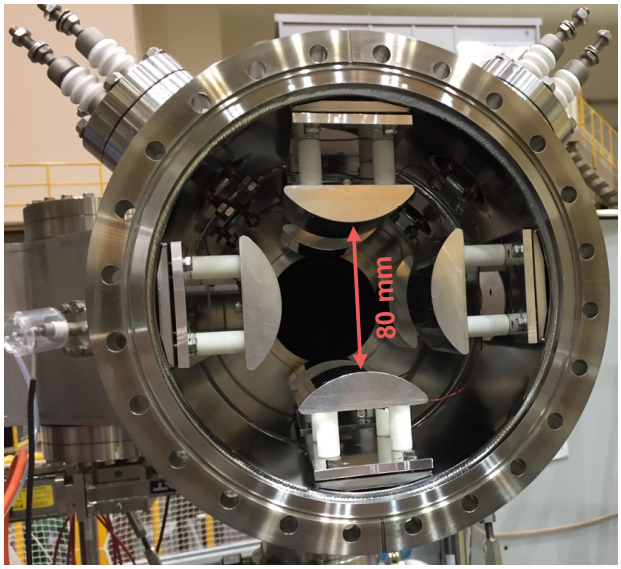

Figure 2.7: Photograph of the EQ.

Table 2.3: Specification of the EQ.

Typical voltage [kV]	1.0
Length of the electrode [mm]	80
Electrode aperture [mm]	80

Table 2.4: Transverse focusing directions of EQ's in the μ^+ and Mu$^-$ measurements.

EQ1	Y
EQ2	X
EQ3	Y
EQ4	X
EQ5	Y

The Mu$^-$ is bended with the ED by 90 degrees. The ED is located between the EQ2 and the EQ3. Figure 2.8 and table 2.5 show the schematic drawing and the specification of the ED, respectively. The charge and kinetic energy can be selected using the ED. Therefore, the decay positron from the incident surface muon is eliminated with the ED, because the kinetic energy of

the decay positron is mainly more than 20 keV. The applied voltage is 5 kV to bend the charged particle with 20 keV.

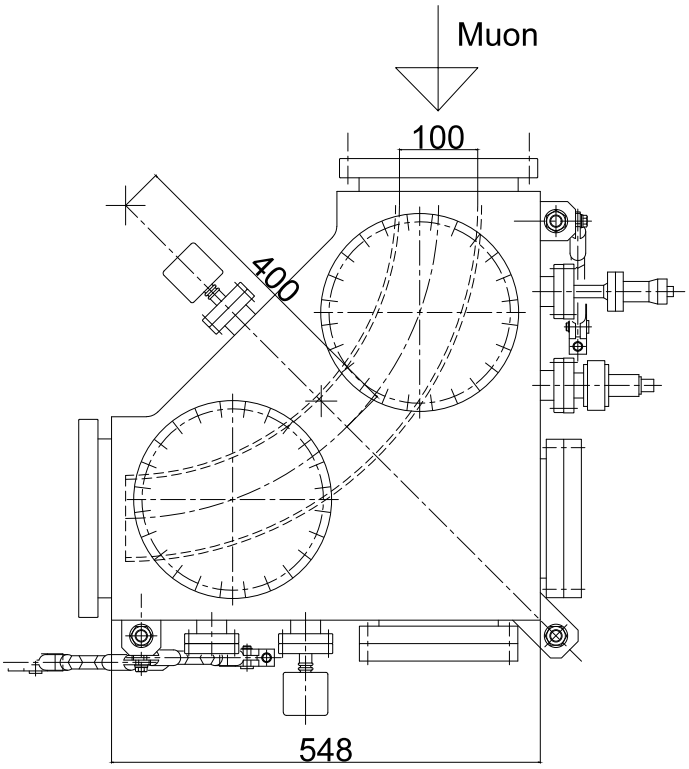

Figure 2.8: Schematic drawing of the ED.

Table 2.5: Specification of the ED.

Deflection angle [degree]	90
Maximum withstand voltage [kV]	2.5
Curvature radius [mm]	400
Electrode aperture [mm]	100

The Mu^- is bended with the BM by 90 degrees. Table 2.6 shows the specification of the BM. The electron generated by the field emission at the Soa lens cannot be eliminated using the ED, because the kinetic energy of this electron is same as that of the accelerated Mu^-. This electron is eliminated with the BM, since the momentum of the electron is different from that of the Mu^-. Only the Mu^- can be transported to the MCP using the ED and the BM. The incident muons penetrated through the Al target are stopped at the ED and produce many decay positrons. The ED and the BM are also useful to eliminate these decay positrons.

2.6 Detector

The single-anode MCP is used to detect the decelerated μ^+ and the Mu^-. The MCP for the beam profile monitor (BPM-MCP) which is described in Appendix C.1 is also used. It has almost the same specification of the single-anode MCP. The MCP consists of millions to tens of millions of ultra-thin conductive glass capillaries (or channels). When the charged particle

Table 2.6: Specification of the BM.

Deflection angle [degree]	90
Magnetic field [Gauss]	300
Current [A]	20
Voltage [V]	6
Cooling	Air cooling

hits the wall in the channel of the MCP, secondary electrons are produced. These secondary electrons are accelerated with the potential gradient in the MCP and hit the opposite side of the wall. The number of electrons is increased with these processes repeatedly. The produced many electrons are obtained as the electrical output signal.

The MCP is suitable to detect the decelerated μ^+ and the Mu^-, since the MCP can detect the low-energy ion with a high sensitivity in principle. Table 2.7 shows the specification of this MCP. The time resolution in this experiment depends on the sampling speed of the flash ADC (FADC) for the data acquisition system (DAQ). The time resolution is 4 ns/$\sqrt{12}$ ≈1.2 ns, because the sampling time is 4 ns. The gain of the MCP was measured using the photoelectron produced from the γ-ray source (^{55}Fe). The measured gain was $(9.95 \pm 0.88) \times 10^6$ C/e [32]. The detection efficiency of the MCP depends on the open aperture ratio of the channel on the surface, which is 60 % for this MCP.

Figure 2.9 shows the typical pulse height distributions of this MCP. In figure 2.9, the high-energy decay positron was produced from the positive muon at rest. The 500 eV electron was produced from the photoelectron generated with the UV light, while the field gradient of 500 V was applied to the entrance plane of the MCP. In the toy model, the pulse hight depends on the number of secondary electrons, when the incident particle hit the wall in the MCP. If the high-energy particle such as the decay positron enters the MCP, the secondary electrons are amplified in the multi-channel, because the decay positron penetrates through the several channels. This multi-channel effect was also considered in this toy model.

When the decelerated μ^+ or the Mu^- enters a channel in the MCP, the secondary electrons are produced for the the full length of the channel. On the other hand, when the decay positron enters the channel, the positron penetrates the channel wall and the secondary electrons are amplified from the intermediate position of the channel. Therefore, although the multi-channel contributes to the amplification, the gain of the MCP with the decay positron is smaller than that with these ions. In figure 2.9, the peak of the pulse hight distribution of the decay positron was shifted to the lower side compared with that of the 500 eV electron. As the typical response of these ions; decelerated μ^+ and Mu^- are same as that of the low-energy electron, the low pulse-height events produced from the positrons are eliminated using the pulse height cut.

2.6.1 Data acquisition system

The analog signals from the single-anode MCP and the BPM-MCP are digitized with a FADC. Table 2.8 shows the specification of the flash ADC (FADC) module, CAEN V1720. A sampling time of the FADC is 4 ns. The DAQ trigger is synchronized with the accelerator trigger, that is the beam arrival signal into the experimental area. The gate width of the sampling is set to 10 μs.

Figure 2.10 and 2.11 show the diagram of applied voltages and the DAQ system for the single-anode MCP and that for the BPM-MCP, respectively. The pulse width of the raw waveform is broadened with the fast-filter amplifier (ORTEC 579), because the pulse width of the raw waveform is too narrow for the FADC with the sampling width of 4 ns. The data is sent to a

Table 2.7: Specification of the single-anode MCP [33] [34] .

Model of MCP assembly	F9892-21
MCP type	F1217-011G
Thickness per plate (L) [μm]	480
Channel diameter (d) [μm]	12
Channel pitch [μm]	15
Channel length-to-diameter ratio (L/d=α)	40
Bias angle [degree]	12
Effective area [mm]	ϕ42
Number of stages	2
Typical gain(Min.)	1×10^6
Plate resistance per MCP [MΩ]	8$\sim$32
Dark count (Max.) [$s^{-1}\cdot cm^{-2}$]	3
Pulse width (FWHM, typical) [ns]	0.9
Operating vacuum pressure (Max.) [Pa]	1.3×10^{-4}
Open aperture ratio [%]	60

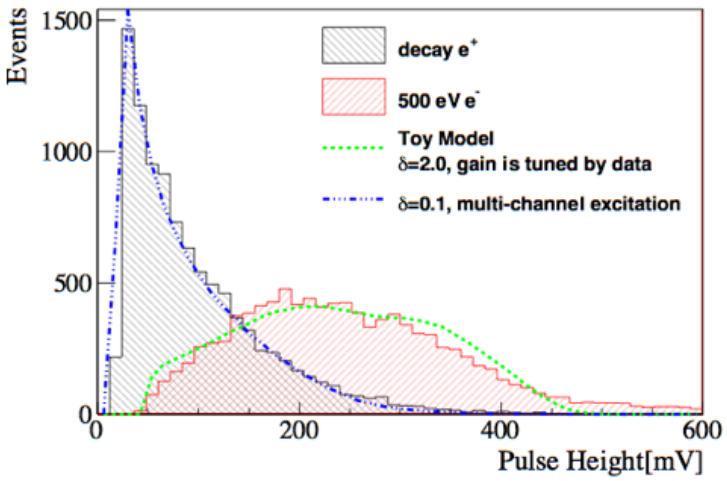

Figure 2.9: Pulse height distributions of the single-anode MCP. The δ is the assumed number of secondary electrons when the incident particle hits the wall in the channel of the MCP. This figure is taken from reference [32].

DAQ PC and recoded in the ROOT [35] format.

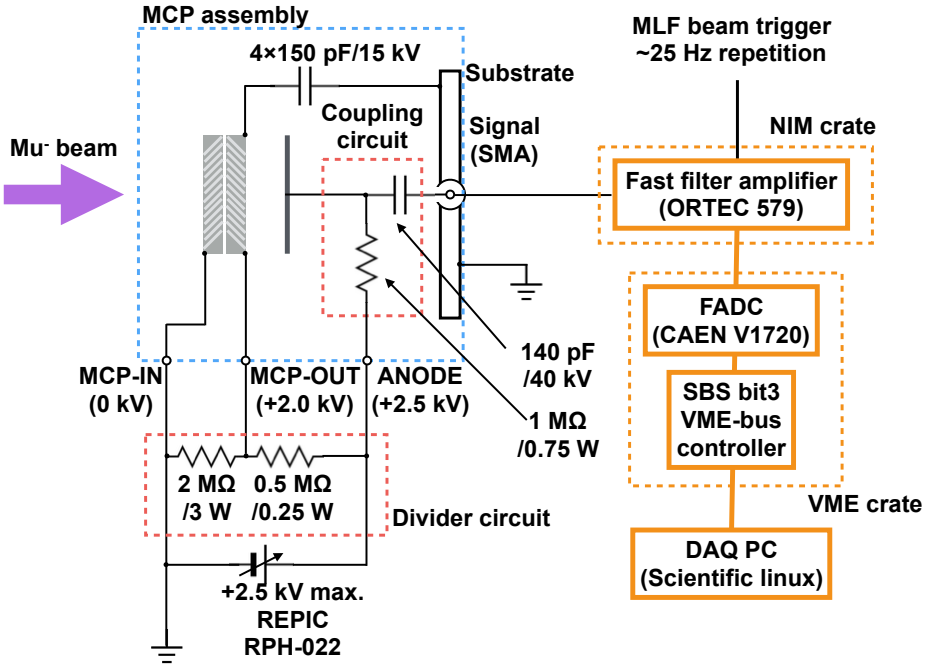

Figure 2.10: Diagram of the applied voltages and the DAQ system of the single-anode MCP.

Table 2.8: Specification of CAEN V1720 flash ADC [36] [37].

Model	CAEN V1720 FADC
Form	VME
Number of channels	8
Max. sampling frequency [MS/s]	250
Number of bits	12
Input dynamic range (V_{pp})	2
Bandwidth [MHz]	125

2.7 Remote control system and vacuum system

The power supplies for the beam line components are remotely controlled with the experimental physics and industrial control system (EPICS) [38] and the programable logic controllers (PLC's). The EPICS is a set of the open source software tools, libraries and applications developed collaboratively and used to create distributed soft real-time control system for scientific instruments such as a accelerator, telescopes and other scientific experiment. When the applied voltage or current is set using the online interface, the EPICS sends the parameter to the PLC's. The PLC's control the power supply with the analog and digital signals. In addition, the PLC's monitor the applied voltage or current and send their values to the EPICS. Table 2.9 shows the list of power supplies used in the Mu^- production experiment.

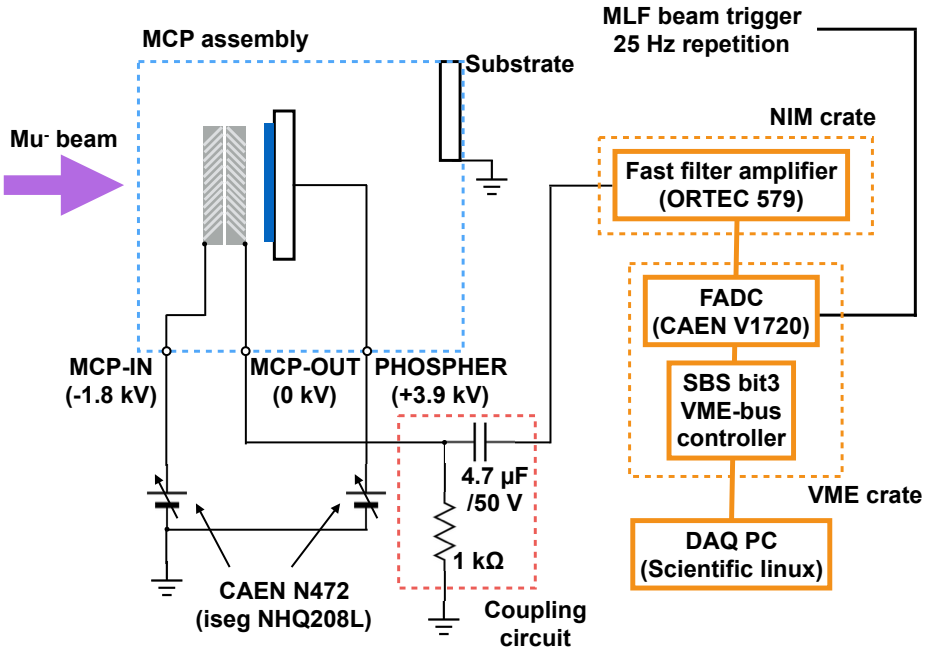

Figure 2.11: Diagram of the applied voltages and the DAQ system of the BPM-MCP.

Several vacuum pumps are used, since the MCP should be operated in the vacuum of less than 1.3×10^{-4} Pa and a good beam transmission is obtained in the vacuum. Figures 2.12 and table 2.10 show the block diagram of the vacuum system of the transport beam line and the list of the vacuum pumps in the Mu^- production experiment, respectively. The vacuum pressure is monitored with two vacuum gauges at the target chamber and the detector chamber to maintain the good vacuum level.

*Made by Kudou Denki Co.

Table 2.9: Power supplies used in the Mu^- production experiment.

Content	Electrode	Model of the power supply	Max. vol. [kV]	Applied vol. [kV]
Soa lens	T	SPELLMAN SL20PN150 [39]	20	20.00
		MATSUSADA HAR-30N2	30	20.00
	S1	SPELLMAN SL20PN150	20	18.94
	S2	SPELLMAN SL20PN150	20	18.04
	S3	SPELLMAN SL20PN150	20	16.00
EQ	EQ1	P.S. (KEK original)*	2	0
	EQ2	P.S. (KEK original)	2	0.35
	EQ3	P.S. (KEK original)	2	0.68
	EQ4	P.S. (KEK original)	2	0.66
	EQ5	P.S. (KEK original)	2	0
ED	ED+	MATSUSADA HAR-20P15	20	5.00
	ED-	MATSUSADA HARb-30N40-LF	30	5.00
Content		Model of the power supply	Max. curr. [A]	Applied curr. [A]
BM		MATSUSADA PRK10-150-LMi	150	16.3

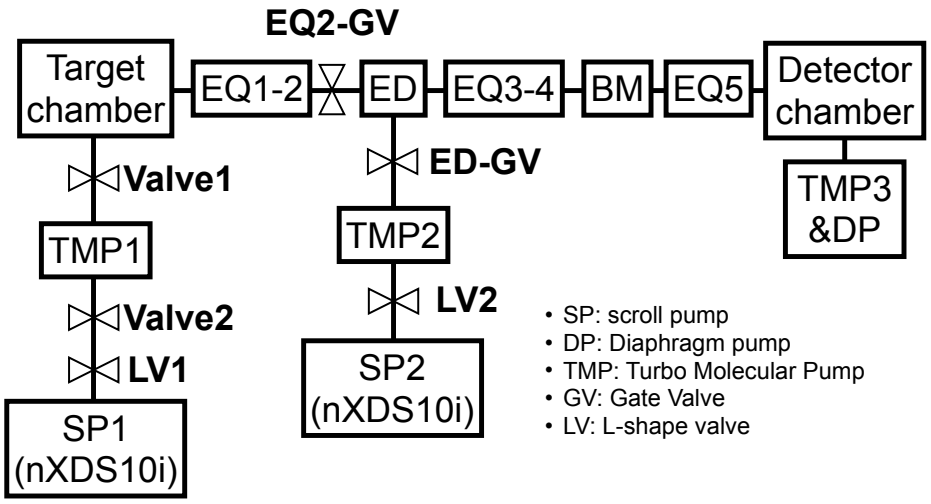

Figure 2.12: Block diagram of the vacuum system of the transport beam line.

Table 2.10: List of the vacuum pumps in the Mu^- production experiment.

ID	Model	Pumping speed [L/s]	Typical pressure [Pa]
TMP1	ULVAC GMT-500	550	1.7×10^{-5}
TMP2	Pfeiffer TMU 520	500	2.2×10^{-5}
TMP3	Pfeiffer HiCube Eco 80	35	2.1×10^{-5}

Chapter 3

Simulation of the Mu^- production experiment

The simulation for the Mu^- production experiment is described in this chapter. This simulation aims to evaluate a target acceptance, a beam transport efficiency of the Mu^- and the TOF of the Mu^-. First, the beam transport of the surface muons through the Muon D-line is simulated. The initial kinetic energy distribution of the Mu^- is generated based on the data of the charge exchange of hydrogen atoms. The initial position and angle distributions in the Mu^- production process are regarded as the same distributions of the decelerated μ^+ simulation which is described in Appendix D.1. The cooling efficiency of the Mu^- is defined as the ratio of the Mu^- with less than 2 keV to the number of the incident μ^+, because the muons with the initial kinetic energy of less than 2 keV at the Al target can be transported to the MCP as described in Appendix D.2. This cooling efficiency of the Mu^- will be evaluated by the measurement in next chapter. Then, the beam transport of the Mu^-'s is simulated. The transport efficiency and the TOF of the Mu^- are estimated using this simulation.

3.1 Incident surface muon beam

The beam transport of the surface muons is simulated using G4beamline [40] which is a particle tracking simulation based on GEANT4 [41]. The distance between the center for the muon production target and the beam port at the Muon D2 experimental area is 23.6 m on the beam axis. The incident muon beam at the D2 area focused on the point 800 mm downstream from the end edge of the last triplet quadrupole (DQ15).

The beam size of the proton beam was assumed to be ϕ24 mm based on the measurement. The pions are generated using the an empirical differential cross-section equation, which approximates the data taken with the proton beam of 2.9 GeV using a beryllium target [42]. The energy loss of the pions are calculated with the Bethe-Bloch formula in the target [43]. The pions stopped at the surface of the target with the thickness of a few hundred μm contribute to produce the surface muons. The number of the surface muons dN_μ with a small faction of the momentum dp calculated with the Bethe-Bloch formula as $dN_\mu/dp \propto p^{2.6}$.

Figure 3.1 show the simulated beam profile distributions of the surface muon beam at the Mu^- production target. The red rectangle in figure 3.1 represents the size of the Mu^- production target. Muons on the Mu^- production target contribute to the deceleration of the μ^+ and the Mu^- production. The target acceptance is defined as $\varepsilon_{\rm tar} = N_{\rm tar}/N_{\rm inc.}$, where $N_{\rm tar}$ is the number of the muons in the target region and $N_{\rm inc.}$ is the total number of the incident muons at the target position. The target acceptance is calculated to be 24%.

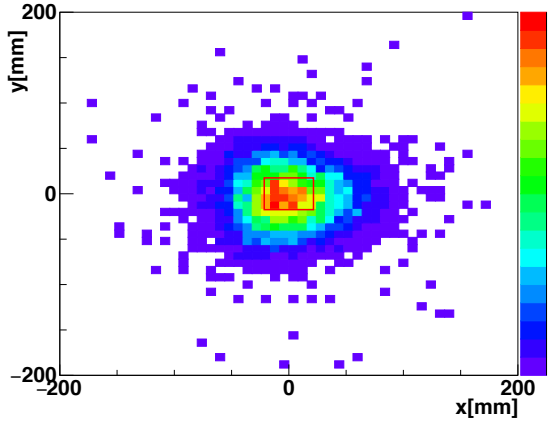

Figure 3.1: Simulated beam profile distribution of the surface muons at the Mu^- production target. The red rectangle is the shape of the Mu^- production target.

3.2 Mu^- production

The kinetic energy and angle distributions of the produced Mu^- at the Mu^- production target are generated using the data of the H^- production [44] and the result of the simulation of the decelerated μ^+, which is described in Appendix D. The position distribution of the Mu^- is same as that of the decelerated μ^+. According to reference [44], the charge state equilibrium in the solid is explained by the overlap of the atomic and the solid-state electron wave functions in wavenumber space. In the charge exchange process of the proton penetrated through the foil target, the conversion fractions of the overlap between the projectile and the atom for the neutral and the negative stats in the target $Q_{0,-}$ are described as

$$Q_{0,-} = 1 - \frac{1 - k_{0,-}^2 + (s/k_F)^2}{2s/k_F}, \tag{3.1}$$

where k_0, k_- and k_F are empirical parameters, and $s = v/v_0$ where v is the velocity of the projectile and v_0 is the velocity of the proton with 5 keV. The ratio of equilibrium charge state yields between H^+ and H^- at the surface of the target is described using equation (3.1) as

$$\frac{Y^-}{Y^+} = \frac{a_0 a_- Q_0 Q_-}{(1 - Q_0)(1 - Q_-)} \cdot e^{(p_0 - p_1)s}, \tag{3.2}$$

where a^0, a^-, p_0 and p_- are empirical parameters. Table 3.1 shows these empirical parameters from [44]. Then, the two-dimensional distribution of the kinetic energy w′ and the angle θ' for the Mu^- $f_{\text{Mu-}}(\text{w}', \theta')$ is described as

$$f_{\text{Mu-}}(\text{w}', \theta') = f_{\text{dec.}\mu}(\text{w}, \theta)\frac{Y^-}{Y^+}, \tag{3.3}$$

where $f_{\text{dec.}\mu}(\text{w}, \theta)$ is the two-dimensional distribution of the kinetic energy w and the angle θ for the decelerated μ^+. Figure 3.2 shows the generated two-dimensional distribution of the kinetic energy w′ and the angle θ' for the Mu^-. These w′ and θ' are generated to reproduce this two-dimensional distribution. Then, the angle distributions x′ and y′ of the Mu^- are calculated from the w′ and the θ' using equation (D.1). The azimuthal angle of the Mu^- ϕ' is assumed to be an uniform distribution in equation (D.1).

As a result, the kinetic energy and phase-space distributions of the Mu^- after the Al target are generated as shown in figures 3.3 and 3.4. The means and the sigmas of the positions

x and y are same as those of the decelerated μ^+. Sigmas of the position x and y with the Gaussian are assumed to be 19 mm and 27 mm, respectively, because those are referred from the measurement [45]. The generated events with less than 2 keV is used for the beam transport simulation, because the muons with less than 2 keV can be transported using this transport beam line. The number of generated events is 1×10^6 events.

Table 3.1: Empirical parameters to generate the initial kinetic energy of the Mu^-.

k_0	0.991
k_-	0.989
k_F	1.178
a_0	0.953
a_-	0.029
p_0	0.284
p_1	0.193

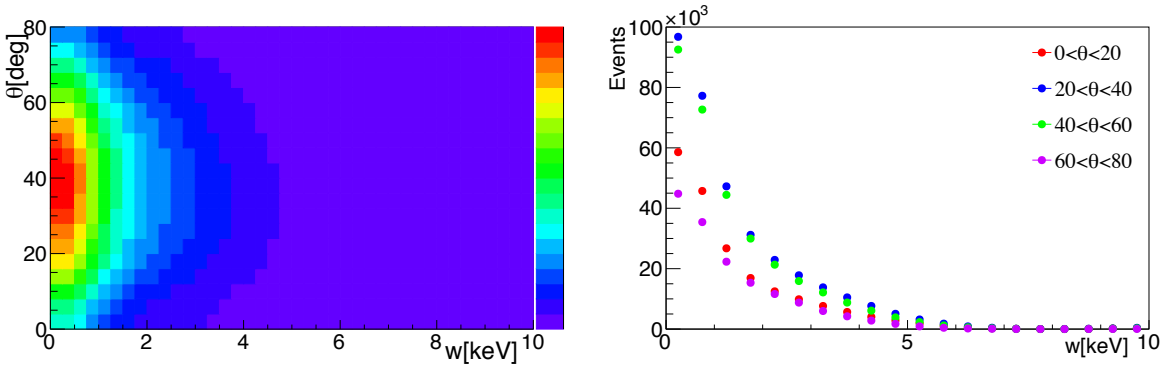

Figure 3.2: Generated two-dimensional distribution of the kinetic energy w′ and the angle θ' for the Mu^- (left) and the kinetic energy distribution for each angle region (right). The total number of the generated events is 1.0×10^6 events.

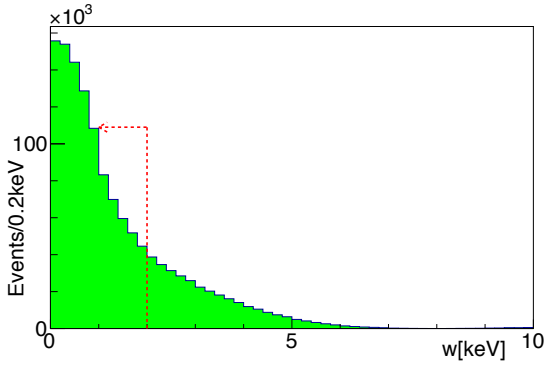

Figure 3.3: Generated kinetic energy distribution of the Mu^- at the Mu^- production target. Events with less than 2 keV are used as indicated with the red dotted arrow.

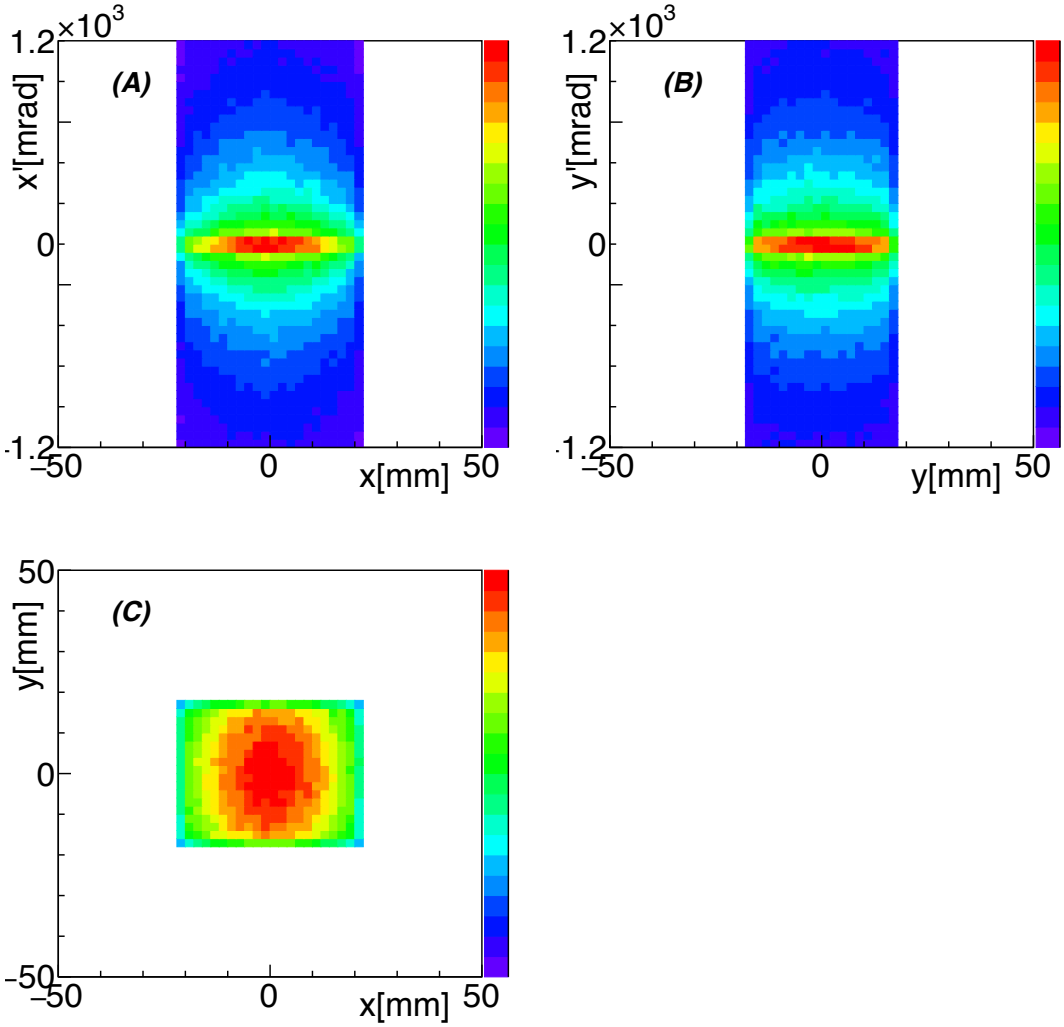

Figure 3.4: Generated phase-space distributions of the Mu^- with less than 2 keV at the Mu^- production target. (A) the horizontal divergence angle x' vs the horizontal position x, (B) the vertical divergence angle y' vs vertical position y, and (C) y vs x.

3.3 Beam transport simulation

The beam transport of the Mu^- is simulated using musrSim [46]. Figure 3.5 shows the schematic view of the beam transport simulation. The electric fields of the Soa lens, the ED, and the EQ's, and the magnetic field of the BM are generated with OPERA [47] and implemented in musrSim. Strengths of their fields are set to those in the experimental condition, which are shown in chapter 2.

Figures 3.6 and 3.7 show simulated phase-space distributions of the Mu^- at the MCP. The transport efficiency, $\varepsilon_{\text{trans.}}$ is defined as $\varepsilon_{\text{trans.}} = N_{\text{det.}}/N_{\text{gen.}}$, where $N_{\text{det.}}$ is the number of Mu^-'s detected with the MCP, and $N_{\text{gen.}}$ is the number of generated events. The number of the detected events is defined as the events within the effective area of the MCP. Table 3.2 shows the number of generated and detected events for the Mu^- in the beam transport simulation. From table 3.2, the transport efficiency of the Mu^- is 9.5×10^{-3}.

From the time distributions in figure 3.6, the mean TOF of the Mu^- is 665.7 ns. The distance from the Mu^- production target to the MCP detector is 3.49 m, and the β of the 20 keV muon is 0.0194. Therefore, the drift time of this muon is 601.0 ns. The difference between this drift time and the simulated TOF, 64.7 ns, comes from the acceleration time in the Soa lens.

The mesh electrode (S1) is used in the Soa lens to extract the Mu^-'s into the downstream beam line. The transmission of the S1 electrode is assumed to be same as the open aperture ratio of the mesh, which is 85 %. The detection efficiency of the MCP is assumed to be 60 %, which is derived from the open aperture ratio.

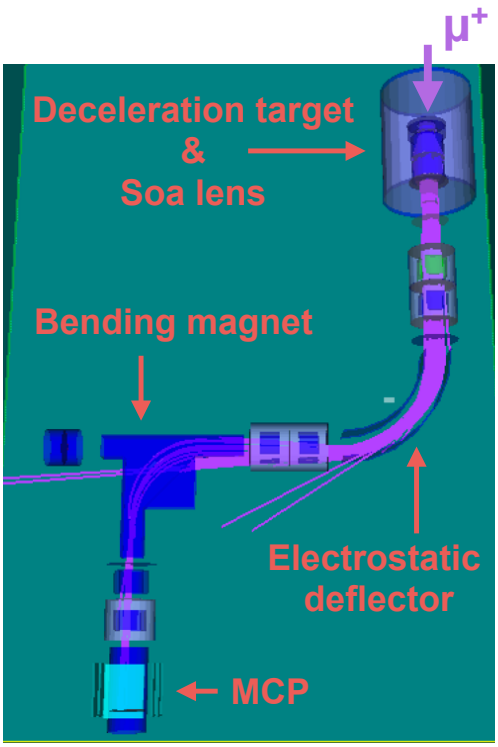

Figure 3.5: Schematic view of the beam transport simulation.

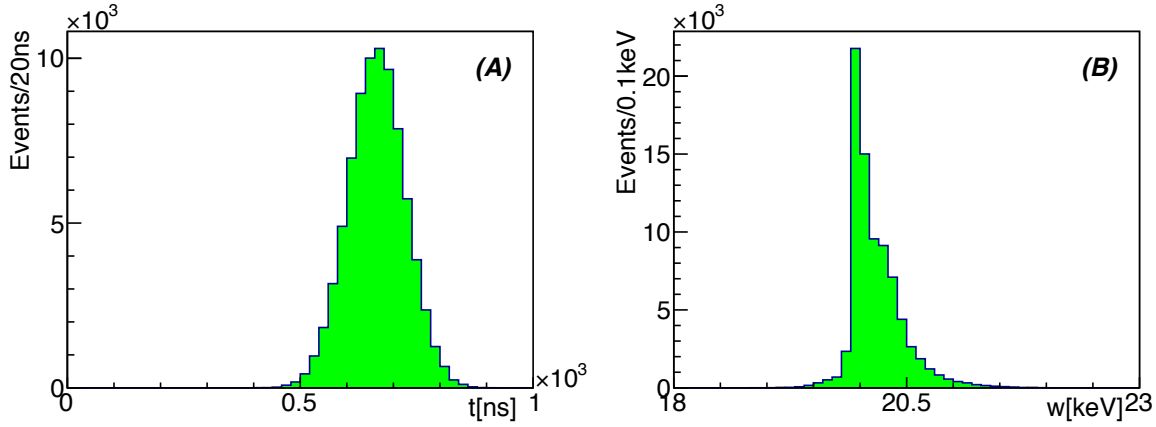

Figure 3.6: (A) simulated time distribution t, and (B) kinetic energy distribution w for the Mu^- at the MCP.

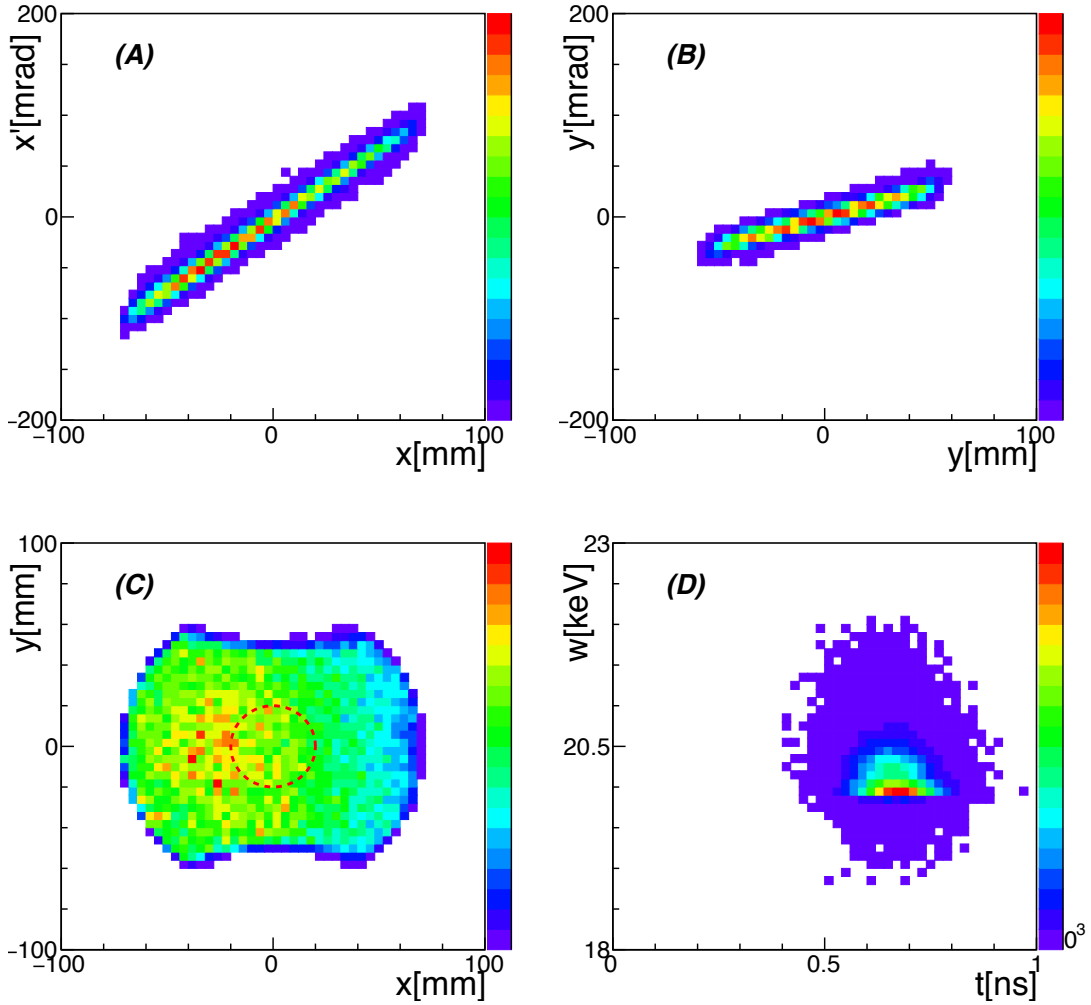

Figure 3.7: Simulated phase-space distributions of the Mu^- at the MCP. (A) the horizontal divergence angle x' vs the horizontal position x, (B) the vertical divergence angle y' vs vertical position y, (C) y vs x, and (D) the kinetic energy distribution w vs the time distribution t. Red dotted circle in the x-y distribution shows the effective area of the MCP.

Table 3.2: Number of generated events and detected events for the Mu^- in the beam transport simulation.

N_{gen}	1×10^6
N_{det}	9484
Transmission	9.5×10^{-3}

3.4 Summary of the simulation for the Mu^- production experiment

In table 3.3, the target acceptance, the transport efficiency of the Mu^- evaluated with the simulations and other efficiencies are summarized. The cooling efficiency for the Mu^- will be estimated from the data of the Mu^- production experiment in the next chapter. The TOF of the Mu^- is also evaluated from the result of the simulation, which is 665.7 ns.

Table 3.3: Estimated efficiencies of the beam transport for the Mu^-.

Target acceptance	2.4×10^{-1}
Mesh transmission efficiency	8.5×10^{-1}
Beam transport efficiency	9.5×10^{-3}
Detection efficiency of the MCP	6.0×10^{-1}

Chapter 4

Analysis of the Mu^- production experiment

The analysis of the event rate and the TOF for the Mu^- is described in this chapter. Accelerated Mu^-'s were transported to the BPM-MCP which was located at the end of the transport beam line. Table 4.1 shows the summary of the data set taken in the beam test. When the setting is the positive extraction, polarities of the Soa lens and the transport beam line are set to transport the positive charged particle such as the μ^+. Conversely, when the setting is the negative extraction, those polarities are set to transport the negative charged particle such as the Mu^-.

Table 4.1: Data set of the Mu^- production experiment.

Data set	Number of triggers	Data acquisition time [hours]	Number of events after the event reconstruction
Positive extraction	6.5×10^5	7.2	1779
Negative extraction	5.5×10^5	6.2	1351

4.1 Signal processing

Signal waveforms from the BPM-MCP were digitized with the FADC as shown in figure 4.1. The hit timing and pulse heights are extracted from the waveform data. The threshold is set to be 70 mV. The width of the sampling gate for the FADC was 10 μs. The base line to calculate the pulse height is defined as the average of the ADC counts for 400 ns from the beginning of the gate. The ADC count was converted into the voltage using the calibration data taken with the pulse generator. The first pulse which exceeds the threshold was regraded as a signal and the pulse height and hit timing were recorded. Following 400 ns was vetoed to prevent double counting the signal.

4.2 Event selection

4.2.1 Determination of the muon arrival time

The arrival time of the incident surface muon beam on the Al target, which is regarded as the muon arrival time t_0, should be determined, because the decelerated μ^+ and the Mu^- are

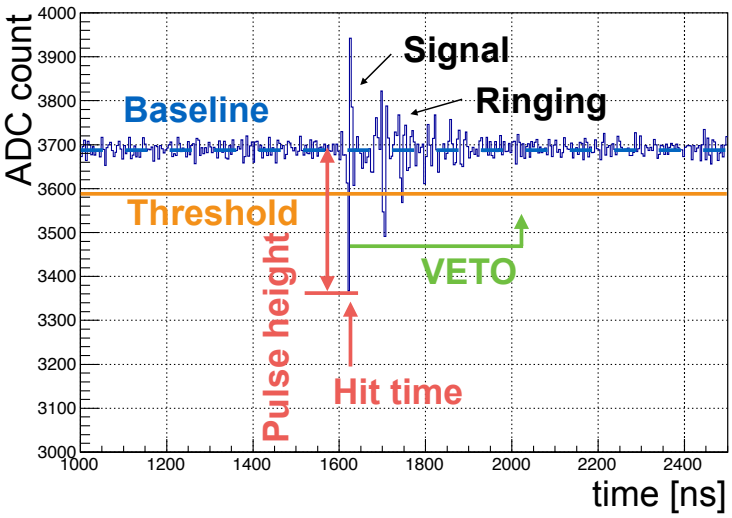

Figure 4.1: Waveform of the BPM-MCP.

identified using the TOF method. The t_0 is defined as

$$t_0 \equiv t_{\text{prompt}} - \Delta t, \tag{4.1}$$

where t_{prompt} is the arrival time of the prompt positrons and Δt is the time difference of arrival times between the prompt positrons and the incident surface muons. The prompt positrons and surface muons are produced at the same time in the muon production target. The prompt positrons are transported in the D-line at the speed of light and arrived at the experimental area earlier than the surface muons. The Δt is constant, if the setting of the D-line is same. Therefore, if t_{prompt} in the time distribution is determined and Δt is known, t_0 of the TOF can be determined. Figure 4.2 shows the signal peak of prompt positrons in the time distributions taken with the BPM-MCP. The fitting function is the Gaussian with an offset term. By this fitting, t_{prompt} is determined as

$$t_{\text{prompt}} = 750.5 \pm 3.0 \text{ ns}. \tag{4.2}$$

Next, Δt was measured using the beam counter. The digital signal from the coincidence module was recorded with the FADC and the hit time was extracted. Figure 4.3 shows the time distribution of the coincidence events of the beam counter. The fitting function is defined as

$$f(t) = p_0 e^{-\frac{t}{\tau}} \frac{1}{e^{-a(t-t_0)}} + p_1 N(t, t_{\text{prompt}}, \sigma^2), \tag{4.3}$$

where p_0, p_1 and a are fitting parameters, τ is the muon life time, t_0 is the arrival time of the muon at the Al target and $N(t, t_{\text{prompt}}, \sigma^2)$ is the Gaussian in which the mean is t_{prompt} and the sigma is σ. The first term disctibes the convolution of the muon decay function and the sigmoid function to describe the step function. The second term describes the peak of the prompt positrons. By fitting with this function, t_0 and t_{prompt} are evaluated as

$$t_0 = 1320.2 \pm 0.1 \text{ ns} \tag{4.4}$$

$$t_{\text{prompt}} = 1021.7 \pm 0.4 \text{ ns}. \tag{4.5}$$

The Error is the statistical error only. Therefore, Δt is evaluated as

$$\Delta t = t_0 - t_{\text{prompt}} = 298.4 \pm 0.4 \text{ ns}. \tag{4.6}$$

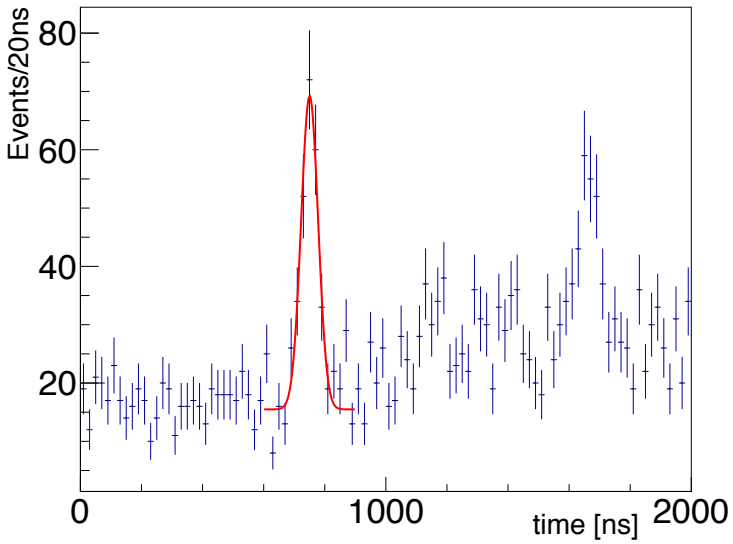

Figure 4.2: Prompt positrons in the time distribution with the data of the positive extraction setting taken with the BPM-MCP. The peak around 1350 ns is the decelerated μ^+'s.

As a result, the muon arrival time of incident surface muons for the BPM-MCP is estimated using equations (4.1), (4.2) and (4.6) as

$$t_0 = 1049.9 \pm 3.0 \text{ ns}. \tag{4.7}$$

The TOF distribution was obtained by subtracting t_0 from the time distribution obtained in section4.1. Figure 4.4 and 4.5 show the scatter plots of the TOF and pulse height and the TOF distributions for a series of data. Figure 4.6 shows the TOF distributions of the positive and negative extractions with the threshold of 100 mV. The peak of the decelerated μ^+ or the Mu^- events was observed from figure 4.6.

4.2.2 Background suppression

To eliminate the background from the decay positrons, the pulse height cut was applied. While the event rates of the decelerated μ^+ and the Mu^- are measured with fitting, some of the events are lost with the pulse height. Therefore, the selection efficiency with the pulse height cut should be consider to evaluate the net event rate. The peaks of the muons in the pulse height distribution are observed from figure 4.4. As shown in section 2.6, while the pulse height of the muon waveform is higher than that of the decay positron. The net pulse height distributions of the muons are obtained by subtracting the pulse height distributions in the sideband region from those in the signal region. Figure 4.7 shows pulse height distributions in the signal and sideband region for data of the positive and negative extractions. These pulse height distributions are normalized with the number of events in the pulse height region of 70 mV to 100 mV, in which events are almost decay positrons. Figure 4.8 shows pulse height distributions in the sideband regions every 1000 ns for data of positive and negative extractions. No significant difference in these pulse height distribution is seen. Figure 4.9 shows the comparison of subtracted pulse height distributions for decelerated μ^+'s and Mu^-'s.

Figure 4.10 shows the subtracted pulse distribution for the μ^+ extraction and the survival fraction with the pulse height cut, when the threshold was scanned. The threshold for the subsequent extend-likelihood fitting is determined to 100 mV from figure 4.10 to obtain the survival fraction of 1.000 ± 0.003.

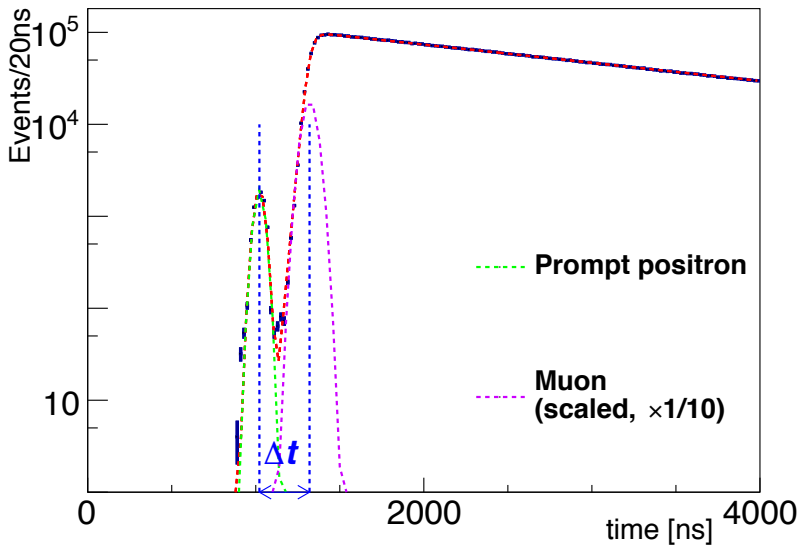

Figure 4.3: Time distribution of the coincidence events of the beam counter. Peak distributions of muons was scaled by a factor of 1/10.

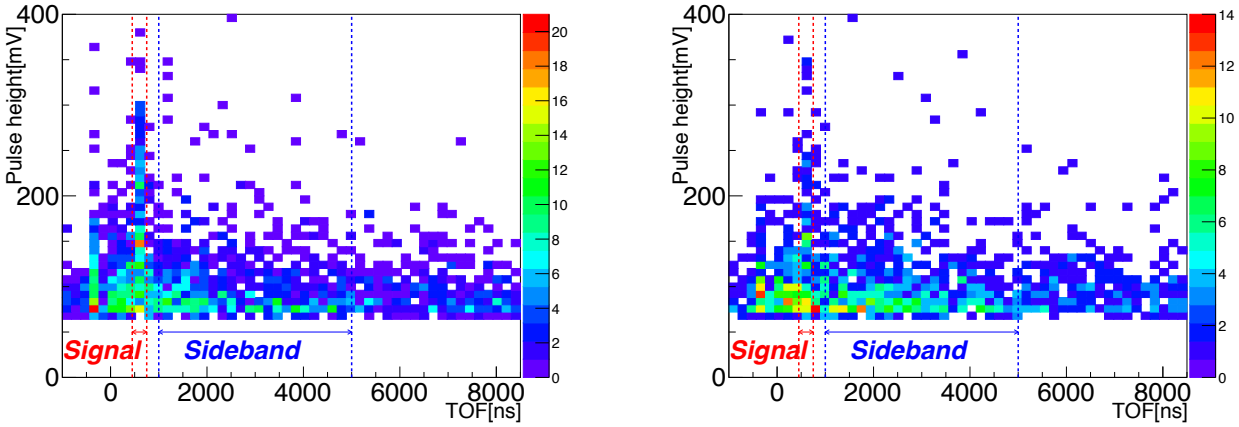

Figure 4.4: Scatter plots of the TOF and pulse height for data of the positive (left) and negative (right) extractions after the time correction.

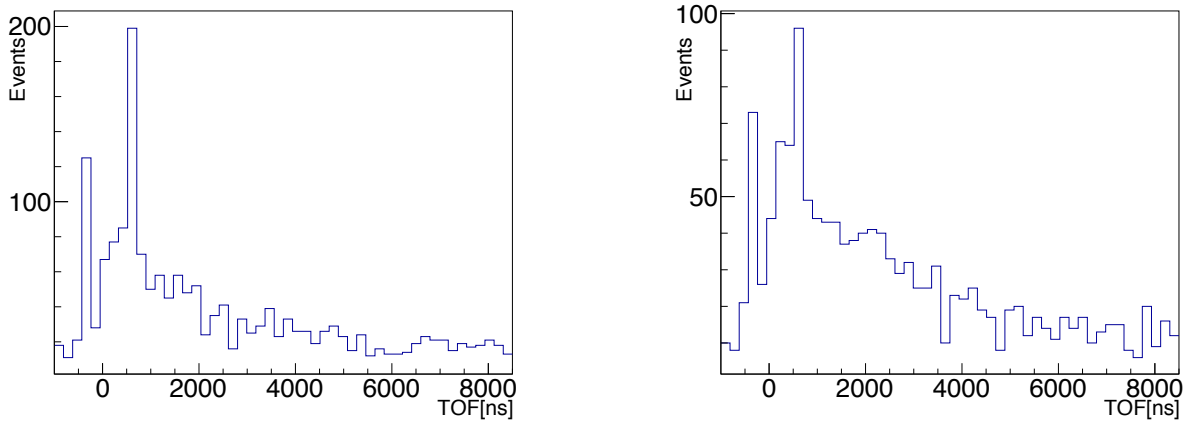

Figure 4.5: TOF distributions for data of the positive (left) and negative (right) extractions after the time correction.

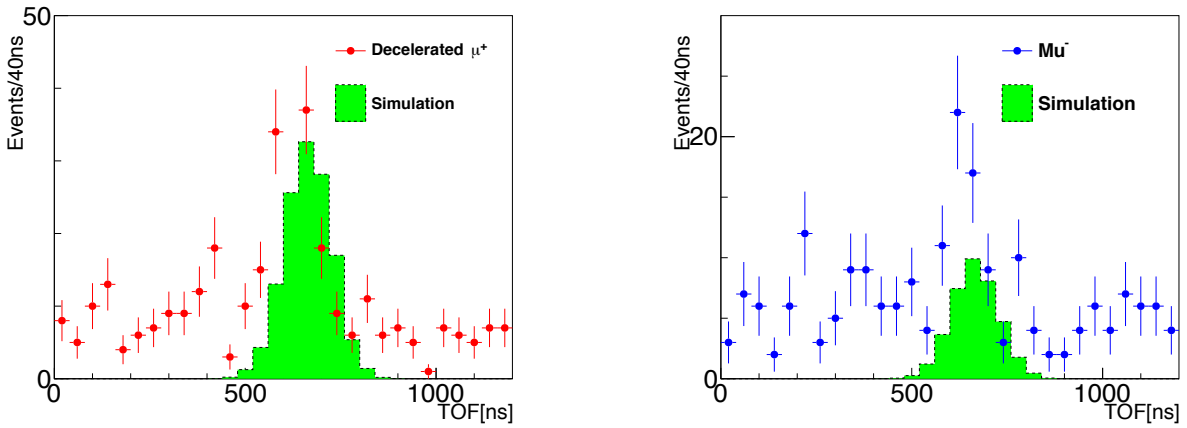

Figure 4.6: TOF distributions for data of the positive (left) and negative (right) extractions after the time correction with the threshold of 100 mV.

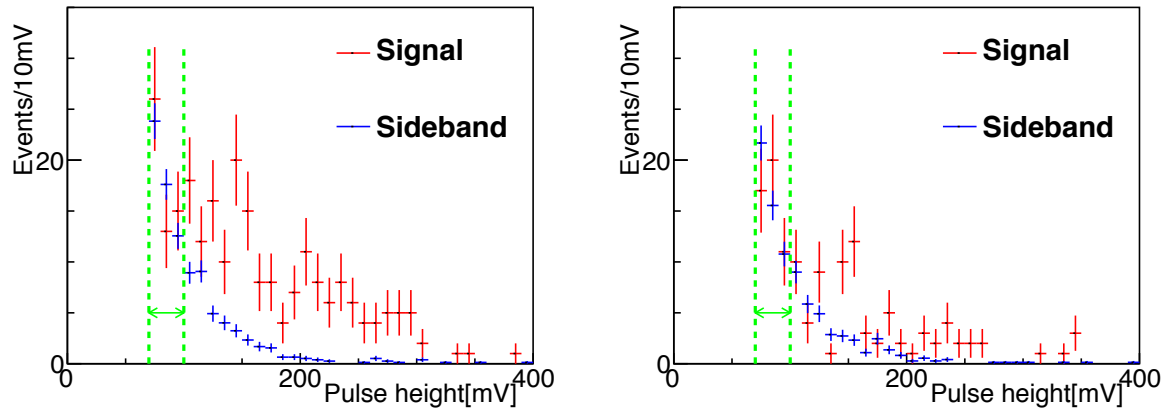

Figure 4.7: Pulse height distributions in the signal region and sideband region for data of positive (right) and negative (left) extractions. Events in the region shown by the green dotted-line were used for the normalization of histograms.

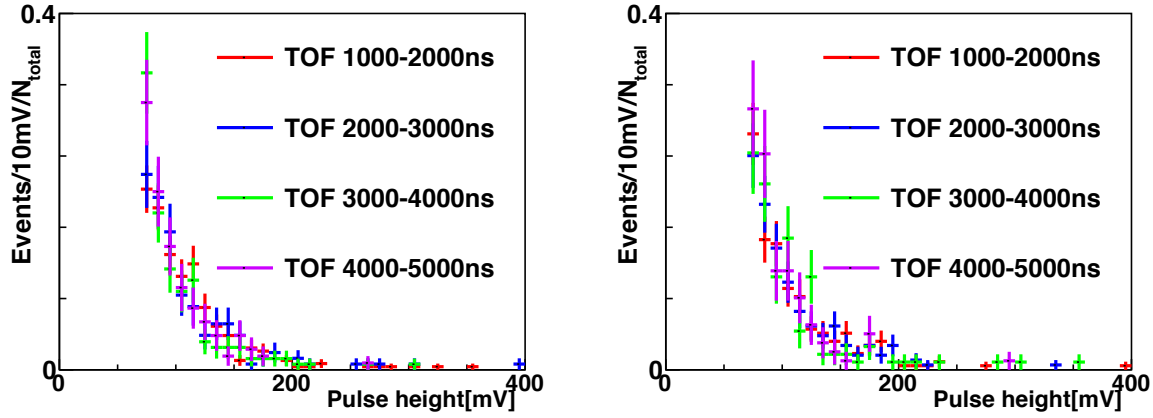

Figure 4.8: Pulse height distributions in the sideband regions every 1000 ns for data of positive (right) and negative (left) extractions.

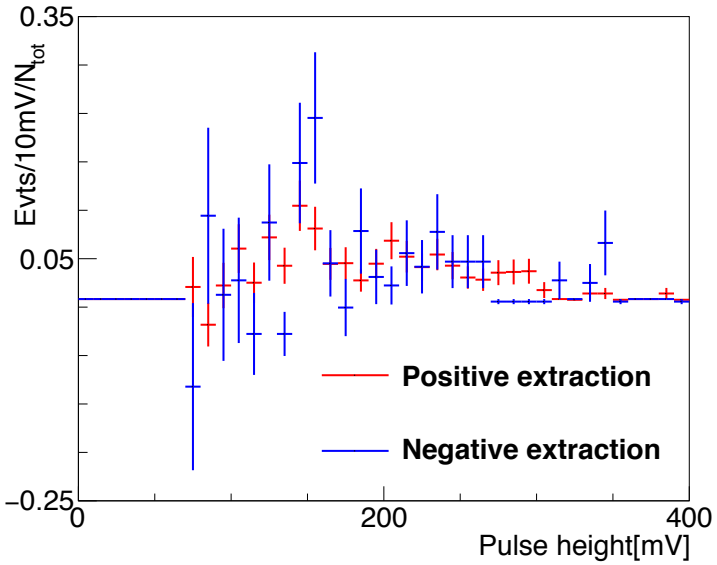

Figure 4.9: Comparison of subtracted pulse height distributions for decelerated μ^+'s and Mu^-'s. The histograms are normalized by the number of total events.

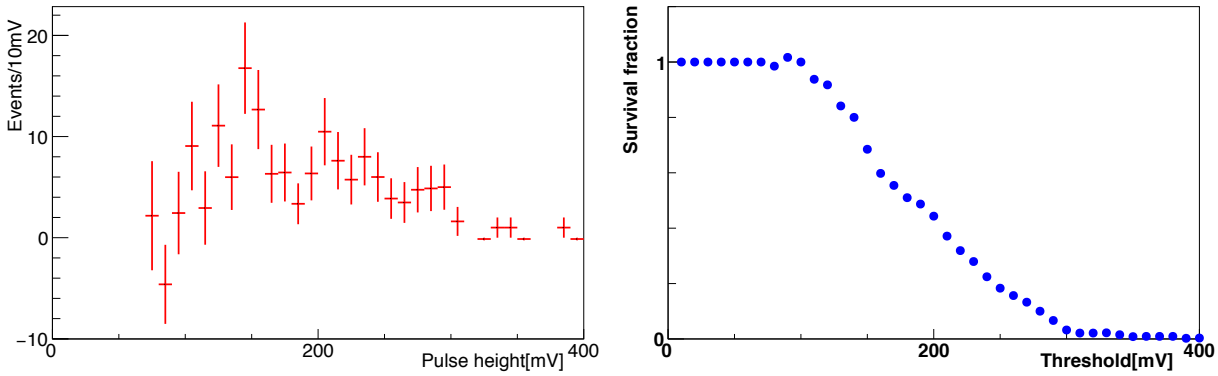

Figure 4.10: Pulse height distribution (left) and survival fraction of the pulse height cut for the positive extraction (right).

4.3 Evaluation of the TOF and the event rate

TOF's and event rates of the decelerated μ^+ and the Mu^- are estimated with the fitting for TOF distributions. The extended log-likelihood method is used to measure the TOF and the number of signal events, that is the event rate of the decelerated μ^+ and the Mu^-, because the number of signal events is small [48]. In terms of the TOF distribution, the likelihood for the fitting using the probability density function is described as

$$L = \frac{\mu^n}{n!}e^{-\mu}\prod_{i=1}^{n} f(t_i; m, \sigma) = \frac{e^{-\mu}}{n!}\prod_{i=1}^{n} \mu f(t_i; m, \sigma), \tag{4.8}$$

where L is the likelihood, μ was the number of expected events, n is the number of observed events, f is the probability density function, m and σ are parameters as follows. Probability density functions of the signal and the background are defined as

$$f_{sig}(t_i; \mu_{sig}, m, \sigma) = \frac{\mu_{sig}}{\sqrt{2\pi\sigma^2}}e^{(-\frac{(t_i-m)^2}{2\sigma^2})} \tag{4.9}$$

$$f_{bg}(t_i; \mu_{bg}) = \mu_{bg}C_{bg}e^{(-\frac{t_i}{\tau})}, \tag{4.10}$$

where

$$C_{bg} = \frac{1}{\tau[e^{(-\frac{t_{min}}{\tau})} - e^{(-\frac{t_{max}}{\tau})}]} \tag{4.11}$$

$$\mu = \mu_{sig} + \mu_{bg} \tag{4.12}$$

$$\mu_{sig} = \int_{t_{min}}^{t_{max}} f_{sig}(t; 1, m, \sigma)dt \tag{4.13}$$

$$\mu_{bg} = \int_{t_{min}}^{t_{max}} f_{bg}(t; 1)dt. \tag{4.14}$$

In equation (4.9) and (4.10), μ_{sig} and μ_{bg} are the number of fitted events of the signal and background, respectively, and m and σ are the mean and the sigma of the Gaussian. In equation (4.11), C_{bg} is the constant to normalize the background function, and t_{min} and t_{max} are the minimum and maximum of the fitting region. In addition, τ is the muon life time. Fitting parameters are μ_{sig}, μ_{bg}, m and σ. Taking the logarithm of the likelihood and dropping constant terms to change the production of the likelihood from the summation of that, the log-likelihood summation is described as

$$\log(L) = -\mu + \sum_{i=1}^{n} log(\mu f(t_i)) = -(\mu_{sig} + \mu_{bg}) + \sum_{i=1}^{n} \log(L_i) \tag{4.15}$$

$$L_i = \mu_{sig} f_{sig}(t_i; 1, m, \sigma) + \mu_{bg} f_{bg}(t_i; 1) \tag{4.16}$$

The minimization function is defined as

$$M \equiv -2\log(L) \tag{4.17}$$

The function M is minimized with the MINUIT software [49]. The MIGRAD algorithm is used as the minimizer for the fitting. The fitting region is set to the region between 100 ns and 2100 ns. Errors of fitting parameters are estimated for one standard deviation. Figure 4.11 shows the fitting result of TOF distributions for the positive extraction and the negative extraction, when the threshold is 100 mV.

The measured TOF's of the decelerated μ^+ and the Mu^- are summarized in table 4.2. From these fitting, the TOF's of the decelerated μ^+ and the Mu^- are evaluated to be 621.9 ±

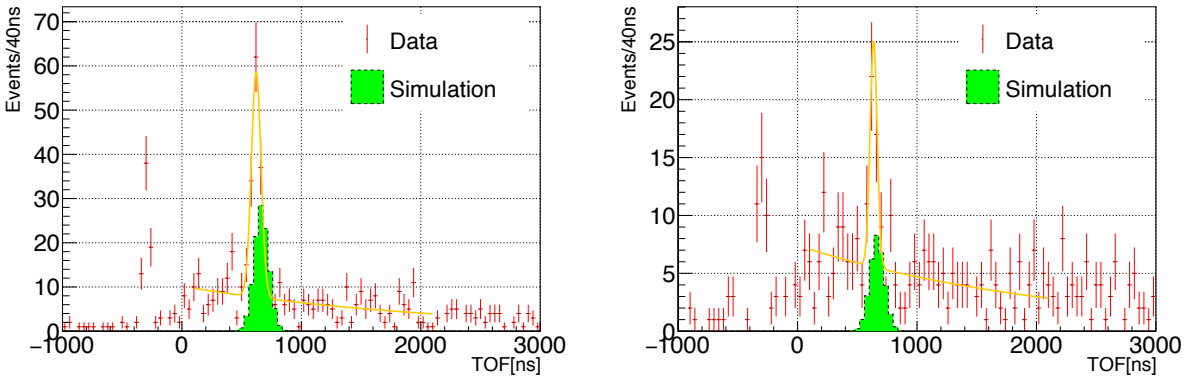

Figure 4.11: Fitting result of TOF distributions for the positive (right) and negative (left) extractions when the threshold was 100 mV. The orange line shows the fitted function.

4.6 ns and 636.9 ± 7.1 ns, respectively. The error of the TOF is calculated as $\Delta t_{\mathrm{TOF}} = \sqrt{(\Delta t_{\mathrm{TOF,fit}})^2 + (\Delta t_{t_0})^2}$, where $\Delta t_{\mathrm{TOF,fit}}$ is the statistical error estimated with the fitting and Δt_{t_0} is the statistical error of the muon arrival time which is determined to be 3.0 ns in section 4.2.1. Therefore, the Δt_{TOF}'s of the decelerated μ^+ and the Mu^- are 5.5 ns and 7.7 ns, respectively. As a result, the measured TOF of the Mu^- was consistent with the measured TOF of the decelerated μ^+. The time difference between the measured TOF's of the decelerated μ^+ or the Mu^-, and the simulated TOF's is approximately 40 ns. The measured TOF's of the decelerated μ^+ and Mu^- are consistent with the simulated TOF's within the precision of 6 %.

The number of the signal events for the Mu^- is evaluated to be 36.6 ± 7.5 events, taking into account the selection efficiency of the pulse height cut. The total number of the triggers for the negative extractions is 5.5×10^5. The repetition rate was 25 Hz. Therefore, the measured event rate of the Mu^- is $(1.7 \pm 0.3) \times 10^{-3}$ /s.

Table 4.2: Measured and simulated TOF's for the decelerated μ^+ and the Mu^-. Simulated TOF of the decelerated μ^+ is described in Appendix D.2.

Data set	Decelerated μ^+	Mu^-
Measured TOF [ns]	621.9 ± 5.5	636.9 ± 7.7
Simulated TOF [ns]	664.5	665.7

4.4 Mu^- production efficiency

Survival fraction of the Mu^- beam up to the detection at the MCP is summarized in table 3.3 using simulations as shown in the chapter 3. The relation between the event rate of the incident surface muons and the measured event rate at the MCP is described as

$$R_{\mathrm{det.}} = R_{\mathrm{inc.}\mu} \times \varepsilon_{\mathrm{tar}} \times \varepsilon_{\mathrm{cool}} \times \varepsilon_{\mathrm{mesh}} \times \varepsilon_{\mathrm{trans.}} \times \varepsilon_{\mathrm{MCP}}, \tag{4.18}$$

where $R_{\mathrm{det.}}$ is the measured event rate of the Mu^- at the MCP, $R_{\mathrm{inc.}\mu}$ is the event rate of the incident surface muons, $\varepsilon_{\mathrm{tar}}$ is the target acceptance, $\varepsilon_{\mathrm{cool}}$ is the cooling efficiency with the Al target, $\varepsilon_{\mathrm{mesh}}$ is the transmission efficiency of the mesh electrode in the Soa lens, $\varepsilon_{\mathrm{trans.}}$ is the transport efficiency of the transport beam line and $\varepsilon_{\mathrm{MCP}}$ is the detection efficiency of the MCP.

Table 4.3 shows the summary of the measurement of the Mu^- in the Mu^- production experiment. Using parameters in table 3.3 and 4.3, the measured cooling efficiency of the Mu^-

are evaluated to be $(1.1 \pm 0.2) \times 10^{-6}$. The error of the measured cooling efficiency comes from the measured event rate. This measured cooling efficiency in the Mu^- production will be used to estimate the expect event rate of the accelerated Mu^- in the muon acceleration experiment.

Table 4.3: Summary of the measurement of the Mu^- in the Mu^- production experiment.

Measured number of events $\mu_{sig,corr.}$	36.6 ± 7.5
Measured event rate $R_{\mathrm{det.}}$ [/s]	$(1.7 \pm 0.3) \times 10^{-3}$
Intensity of the incident μ^+ $R_{\mathrm{inc.}\mu}$ [/s]	1.3×10^6
Total beam transport efficiency $\varepsilon_{\mathrm{target}} \times \varepsilon_{\mathrm{mesh}} \times \varepsilon_{\mathrm{trans.}} \times \varepsilon_{\mathrm{MCP}}$	1.2×10^{-3}
Measured cooling efficiency $\varepsilon_{\mathrm{cool}}$	$(1.1 \pm 0.2) \times 10^{-6}$

Chapter 5

Experimental setup of the muon acceleration experiment

5.1 Overview of the experimental setup

The muon acceleration experiment with the RFQ was carried out at the Muon D-line in the J-PARC MLF. The Mu^- produced from the conventional surface muon beam using the Al target was accelerated with the RFQ to 89 keV. Figures 5.1 and 5.2 show the schematic drawing and the photograph of the setup for the muon acceleration experiment. The setting of the incident surface muon beam, the Mu^- production target and the Soa lens were same as those of the Mu^- production experiment except for the proton beam power. The produced Mu^-'s were accelerated with the Soa lens to 5.6 keV, which is a input energy of the RFQ. Figure 5.3 shows the RFQ used in this experiment. The Mu^-'s accelerated to 89 keV were transported with a diagnostic beam line to the MCP. The diagnostic beam line consists of two quadrupole magnets (QM1 and QM2) and a bending magnet (BM) to select the momentum of the accelerated Mu^-. The same MCP used in the Mu^- production experiment was also used. Table 5.1 shows the experimental condition of the incident surface muon beam in the muon acceleration experiment.

Table 5.1: Experimental condition of the incident surface muon beam in the muon acceleration experiment.

Proton beam power [kW]	319
Muon beam intensity [μ^+/s]	2.5×10^6
Momentum [MeV/c]	25
Repetition [Hz]	25
Pulse mode	Single

5.2 RFQ

A prototype RFQ [50] of the J-PARC H^- linac was used in the muon acceleration experiment, instead of the RFQII. The length of this prototype RFQ is 1973 mm. This length is a half of the completed RFQ. No transition cell is implemented at the downstream end in the vane. Table 5.2 shows the nominal parameters of the RFQ for the muon acceleration. Figure 5.4 shows the cross-sectional drawing of the RFQ. The cavity structure is composed of four vanes, which are made of oxygen free copper and jointed with the laser beam welding method. The π-mode stabilizing loops are employed to stabilize the accelerating mode against a dipole mode

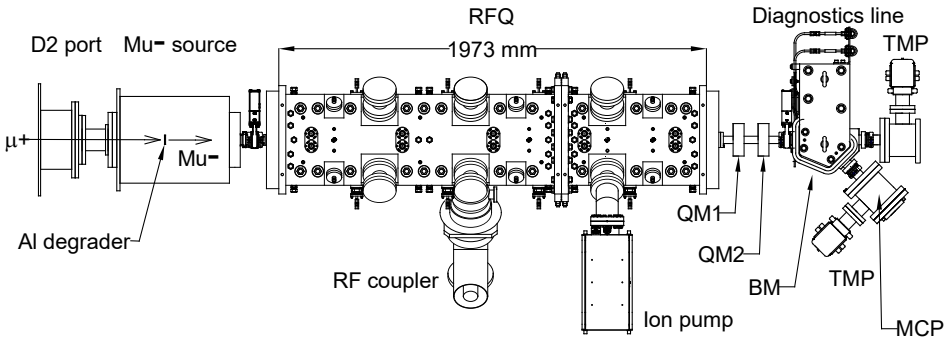

Figure 5.1: Schematic drawing of the muon acceleration experiment with the RFQ. This figure is taken from reference [3].

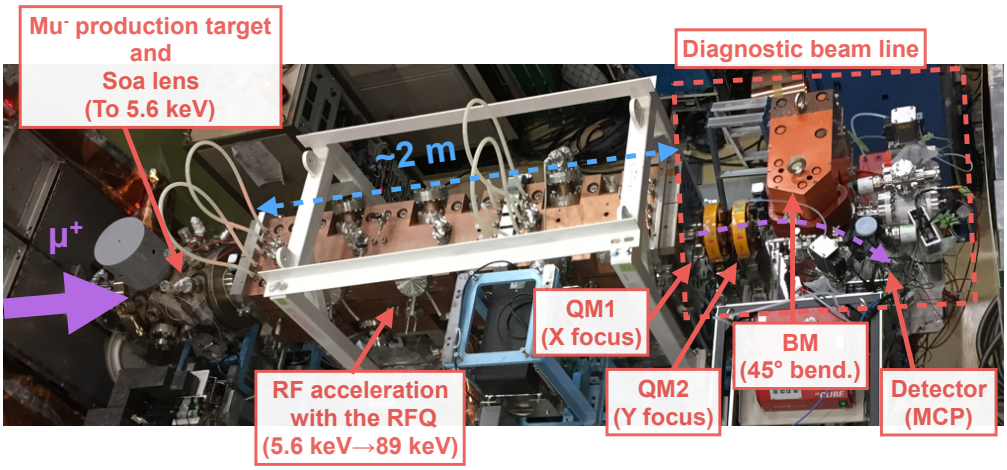

Figure 5.2: Setup of the muon acceleration experiment with the RFQ.

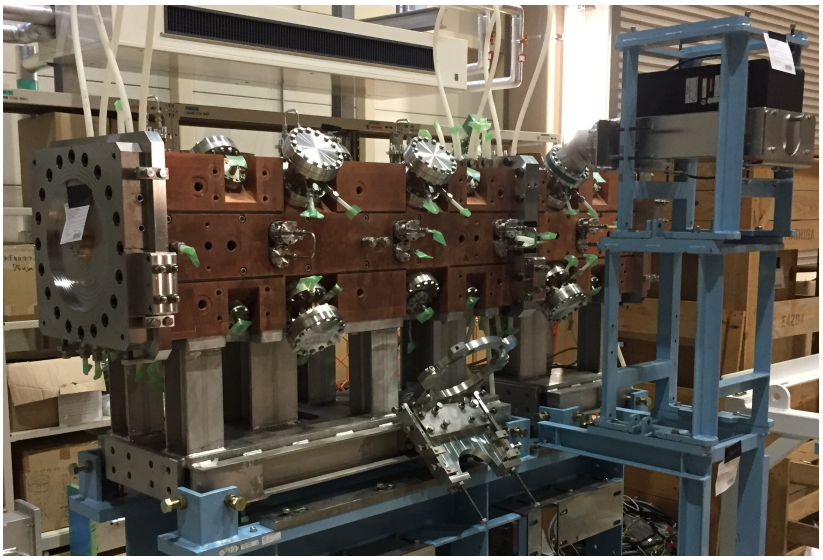

Figure 5.3: RFQ used in the muon acceleration experiment.

mixing. The machining accuracy of the vane tips are within 15 μm. The resonant frequency f_0 and the quality factor Q_0 were confirmed before the muon acceleration experiment. The RF signal is generated using the signal generator (TSG-4104A E1, Tektronix) and amplified with the RF amplifier (CA324BW0.4-6767R(P), R&K). The measured f_0 and Q_0 were 324.017 MHz and 9560, respectively, with vacuum. There was no serious degeneration.

The calculated power dissipation for the full length (3874 mm) RFQ using SUPERFISH [51] is 317 kW. Therefore, the power dissipation of the prototype RFQ is 317 kW$\times$(1973 mm/3874 mm) = 161 kW. The ratio between the calculated an measured Q_0 is 0.84. Thus, the required power for H^- acceleration is estimated to be 192 kW. For the muon acceleration, this power should be scaled by the squared muon mass. Therefore, the required power for the muon acceleration is 2.4 kW. The RF power is supplied to the RFQ through an loop type RF coupler. Figure 5.5 shows the block diagram of the setup to input the RF power into the RFQ.

Figure 5.6 shows the waveform of the RF input into the RFQ. The pulse with of the RF was set to 100 μs, which was enough longer than the pulse width of the Mu^- beam, because the pulse widths of the incident muons and the extracted Mu^-'s were about 40 ns (rms).

5.3 Diagnostic beam line

The accelerated Mu^-'s with the RFQ were transported with the diagnostic beam line. Figure 5.7 shows the photograph of the diagnostic beam line.

5.3.1 Quadrupole magnet

Accelerated Mu^- beam was focused with two quadrupole magnets (QM's); QM1 and QM2 having identical specifications. The QM1 focuses the beam in a x direction, while the QM2 focuses the beam in a y direction. Figure 5.8 and table 5.3 show the photographs and the parameters of the QM. The magnetic field distribution along the beam axis of the QM was measured with a Hall probe to evaluate the effective length of the QM. Figure 5.9 shows the measured magnetic field distribution and the simulated magnetic field distribution with OPERA TOSCA [47]. The

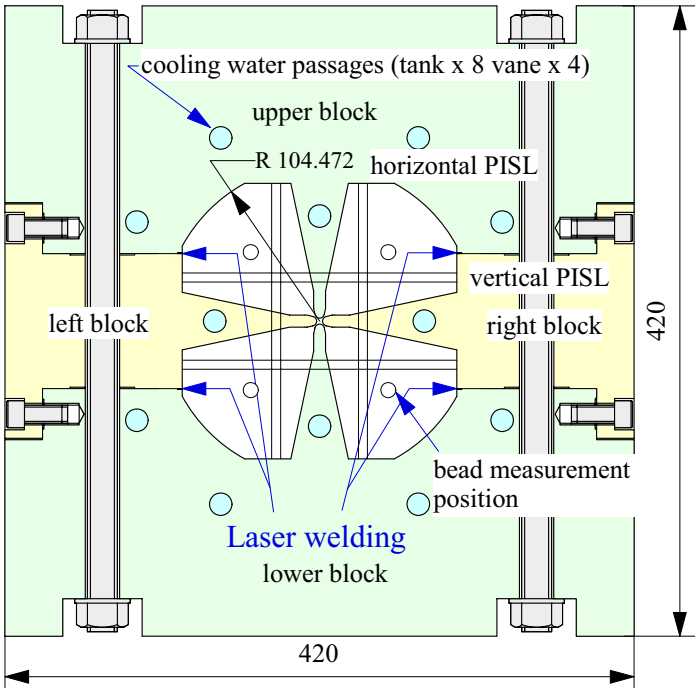

Figure 5.4: Cross-sectional drawing of the prototype RFQ. This figure is taken from reference [50].

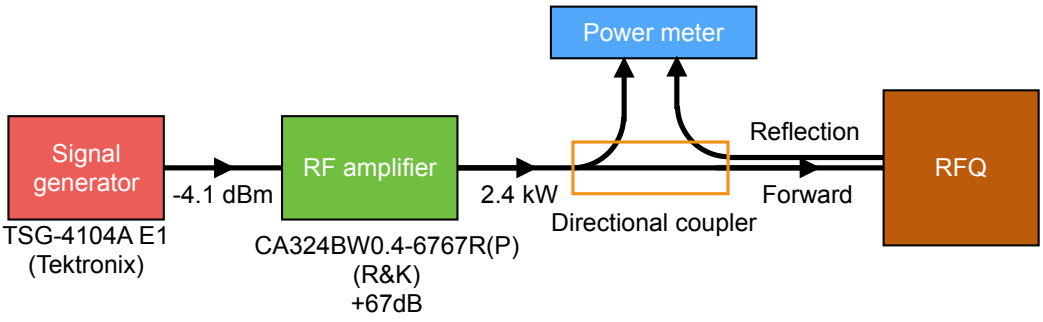

Figure 5.5: Block diagram of the RF system for the RFQ.

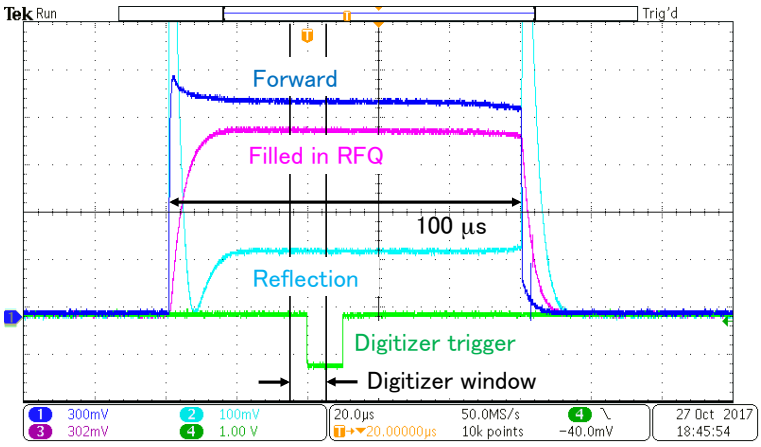

Figure 5.6: Waveform of the RF input into the RFQ. This figure is taken from reference [3].

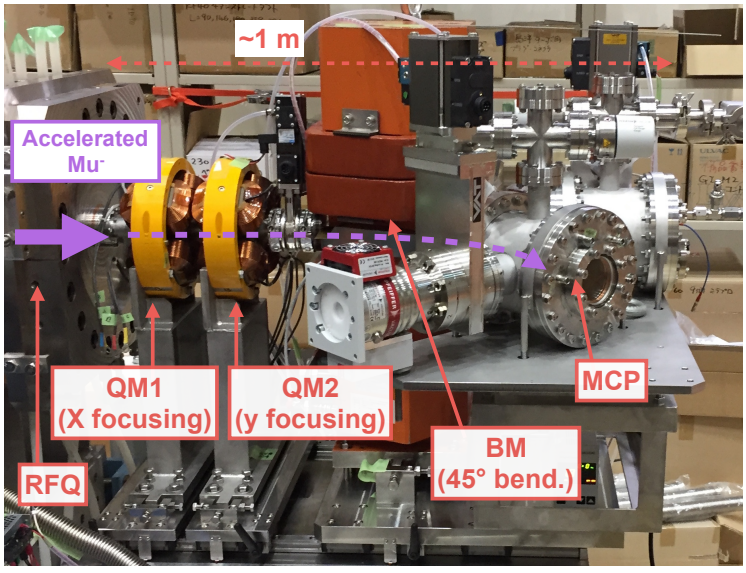

Figure 5.7: Photograph of the diagnostic beam line after the RFQ.

Table 5.2: Nominal parameters of the RFQ used in the muon acceleration experiment.

Cavity structure	4-vane
Resonant frequency	324 MHz
Length	1973 mm
Number of cells	297
RF power	2.4 kW
Inter vane voltage	9 kV
Average bore radius	3.6 mm
Input – output β	0.01 – 0.04
Transmission*	100 %
Transverse emittance* (normalized, rms)	0.19π mm mrad
Longitudinal emittance* (normalized, rms)	0.029π MeV deg

*PARMTEQM calculation(1.0π mm mrad (100 %, normalized, warterbag) injection)

origin of the z axis is the center of the QM. The measured field distribution was consistent with the simulated field distribution. The effective length is defined as

$$L_{eff} = \frac{1}{B_0} \int_{-\infty}^{\infty} B(z) dz, \tag{5.1}$$

where z is the position on the beam axis, B_0 is the peak value of the magnetic field and $B(z)$ is the measured magnetic field as a function of z [52]. The effective length of the QM was evaluated to be 76 mm.

The field gradient of the QM was also measured with the Hall probe. Figure 5.10 shows the measured magnetic field distributions of the QM along the horizontal and vertical axis on the central plain of the QM. The origin of the y or x axis is the center of the QM. The field gradient was evaluated to be 900 Gauss/mm with an applied current of 4 A from the fitting to the field-gradient distribution.

Table 5.3: Parameters of the QM used in the muon acceleration experiment.

Effective length [mm]	76
Aperture diameter [mm]	17
Number of the turn [Turn/pole]	280
Field gradient [Gauss/mm]	900 (at 4 A)
Resistance [Ω]	1.9
Cooling	Air cooling

5.3.2 Bending magnet

Figure 5.11 and table 5.4 show the drawing and the parameters of the bending magnet (BM). The effective length of the BM was evaluated from the magnetic field distribution along the beam axis, which was shown as figure 5.12. The effective length of the BM was evaluated to

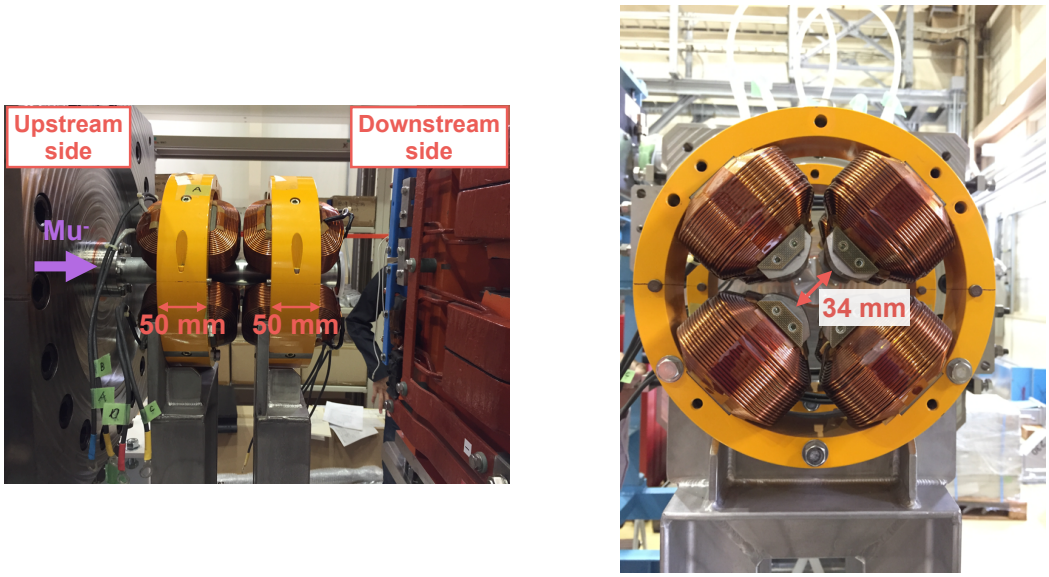

Figure 5.8: QM's in the diagnostic beam line.

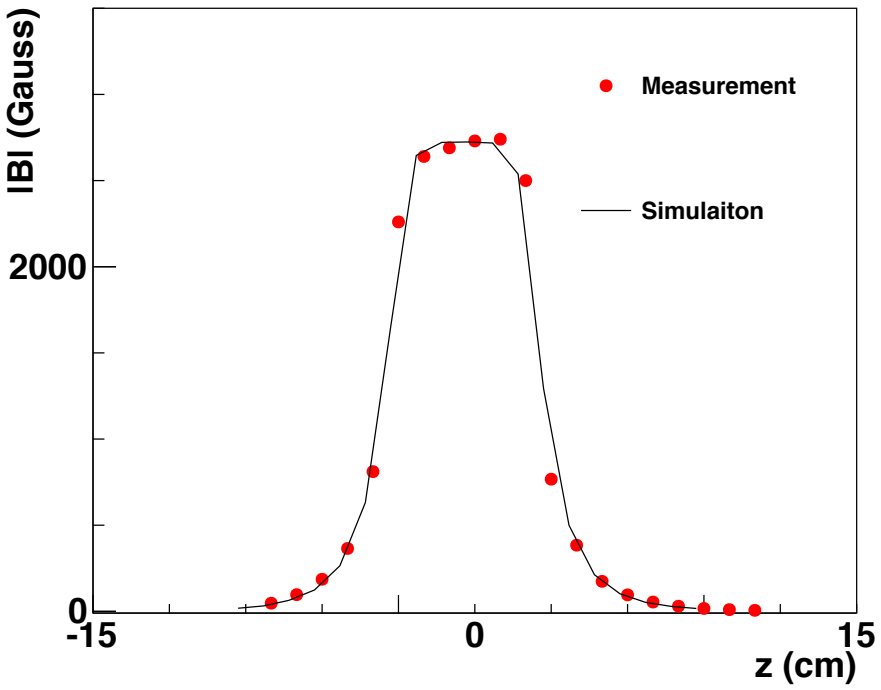

Figure 5.9: Magnetic field distribution of the QM along the beam axis [53].

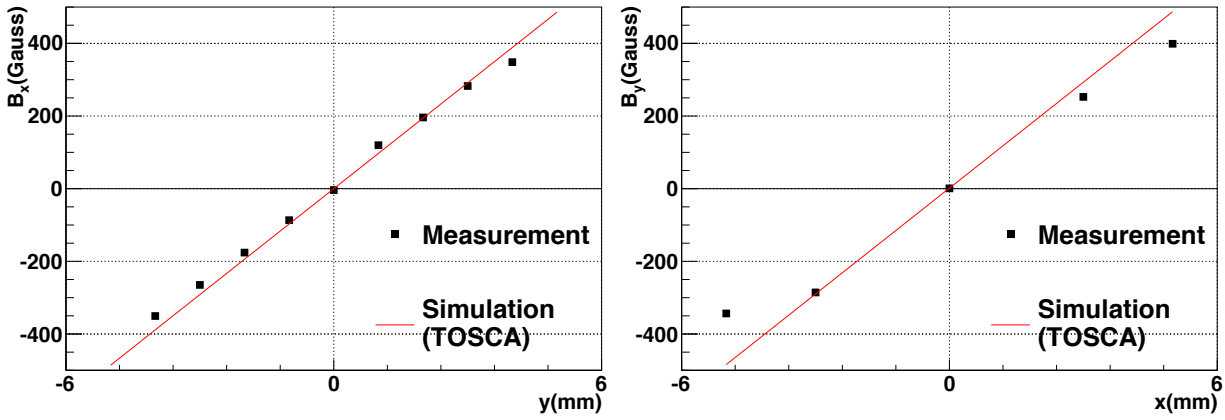

Figure 5.10: Magnetic field-gradient distributions of QM's [53], where x is the horizontal axis and x is the vertical axis. The B_y component along the x direction (left) and the B_x component along the y direction (right) on the central plain of the QM.

be 273.9 mm using equation (5.1) by integrating the measured field distribution. The relation between the current and the field is 275 A/Tesla from the measurement of the field strength. Since the momentum of the accelerated Mu^- is $p_{\mathrm{acc.}} = 4.3$ MeV/c, the required field strength is $2\pi p_{\mathrm{acc.}}/0.3L_{eff}(360°/45°) = 410$ Gauss. Therefore, the required current is 0.0410 Tesla×(275 A/Tesla) = 11.3 A.

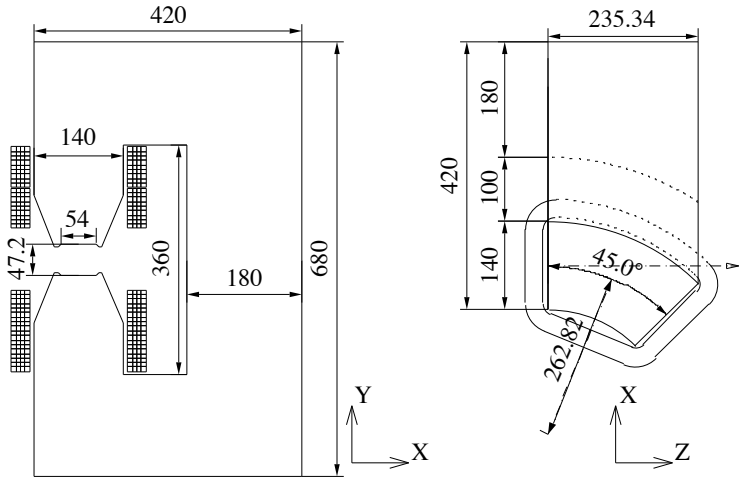

Figure 5.11: Drawing of the BM. This figure is taken from reference [54].

5.4 Detector, remote control system and vacuum system

The single-anode MCP and the BPM were also used as the detector in the muon acceleration experiment, which had been used in the Mu^- production experiment. The single-anode MCP was used in the measurement of the accelerated Mu^-. The BPM was used in the commissioning of the diagnostic beam line with the H^- beam.

The applied voltage and currents to the Soa lens, the QM's and the BM are controlled using the PLC's. The vacuum system consists of three sections; the target section, the RFQ section

Table 5.4: Parameters of the BM used in the muon acceleration experiment.

Effective length [mm]	273.9
Bend angle [degree]	45
Radius of curvature [mm]	262.82
Gap (shim gap) [mm]	47.20 (42.48)
Turn number of coil [Turn/pole]	72
Resistance [mΩ]	103.02
Cooling	Air cooling

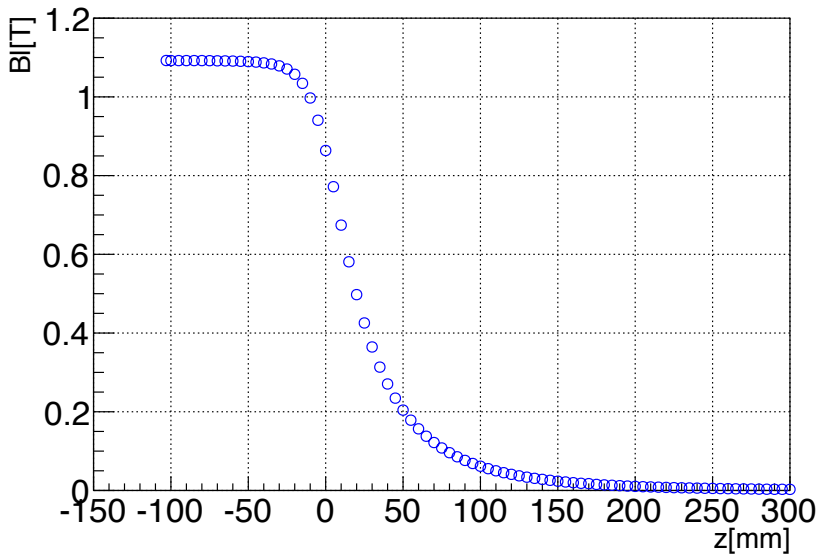

Figure 5.12: Longitudinal magnetic-field distribution of the BM.

and the detector section. Figure 5.13 and table 5.5 show the block diagram of the vacuum system and the list of vacuum pumps in the muon acceleration experiment, respectively.

Table 5.5: List of the vacuum pumps in the muon acceleration experiment.

ID	Model	Pumping speed [L/s]	Typical pressure [Pa]
TMP1	Pfeiffer TMU 520	500	4.2×10^{-5}
TMP2	Pfeiffer HiCube Eco 80	35	7.9×10^{-6}
Ion pump	Gamma vacuum Titan 200T	200	2.0×10^{-5}

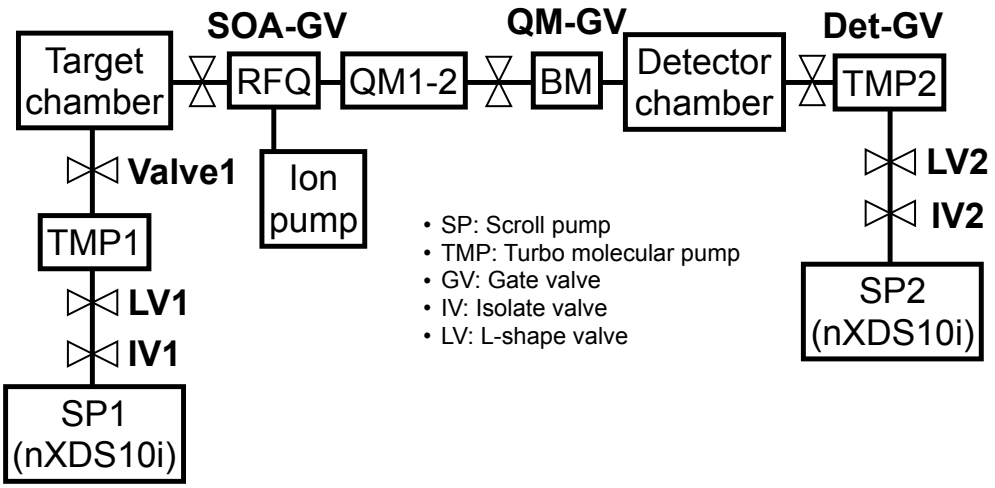

Figure 5.13: Block diagram of the vacuum system.

Chapter 6

Simulation of the muon acceleration experiment

The simulation of the muon acceleration experiment is described in this chapter. This simulation aims to evaluate the event rate at the MCP and the TOF for the Mu^- accelerated with the RFQ.

6.1 Incident surface muon beam and the production of the Mu^-

The setting of the D-line, the Mu^- production target and the Soa lens in the muon acceleration experiment were same as those in the Mu^- production experiment except for the proton beam power. The target acceptance, 2.4×10^{-1}, evaluated in chapter 3 is used. The initial phase-space distributions of the Mu^-'s at the Mu^- production target are used to evaluate beam transport efficiencies to the MCP. The cooling efficiency of the Mu^- with the Al target, which is evaluated to be $(1.1 \pm 0.2) \times 10^{-6}$ in chapter 4, is used to evaluate the expected event rate of the accelerated Mu^-.

6.2 RFQ injection

The beam transport of the Mu^- is simulated from the Mu^- production target to the entrance of the RFQ. The acceleration of the Soa lens simulated using musrSim [46]. Figure 6.1 shows the schematic of the Soa lens modeled in musrSim. Table 6.1 shows the applied voltage to the electrodes of the Soa lens in the muon acceleration experiment. The applied voltage to accelerate Mu^- is 5.6 kV, which is same as the nominal input energy of the RFQ, because the initial kinetic energy of the Mu^- at the Mu^- production target is in the vicinity of 0 keV. Figures 6.2 and 6.3 show simulated profiles and phase-space distributions of the Mu^- at the entrance of the RFQ, respectively. Table 6.2 shows the numbers of the generated events at the Mu^- production target and transported events at the entrance of the RFQ for the Mu^- estimated with musrSim. The transport efficiency of the Soa lens for the Mu^- is 5.2×10^{-2}. Since the phase space of the Mu^- at the entrance of the RFQ is larger than the input acceptance of the RFQ, some of the Mu^-'s are out of the acceptance of the RFQ. They are lost with the next simulation of the RFQ.

6.3 RFQ simulation

The RF acceleration in the RFQ is simulated with PARMTEQM [55]. Parts of the generated events of the Mu^- in the previous section are used for the RFQ simulation. Figure 6.4 shows the evolution of the phase-space distributions of the Mu^- in the RFQ.

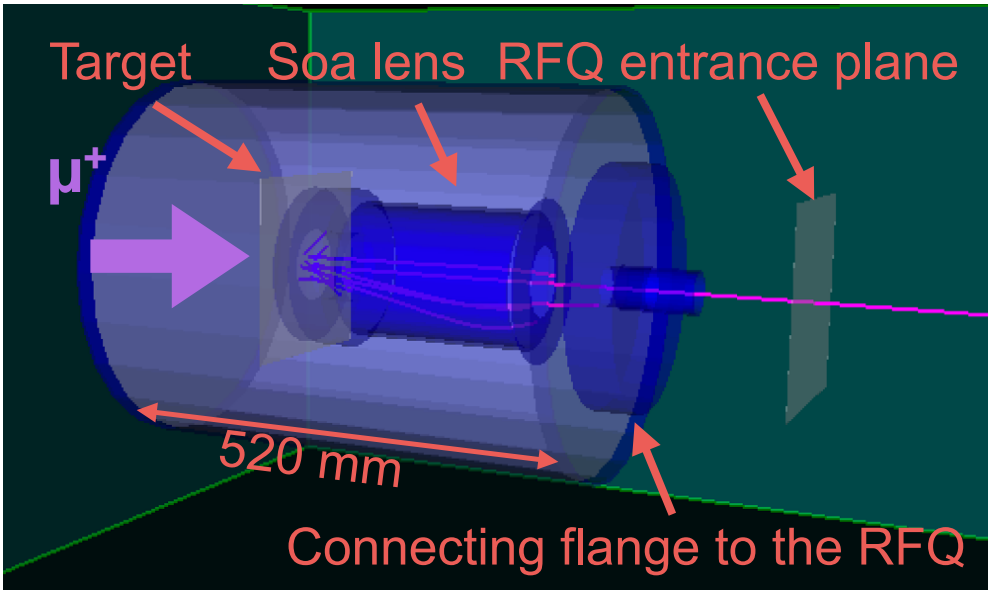

Figure 6.1: Schematic of the Soa lens modeled in musrSim.

Table 6.1: Applied voltage to electrodes of the Soa lens.

Polarity	Negative extraction
T [kV]	5.6
S1 [kV]	5.3
S2 [kV]	5.1
S3 [kV]	4.5

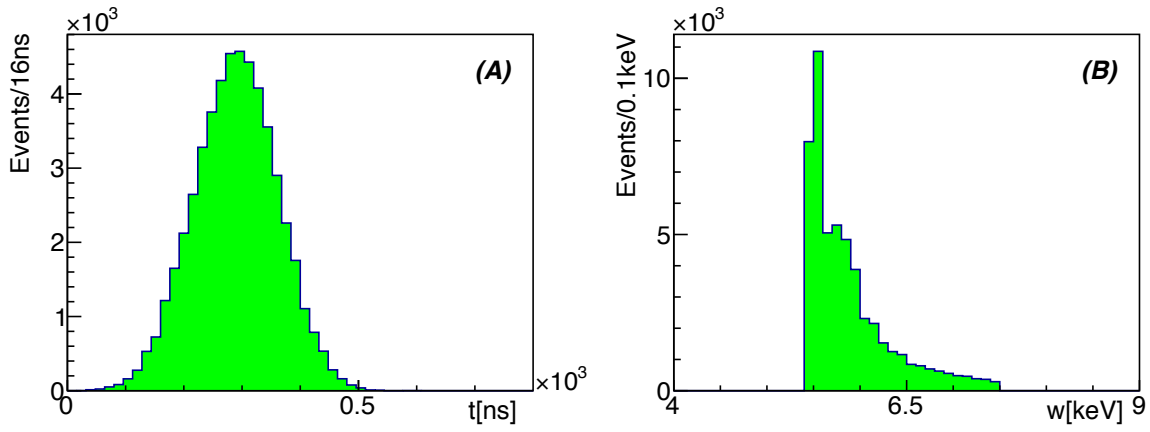

Figure 6.2: Simulated profiles at the entrance of the RFQ with the Mu^-. (A) time of flight from the production target to the entrance of the RFQ, (B) the kinetic energy w.

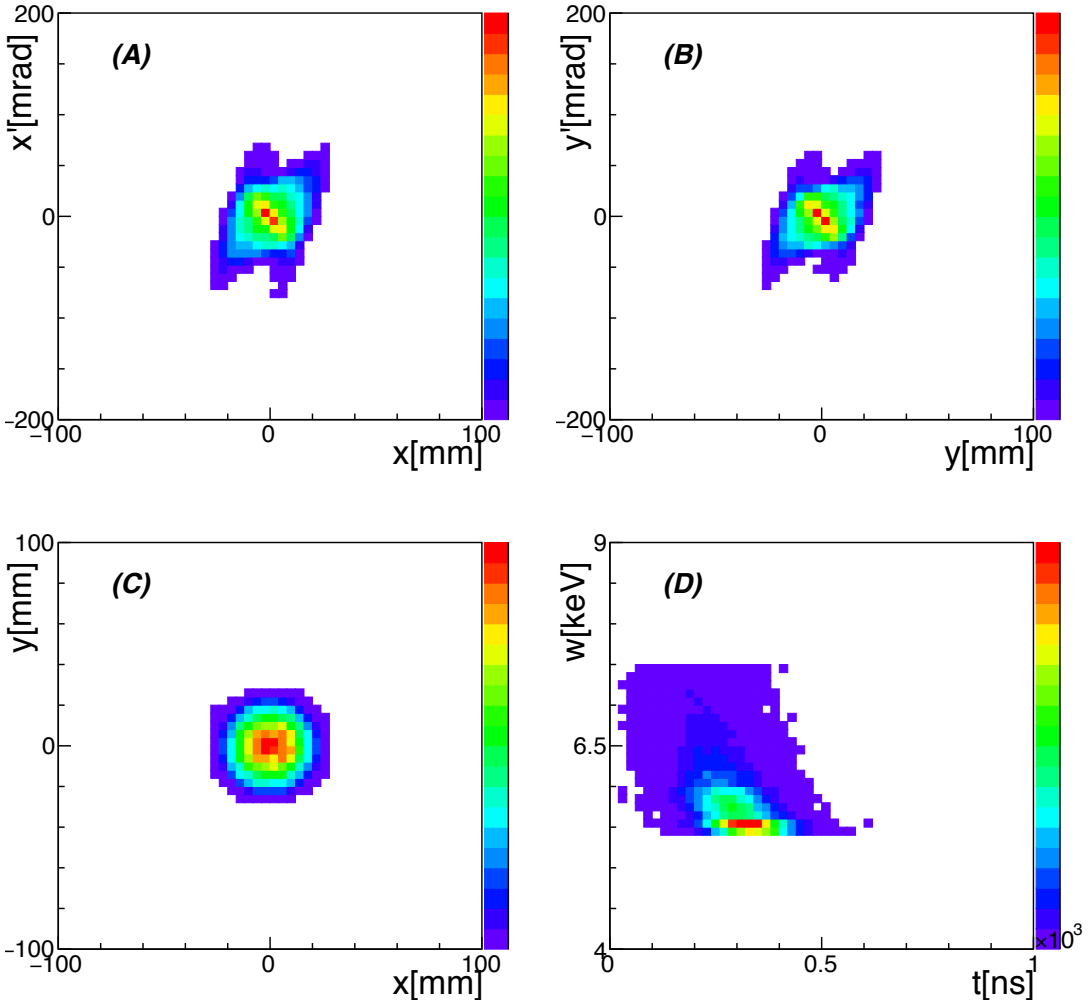

Figure 6.3: Simulated phase-space distributions at the entrance of the RFQ with the Mu^-. (A) the horizontal divergence angle x' vs the horizontal position x, (B) the vertical divergence angle y' vs vertical position y, (C) y vs x, and (D) the kinetic energy vs the time of flight from the production target to the entrance of the RFQ.

Table 6.2: Numbers of the generated events at the Mu^- production target and transported events at the entrance of the RFQ for the Mu^- estimated with musrSim.

N_{gen}	1×10^6
N_{RFQin}	51815

As described in chapter 5, this RFQ is a prototype of the J-PARC RFQ and it corresponds to a half of the complete RFQ for the J-PARC H^- linac [50]. To match the vane length to the cavity length, the last accelerating cell is just extended without modulation; PARMTEQM can't simulate such structure. Therefore, the partilcle simulation in this region is performed using General Particle Tracer (GPT) [56]. First, the structure of this exit-end section is modeled using Autodesk Inventor [57]. Figure 6.5 shows the three-dimensional structure of the exit-end section. The generated three-dimensional structure is implemented to CST EM STUDIO [58]. The calculated electric-field map is used for the GPT simulation. The output of the phase-space distributions from PARMTEQM is used as the input for the GPT simulation. Accelerated Mu^-'s in RFQ are slightly decelerated with the electric field generated in the exit-end section. Therefore, the output kinetic energy of the accelerated Mu^- with the RFQ is 89 keV from results of PARMTEQM and GPT. Figures 6.6 and 6.7 show the simulated phase-space distributions for the Mu^- at the exit of the RFQ. Table 6.3 shows N_{RFQin} and N_{RFQout}, which are the numbers of events at the entrance of the RFQ and at the exit of the RFQ, respectively. The transport efficiency of the Mu^- is 5.5 % including the aperture losses at the entrance of the RFQ.

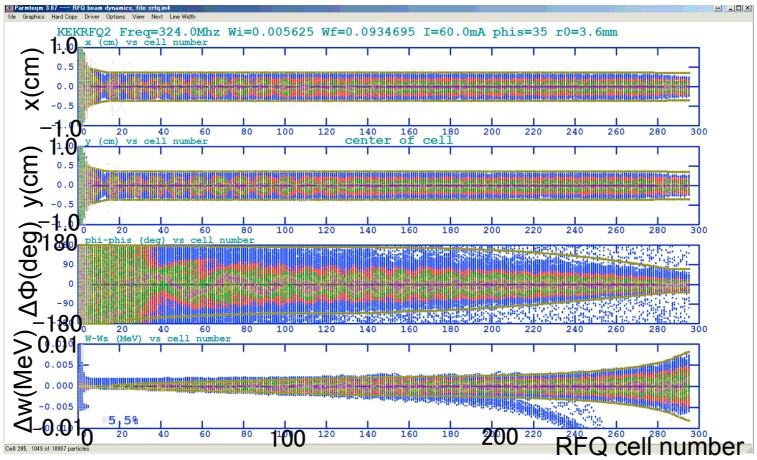

Figure 6.4: Simulation result with PARMTEQM for the Mu^- in the RFQ.

Table 6.3: Number of events at the entrance of the RFQ, N_{RFQin} and the number of events at the exit of the RFQ, N_{RFQout} for the Mu^- estimated with PARMTEQM and GPT.

N_{RFQin}	18967
N_{RFQout}	1044

6.4 Diagnostic beam line

The beam envelope in the diagnostic beam line is simulated with TRACE3D [59]. Figure 6.8 shows the result of the beam envelop simulation with TRACE3D. Field gradients for two quadrupole magnets are determined from the result with TRACE3D to transport the Mu^- effectively. The particle simulation in the diagnostic beam line is simulated with PARMILA [60]. Figures 6.9 and 6.10 show phase-space distributions of the Mu^- simulated with PARMILA at the MCP detector. Table 6.4 shows the number of events at the exit of the RFQ, N_{RFQout}, and the number of events at the MCP for the Mu^-, N_{MCP}, estimated with PARMILA. The transport efficiency for the Mu^- in the diagnostic beam line is 89 %.

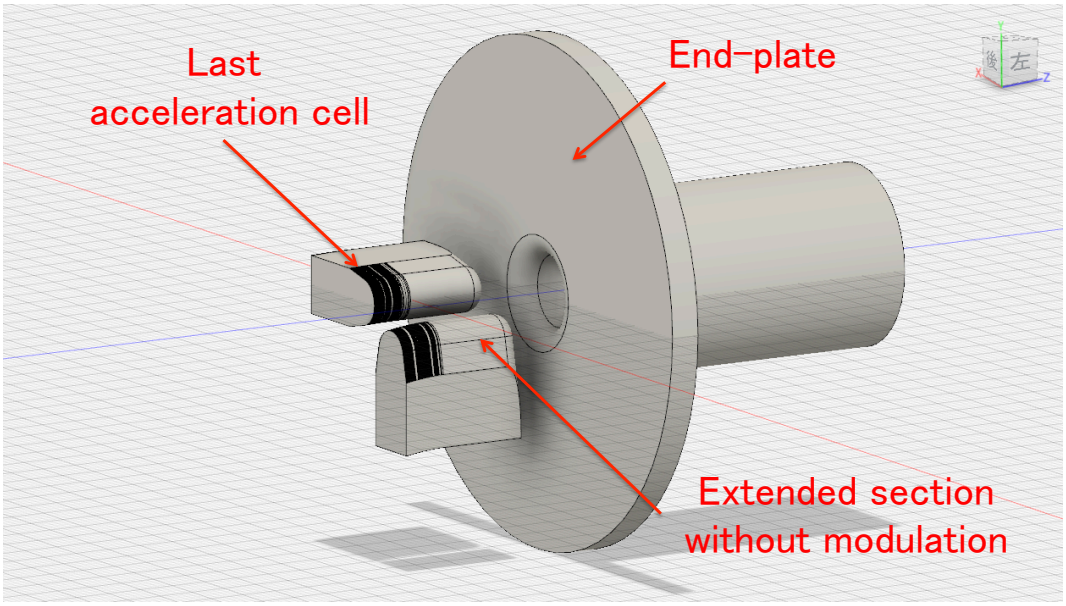

Figure 6.5: Structure built of the downstream end section of the RFQ in Autodesk Inventor.

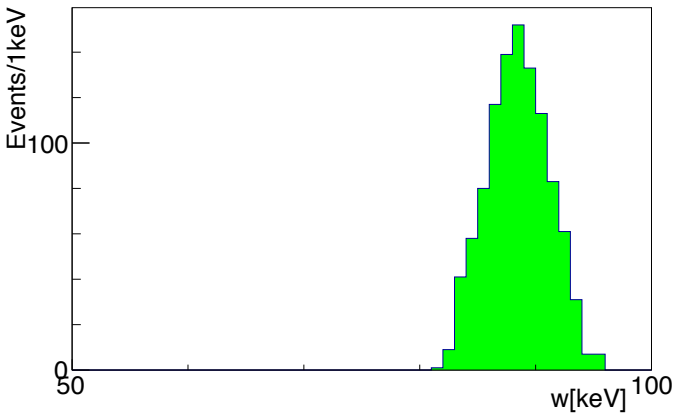

Figure 6.6: Simulated kinetic energy distribution for the Mu^- at the end of the RFQ.

Table 6.4: Number of events at the exit of the RFQ, N_{RFQout} and number of events at the MCP for the Mu^-, N_{MCP} estimated with PARMILA.

N_{RFQout}	1044
N_{MCP}	924

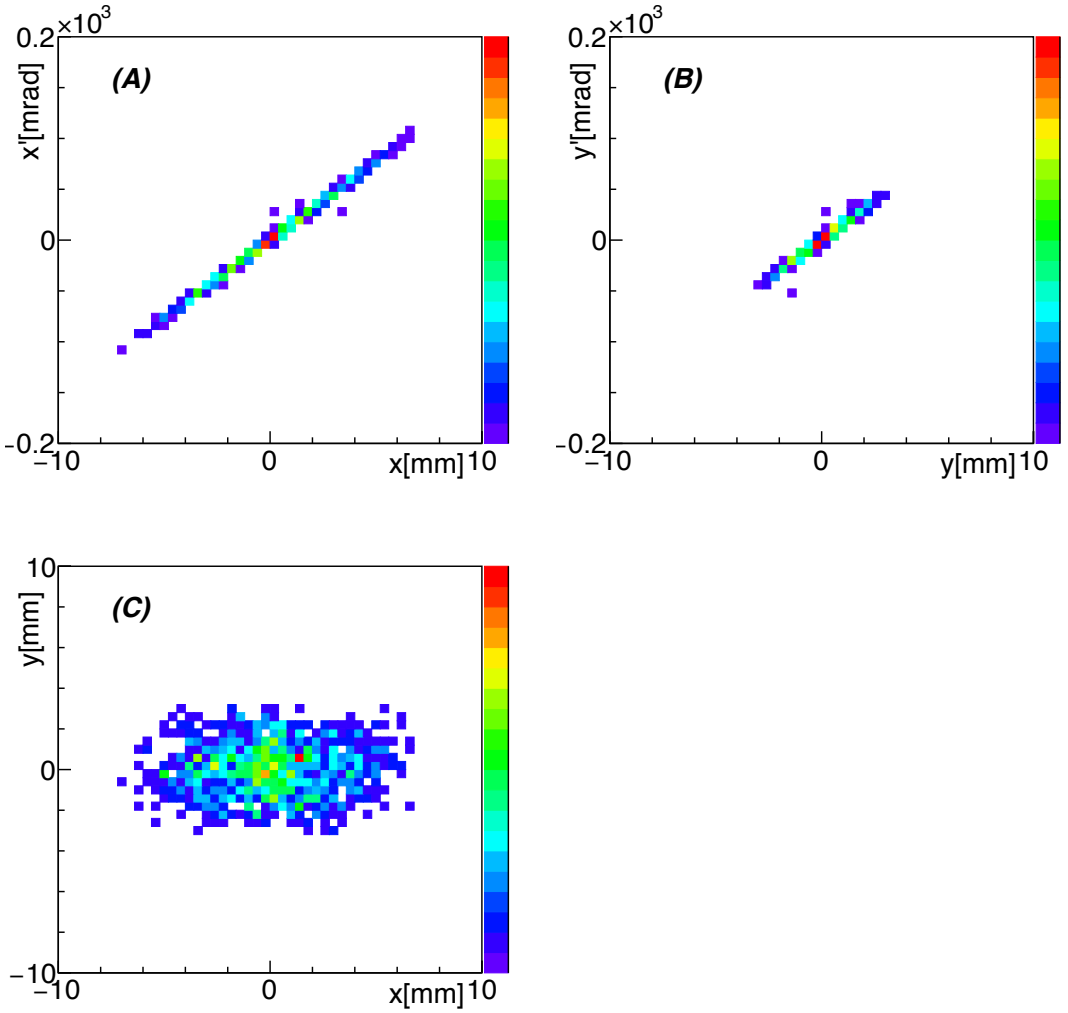

Figure 6.7: Simulated phase-space distributions or the Mu^- at the end of the RFQ. (A) the horizontal divergence angle x' vs the horizontal position x, (B) the vertical divergence angle y' vs vertical position y, and (C) y vs x.

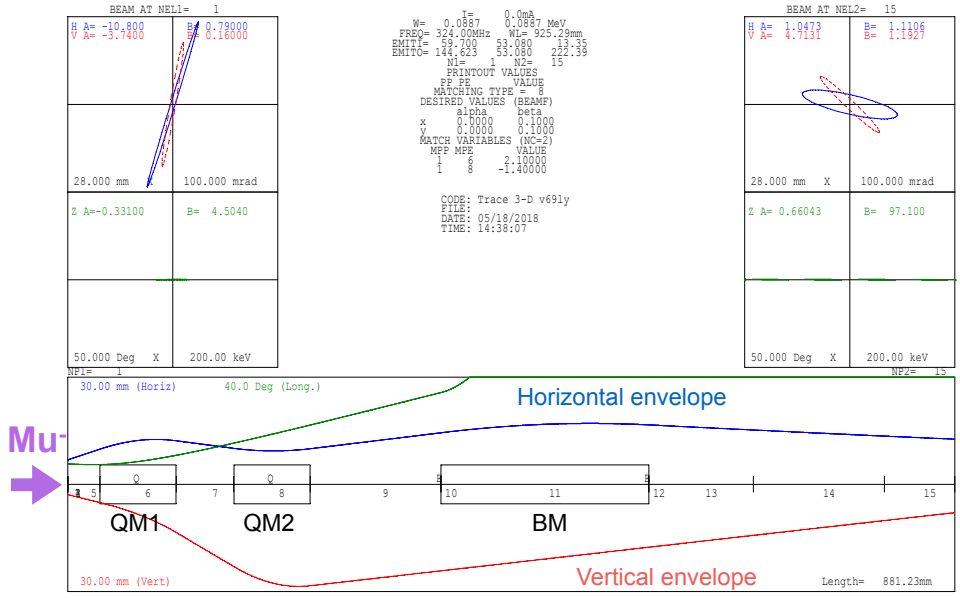

Figure 6.8: Envelope simulation with TRACE3D for the diagnostic beam line.

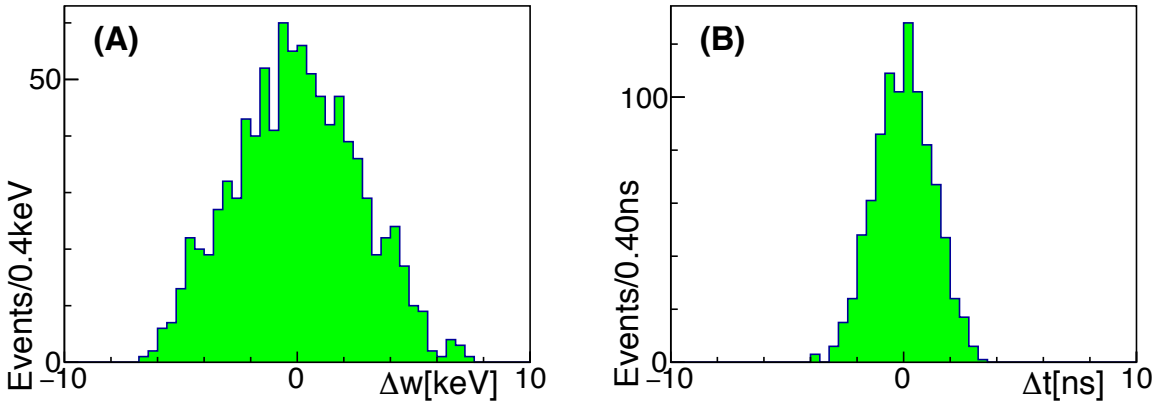

Figure 6.9: Phase-space distributions of the Mu^- simulated with PARMILA at the MCP detector. (A) the displacement from the mean kinetic energy Δw, and (B) the displacement from the mean time Δt.

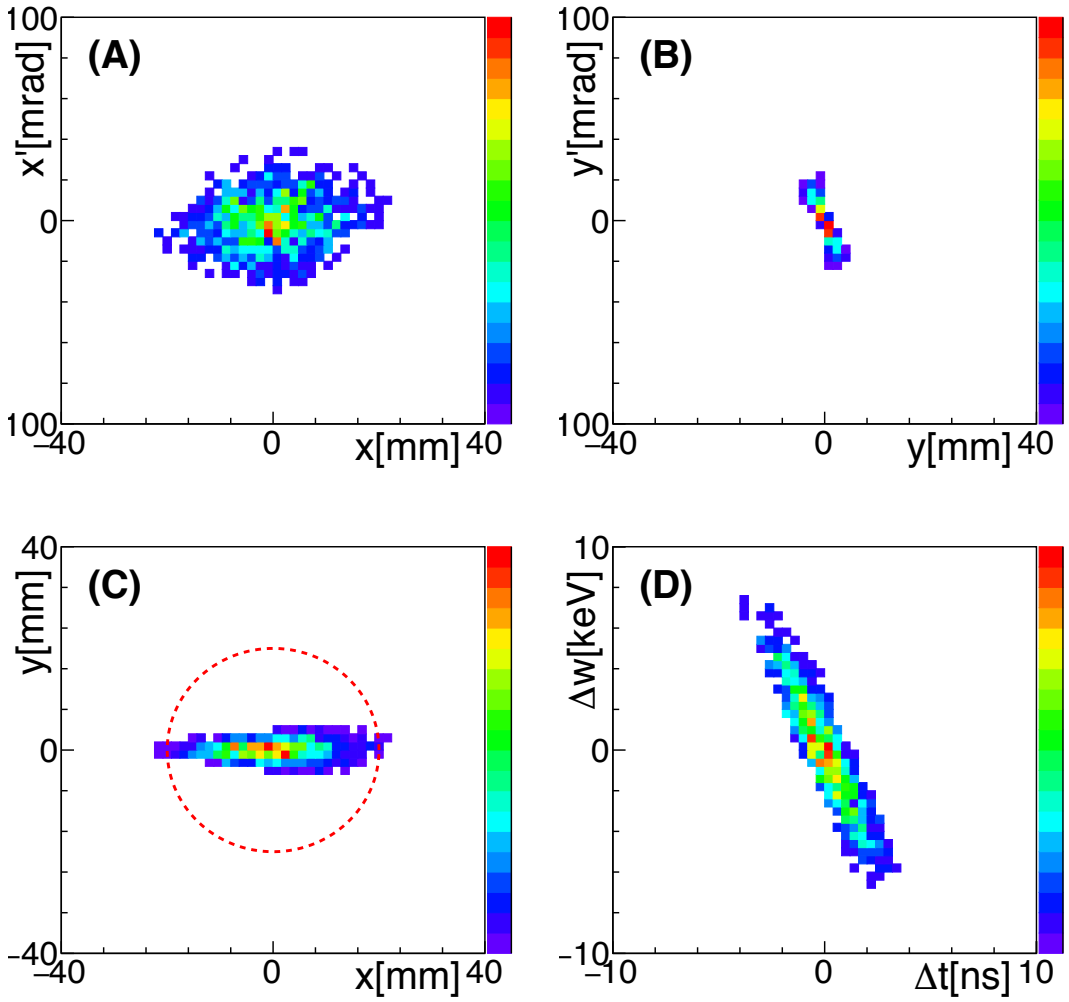

Figure 6.10: Phase-space distributions of the Mu^- simulated with PARMILA at the MCP detector. (A) the horizontal divergence angle x' vs the horizontal position x, (B) the vertical divergence angle y' vs vertical position y, (C) y vs x, and (D) the displacement from the mean kinetic energy, ΔW vs the displacement from the mean time Δt. Red dotted circle shows the effective area of the MCP.

6.5 Summary of the muon acceleration simulation

6.5.1 TOF

The TOF from the Mu^- production target to the MCP for the Mu^- is estimated from results of the simulations. First, the TOF from the Mu^- production target to the entrance of the RFQ is simulated with musrSim. The TOF's of the Mu^- is 289.3 ns. Second, since the length of the unit cell in the RFQ is $\beta\lambda/2$, the TOF in the RFQ is calculated as

$$t_{\mathrm{RFQ}} = \frac{1}{2f}\frac{1}{N_{\mathrm{cell}}}, \tag{6.1}$$

where f is the RF frequency and N_{cell} is the number of the cell in the RFQ. The TOF in the RFQ is estimated to be 455.4 ns, because f is 324 MHz and N_{cell} is 295. The TOF in the exit-end section of the RFQ, which is calculated with GPT, is 5.2 ns. Finally, the TOF in the diagnostic beam line is calculated from the output β of the μ^+ or Mu^- and the length of the diagnostic beam line. Since the length of the diagnostic beam line on the beam axis, $L_{\mathrm{diag.}}$ is 771.5 mm and the output β of the accelerated μ^+ or Mu^- is 0.041, the TOF in the diagnostic beam line is

$$t_{\mathrm{diag.}} = \frac{L_{\mathrm{diag.}}}{\beta} = 63.2 \text{ ns}. \tag{6.2}$$

Therefore, the total TOF of the Mu^- is 813.1 ns as shown in table 6.5.

6.5.2 Event rate

An event rate of the Mu^- is evaluated using results of the simulations. Table 6.6 shows the summary of the estimated beam losses in the muon acceleration simulation. The cooling efficiency of the Mu^-, the mesh transmission efficiency and the detection efficiency of the MCP estimated in chapter 3 are used. The simulation in the Soa lens using musrSim includes the decay loss. The decay loss in the RFQ and the diagnostic beam line is calculated as

$$\varepsilon_{\mathrm{decay}} = \exp\left(-\frac{t_{\mathrm{trans.}}}{\tau}\right), \tag{6.3}$$

where $t_{\mathrm{trans.}} = 523.8$ ns is the transition time through the RFQ and the diagnostic beam line and τ is the muon life time. The decay loss $\varepsilon_{\mathrm{decay}}$ is evaluated to be 79 %. Since the intensity of incident surface muons in the muon acceleration experiment was 2.5×10^6 μ^+/s at the Mu^- production target, the expected event rate of the Mu^- is $(6.8 \pm 1.2) \times 10^{-4}$ Mu^-/s as shown in table 6.5.

Table 6.5: Summary of expected TOF and event rate for the Mu^- in the muon acceleration simulation.

TOF [ns]	Expected event rate [/s]
813.1	$(6.8 \pm 1.2) \times 10^{-4}$

Table 6.6: List of the estimated beam losses for the muon acceleration simulation.

Source of the beam loss	Values
Target acceptance	2.4×10^{-1}
Cooling efficiency	$(1.1 \pm 0.2) \times 10^{-6}$
Mesh transmission efficiency	8.5×10^{-1}
Transport efficiency in the Soa lens	5.2×10^{-2}
Transport efficiency in the RFQ	5.5×10^{-2}
Decay loss in the RFQ and the diagnostic beam line	7.9×10^{-1}
Transport in the diagnostic beam line	8.9×10^{-1}
Detection efficiency of the MCP	6.0×10^{-1}
Total loss	$(2.7 \pm 0.5) \times 10^{-10}$

Chapter 7

Analysis of the muon acceleration experiment

The analysis of the accelerated Mu^-'s using the data set summarized in table 7.1 is described in this chapter. At first, the arrival time of the incident muon beam at the Al target is estimated with the same method described in chapter 4. Then, the TOF and the event rate of the accelerated Mu^- is evaluated with the the extended log-likelihood fitting. The number of the signal events evaluated with this fitting is corrected considering the selection efficiency of the pulse height cut. The measured event rate of the accelerated Mu^-'s is compared with the simulated one with the simulation in chapter 8.

Table 7.1: Data set of the muon acceleration experiment.

Polarity	RF power	Number of triggers	Data acquisition time [hours]	Number of the MCP hits after the signal processing
Positive	On	9.3×10^5	10.3	2041
Negative	On	3.9×10^6	43.4	3377
Negative	Off	4.1×10^5	4.5	286

7.1 Signal processing

The single-anode MCP was used for the muon acceleration experiment to avoid the ringing in the waveform. The waveform signal from the MCP was recorded with the FADC. The width of the sampling gate for the FADC was set to be 10 μs. Figure 7.1 shows the typical waveform of the single-anode MCP. A hit time and a pulse height were extracted from the waveform. The threshold to recognize as the signal information was 50 mV. The base line to calculate the pulse height was defined as the average of the ADC counts of 400 ns from the beginning of the gate. The data of the time region from 500 ns to 5000 ns were used, because the interested events are within this time region.

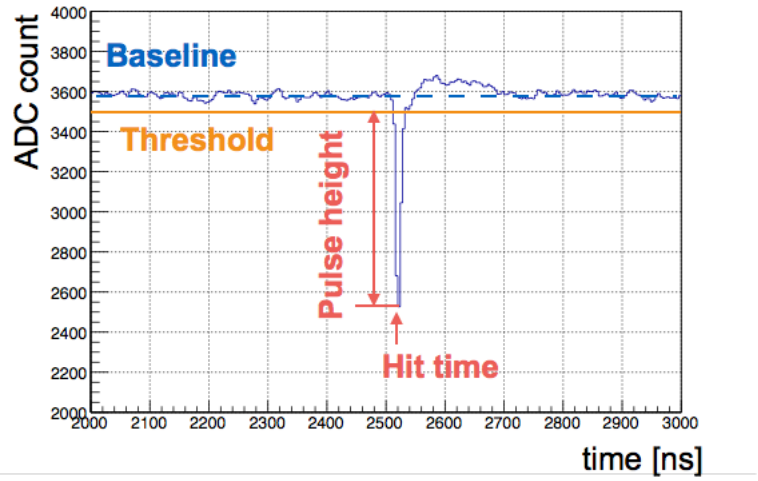

Figure 7.1: Waveform histogram of the single-anode MCP.

7.2 Event selection

7.2.1 Determination of the muon arrival time

The arrival time of the incident muon beam at the Al target was determined using the prompt positron signal in the MCP data taking account in the time difference between the arrival time of prompt positrons and the muon arrival time. This time difference was determined to be $\Delta t = 298.4 \pm 0.4$ ns in chapter 4. Figure 7.2 shows the time distribution of the MCP for the negative RF-on data. The fitting function was the Gaussian. The arrival time of prompt positrons was determined as

$$t_{\text{prompt}} = 970.8 \pm 2.8 \text{ ns}. \tag{7.1}$$

Therefore, the muon arrival time for the MCP data is

$$t_0 \equiv t_{\text{prompt}} - \Delta t = 1269.6 \pm 2.8 \text{ ns}, \tag{7.2}$$

The error is statistical only. The TOF was obtained by subtracting t_0 form the raw time data. Figures 7.3, 7.4 and 7.4 show and the scatter plots of the TOF versus the pulse height and the projected TOF distributions for each data.

The peak around 280 ns in the positive RF-on data in figure 7.3 corresponds to the μ^+'s which penetrate the Al target. The energy distribution of the μ^+'s which penetrate the Al target reaches more than the acceleration energy of the RFQ. The μ^+'s which has the same energy of the accelerated Mu^- can be transported to the MCP with the same BM current. The TOF of the penetrated μ^+ is shorter than that of the accelerated Mu^-, because the accelerated Mu^- spends time for the acceleration at the Soa lens. Since the distance between the Al target and the MCP along the beam axis is 3404 mm, when the β of the penetrated μ^+ is 0.041 (i.e. 89 keV), the TOF of the penetrated μ^+ is 280 ns. The peak of the accelerated Mu^--like events is also observed around 810 ns at the negative RF-on data in figure 7.4.

Figure 7.6 shows the TOF distributions of the negative RF-on and RF-off data with which the pulse height cut is applied. The peak in the TOF distribution for the RF-on data is consistent with the simulated TOF indicated as as the hatched histogram. On the other hand, no significant peak in the TOF distribution for the negative RF-off data is observed. This means that the peak in the RF-on data is the accelerated Mu^- signal.

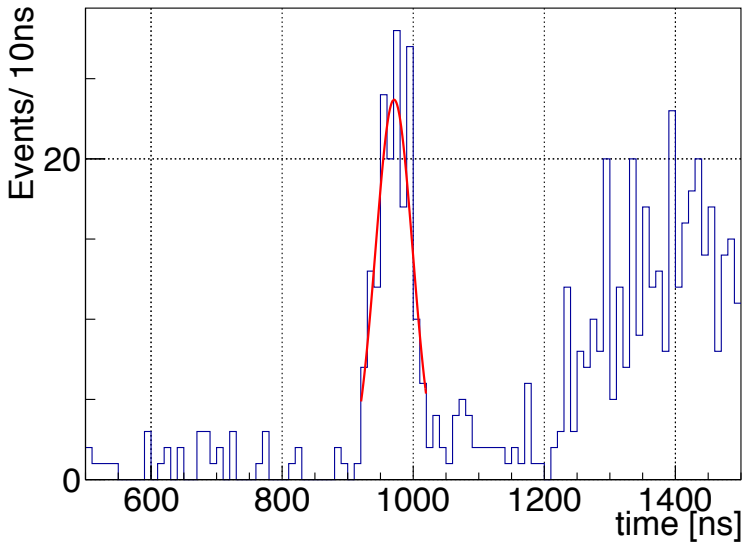

Figure 7.2: Time distribution of the MCP for the negative RF-on data. The fitted peak is the prompt positrons.

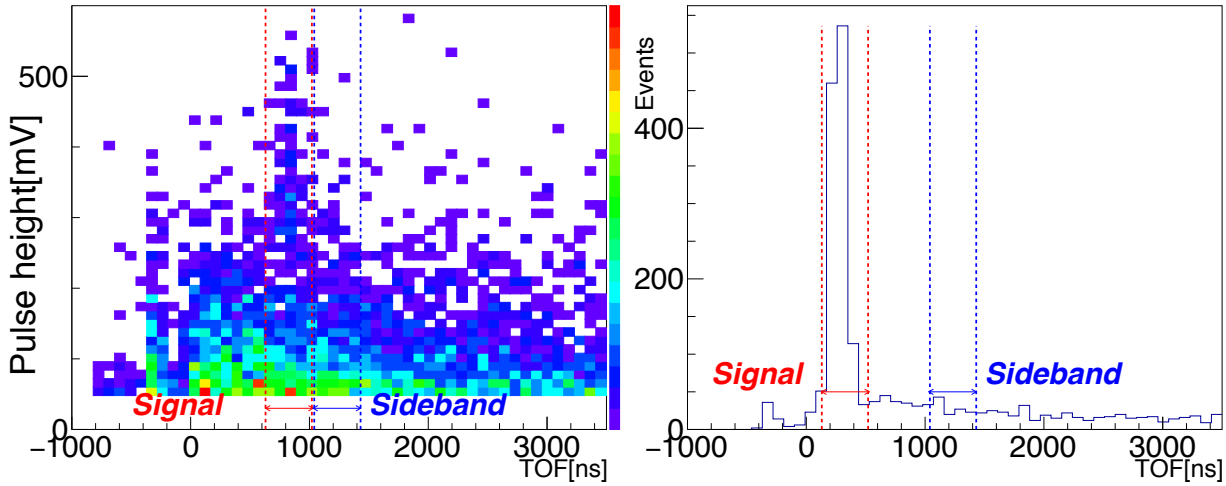

Figure 7.3: Scatter plots of the TOF versus the pulse height (left) and the TOF distribution (right) for the positive RF-on data after the time correction.

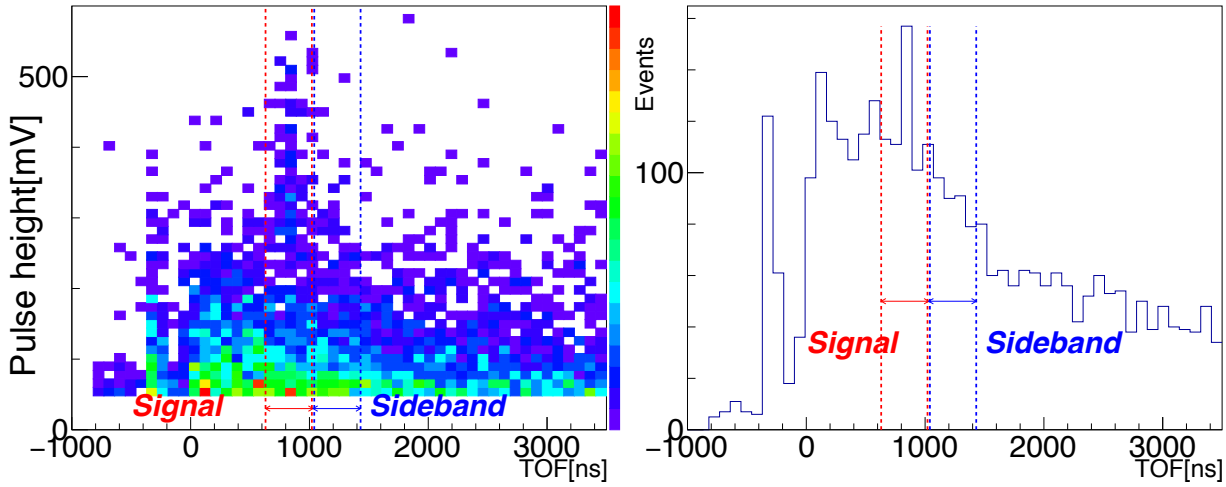

Figure 7.4: Scatter plots of the TOF versus the pulse height (left) and the TOF distribution (right) for the negative RF-on data after the time correction.

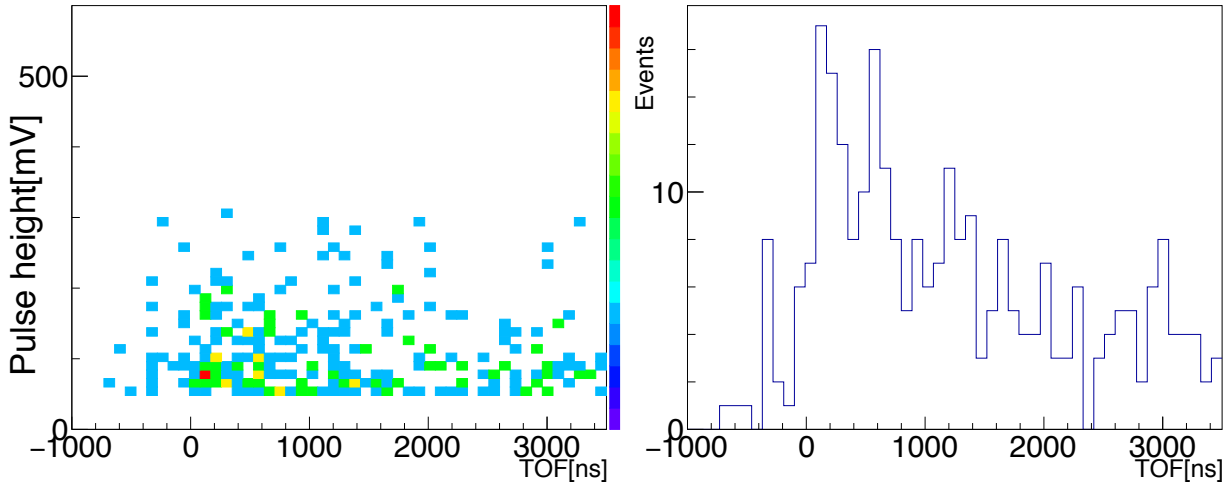

Figure 7.5: Scatter plots of the TOF versus the pulse height (left) and the TOF distribution (right) for the negative RF-off data after the time correction.

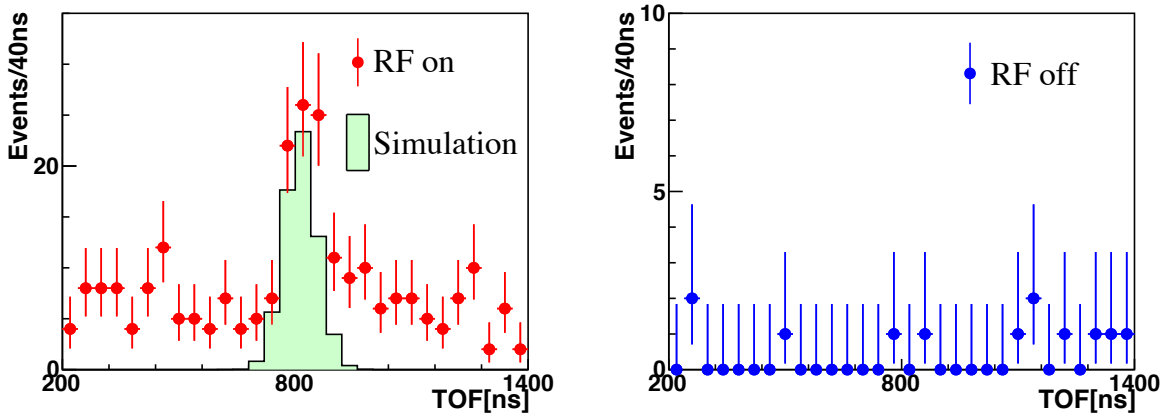

Figure 7.6: Comparison of the TOF distributions between the RF-on (left) and RF-off (right) data with the negative polarity. The threshold of the pulse height cut is 200 mV. The simulated histogram is also shown as the hatched histogram.

7.2.2 Background suppression

To eliminate the background from the decay positrons, the pulse height cut was applied. In order to determine the threshold and estimate the selection efficiency, the pulse height distribution of the μ^+ and Mu^- events were obtained by subtracting the pulse height distributions of the sideband regions from those of the signal regions. The signal regions are defined to select the penetrated μ^+ events in the positive RF-on data and the accelerated Mu^--like events in the negative RF-on data. They are shown in figure 7.3 and 7.4 as the red-dotted lines. The sideband regions are defined to select the positron-like events. They are shown in figure 7.3 and 7.4 as the blue-dotted lines.

Figure 7.7 shows the pulse height distributions in the signal region and sideband regions for the positive and negative RF-on data. The pulse height distributions of the sideband are normalized by the events in the pulse height region indicated with the green dotted-lines, in which almost all the events are decay positrons. Figure 7.8 shows pulse height distributions in the sideband regions every 200 ns for positive and negative RF-on data. No significant difference in these pulse height distribution is seen. Figure 7.9 shows subtracted pulse height distributions of the penetrated μ^+'s and the accelerated Mu^--like events. The pulse height distribution of the penetrated μ^+'s is scaled by the accelerated Mu^--like events.

The selection efficiency of the pulse height cut is evaluated using the pulse height distribution of the penetrated μ^+ events. Figure 7.10 shows the pulse height distribution of the penetrated μ^+ and the survival fraction as a function of the threshold value. The threshold is determined to be 200 mV. With this threshold, the survival fraction is 0.8244 ± 0.0005.

7.3 Evaluation of the TOF and the event rate

The TOF and event rate of the accelerated Mu^- are measured by fitting the negative RF-on data. The same extended log-likelihood method shown in chapter 4 is utilized. The fitting region is between 200 ns and 2700 ns. Errors of the fitting parameters are estimated for one standard deviation. Figure 7.11 shows the fitted TOF distribution for the negative RF-on data.

From this fitting, the TOF is estimated to be 827.8 ± 8.3 ns. The error of the TOF is calculated as $\Delta t_{\mathrm{TOF}} = \sqrt{(\Delta t_{\mathrm{TOF,fit}})^2 + (\Delta t_{t_0})^2}$, where Δt_{TOF} is the error of the TOF, $\Delta t_{\mathrm{TOF,fit}}$ is the statistical error estimated by the fitting and Δt_{t_0} is determined to be 3.0 ns in section 4.2.1. Therefore, Δt_{TOF} is 8.8 ns. The number of the signal events is evaluated to be 66.3 ± 10.4

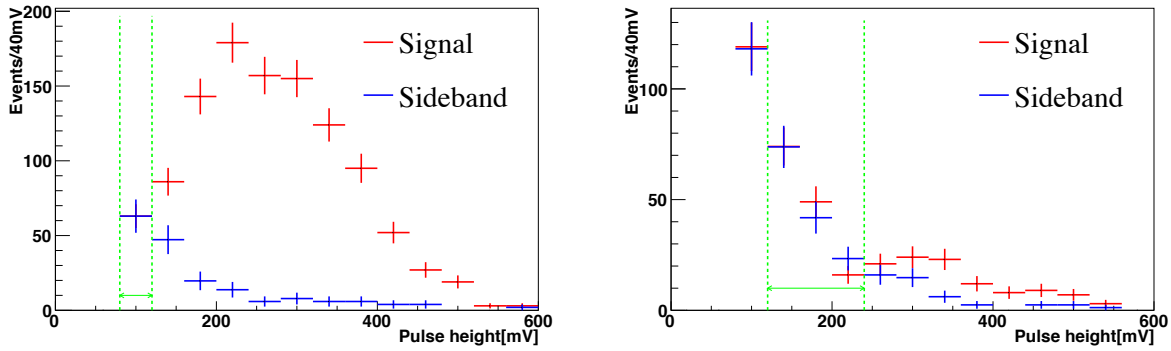

Figure 7.7: Pulse height distributions of the signal and sideband regions for the positive (left) and negative RF-on (right) data. Events in the region shown by the green dotted-line were used for the normalization of histograms.

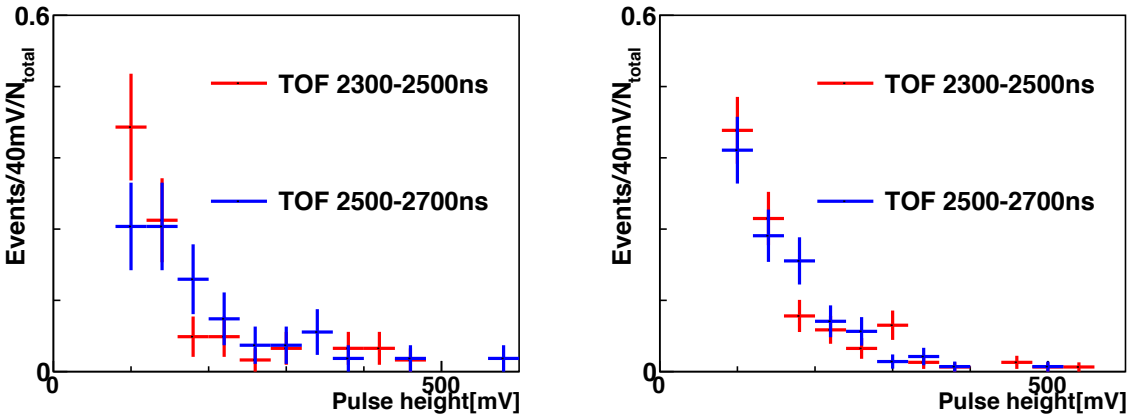

Figure 7.8: Pulse height distributions in the sideband regions every 200 ns for data of positive (right) and negative RF-on (left) extractions.

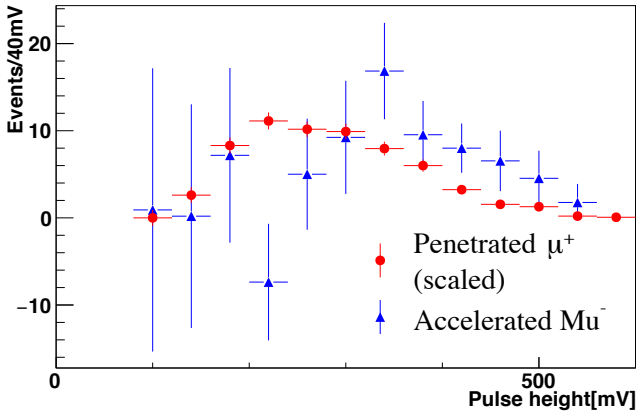

Figure 7.9: Comparison of pulse height distributions between the penetrated μ^+'s and the accelerated Mu^--like events.

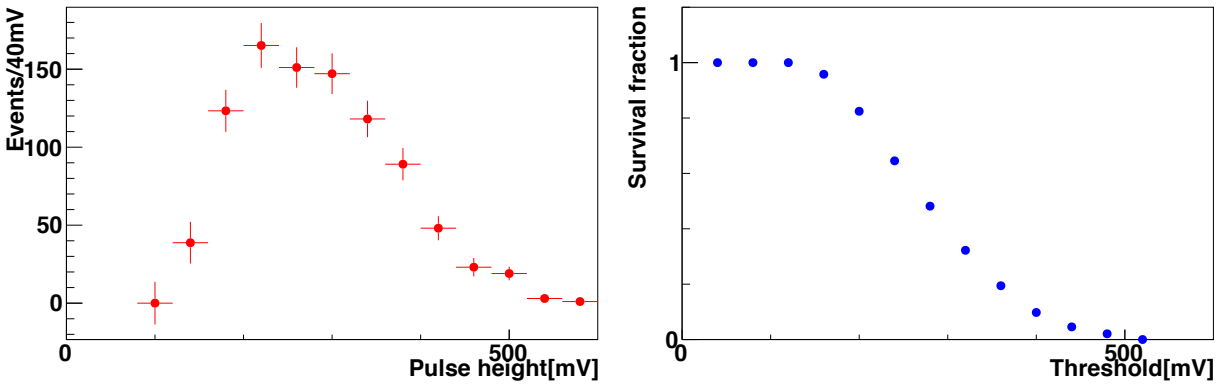

Figure 7.10: Pulse height distribution (left) and survival fraction of the pulse height cut (right) for the penetrated μ^+ data.

events with this fitting. This is corrected using of the selection efficiency obtained in the previous section to be 80.4 ± 12.6 events. The total number of triggers is 3.9×10^6 and the repetition rate is 25 Hz. Therefore, the measured event rate of the accelerated Mu^- is calculated to be $(5.1 \pm 0.8) \times 10^{-4}$ /s.

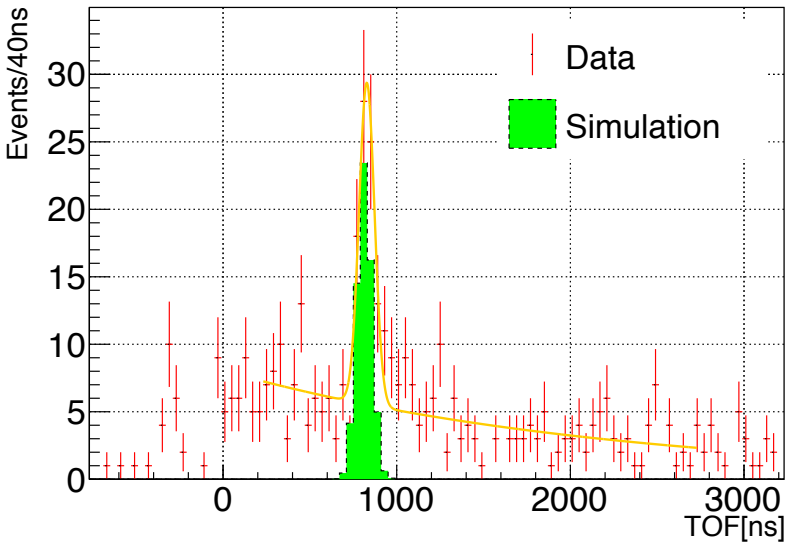

Figure 7.11: Fitted TOF distribution.

In summary, the measured TOF and event rate of the accelerated Mu^- are 827.8±8.8 ns and $(5.1 \pm 0.8) \times 10^{-4}$ /s, respectively. The measured TOF is consistent with that of the simulation, which was obtained in section 6.5.1 to be 813.1 ns.

Chapter 8

Discussion

8.1 Summary of the muon acceleration experiment

The world first muon RF acceleration was demonstrated using the Mu^- produced with the aluminum foil target and the RFQ. The measured TOF and event rate of the Mu^- accelerated with the RFQ were 827.8±8.8 ns and $(5.1 \pm 0.8) \times 10^{-4}$ /s, respectively. Since the simulated TOF of the Mu^- is 813.1 ns, the measured TOF of the Mu^- was consistent with the expectation. It is clear that the Mu^- accelerated with the RFQ was observed. Table 8.1 shows the summary of the event rate in the muon acceleration experiment. The measured event rate of the Mu^- is consistent with the expectation. It means that the beam intensity in the muon acceleration can be reproduced with this model of the simulation.

Table 8.1: Summary of the event rate of the Mu^- in the muon acceleration experiment.

Incident muon intensity [/s]	2.5×10^6
Total beam transport efficiency	$(2.7 \pm 0.5) \times 10^{-10}$
Expected event rate [/s]	$(6.8 \pm 1.2) \times 10^{-4}$
Measured event rate [/s]	$(5.1 \pm 0.8) \times 10^{-4}$

8.2 Improvement of the Mu^- event rate

While the demonstration of the muon acceleration experiment was successful, the measured event rate of the accelerated Mu^- was so small that it was hard to use it for the detailed tuning of the muon linac which is described in Appendix B. Therefore, the improvement of the event rate of the Mu^- beam is important until the implementation of the USM source. Following plans can be considered to improve the Mu^- rate.

- The yield of the Mu^- into the vacuum can be increased, when the target coated by the alkali metal like the cesium is used instead of the aluminum foil target. It is known that the target with the low work function has the large yield of the Mu^-. The conversion efficiency of the Mu^- using such target will be increased with an order or more [61].
- The effective area of the Mu^- production target can be increased using a large target and a large Soa lens to improve the event rate of the Mu^- beam. The target acceptance and transport efficiency in the Soa lens were 24 % and 5.2 %, respectively in this acceleration experiment. The total efficiency including the target acceptance and transport efficiency

in the Soa lens will be increased with a factor of two using the simulation, when the target radius is two times larger than the current radius.

- The momentum of the incident muon beam was set to 25.0 MeV/c in the Mu^- production experiment and the muon acceleration experiment. This momentum was determined by the thickness of the degrader in front of the Mu^- production target. The intensity of the surface muon beam in the D-line or H-line in the MLF [62] is maximized with the momentum of 27.4 MeV/c. When the degrader is optimized to use the surface muon beam with the maximum intensity, the event rate of the Mu^- will be increased by a factor of 1.7.

- The expected intensity of the surface muon beam in the Muon H-line which are being constructed in the MLF will be ten times higher than that in the D-line from the beam transport simulation and the measurement of the beam intensity of the surface muons in the D-line [9].

- The open aperture ratio of the MCP used in the Mu^- production experiment and the muon acceleration experiment is 60 %. Since the detection efficiency of the MCP is estimated as the open aperture ratio, the detection efficiency of the MCP will be increased with a factor of 1.6, when the MCP with a higher open aperture ratio. It will be able to be improved to be 100 %.

- The beam power of the primary proton beam will be improved from the current beam power of 319 kW to 1 MW for a few years. Then the intensity of the incident muon beam will be increased by a factor of three.

With improvements of above plans, the event rate with an $O(1)$ /s for the accelerated Mu^- will be expected in the muon acceleration experiment at the H-line for the muon linac as shown in table 8.2.

Table 8.2: Factors to improves the event rate of the Mu^- beam.

Improvement	Increase rate
New Mu^- target	10
Large target acceptance and Soa lens	2
Degrader optimization	1.7
Using the H-line	10
MCP with the high open aperture ratio	1.6
Proton beam of 1 MW	3
Total	1.6×10^3

8.3 Summary of the emittance and event rate

Table 8.3 shows the simulated beam emittances and event rates of Mu^-'s at the upstream side of the Mu^- production target, the entrance and the exit of the RFQ. The transverse normalized emittance is compressed with two orders of the magnitude and the event rate is reduced with six orders of the magnitude through the Mu^- production and the electrostatic acceleration. The transverse normalized emittance after the RFQ is additionally reduced, because the phase space is cut by the input acceptance of RFQ. The transmission of the RFQ will be improved, if the phase

space is more compressed using the USM instead of the Mu^-. Table 8.4 shows the simulated beam emittances and event rates of the USM at the upstream side of the USM production target, the entrance and the exit of the RFQ at the H-line, the USM and the RFQII which is described in Appendix B,. The much higher-intensity muon beam with the low emittance can be obtained with this condition to carried out the precision measurement of the muon dipole moments.

Table 8.3: Emittances and event rates, which are estimated with simulations. The ε_i is the normalized RMS emittance.

Parameters	Incident muons	RFQ-in	RFQ-out
${\varepsilon_x}^{a,b}$	2.1×10^2	2.2	7.5×10^{-1}
${\varepsilon_y}^{a,b}$	1.1×10^2	1.9	2.0×10^{-1}
${\varepsilon_z}^{a,c}$	–	–	8.6×10^{-2}
Event rate [d]	2.5×10^6	3.2×10^{-2}	1.4×10^{-3}

[a] RMS, normalized
[b] π mm mrad
[c] π MeV deg
[d] Assuming the proton beam of the 319 kW at the D-line.

Table 8.4: Emittances and event rates, which are estimated with simulations assuming the USM and H-line. The ε_i is the normalized RMS emittance.

Parameters	Incident muons	RFQ-in	RFQ-out
${\varepsilon_x}^{a,b}$	–	3.8×10^{-1}	3.0×10^{-1}
${\varepsilon_y}^{a,b}$	–	1.1×10^{-1}	1.7×10^{-1}
${\varepsilon_z}^{a,c}$	–	–	3.8×10^{-2}
Event rate [d]	3.2×10^8	4.7×10^5	3.8×10^5

[a] RMS, normalized
[b] π mm mrad
[c] π MeV deg
[d] Assuming the proton beam of the 1 MW at the H-line.

8.4 Significance and perspective of the demonstration of the muon RF acceleration

The measured event rate of the accelerated Mu^- was consistent with the expected event rate as shown in section 8.1. Since the prototype RFQ used in this muon acceleration experiment is the similar design to the RFQII and the common simulation (PARMTEQM) is used for both of the prototype RFQ and the RFQII, the ambiguity of the output event rate from the RFQII is same when the Mu^- beam is used in the H-line. As shown in section 8.2, the accelerated Mu^- beam of an $O(1)$ /s is expected if these improvements are made. Therefore, when the H-line has been constructed, the acceleration experiment using the RFQII and the Mu^- beam can be carried out immediately. As for the subsequent accelerator in the muon linac, the IH-DTL was already fabricated and is being tested [63]. It can be used for the muon acceleration after the RFQ. In conclusion, the precision measurement of the muon dipole moments in the J-PARC gets a boost from this success of the acceleration experiment.

In terms of the other applications of the low-emittance muon beam such as the muon collider, no demonstration of the muon RF acceleration was one of the restraints for the realization of the project. This result opens the door for the applications of the low-emittance muon beam and provides the new and strong tool to develop the new scientific fields.

Chapter 9

Conclusion

The muon RF acceleration was demonstrated for the first time with the Mu^- beam and the RFQ. Towards this muon RF acceleration experiment, the new measurement system was developed to measure the production yield of the Mu^- source. Then, the event rate of the Mu^- was measured with this measurement system. Finally, the accelerated Mu^- with the RFQ clearly was observed using this Mu^- source. The essential points of this success is the use of the TOF measurement, considering the feature of the pulsed muon beam at the J-PARC MLF. Thanks to the TOF measurement, the background contained in the Mu^- beam is significantly suppressed, and the accelerated Mu^- beam was clearly identified.

At first, the new measurement system was developed to estimate the production yield of the Mu^- using the Al target. The Mu^- extracted from the Al target with the electrostatic accelerator was transported to the MCP through the ED and the BM to reduce the backgrounds. The time difference between the collision time of the incident muon at the target and the detection time of the Mu^- at the MCP was defined as the TOF. Since the backgrounds were suppressed with the TOF measurement, the clear signal of the Mu^- was obtained with this measurement system. The measured event rate of the Mu^- was $(1.7 \pm 0.3) \times 10^{-3}$ /s. From these results, the well-defined Mu^- source was developed including the electrostatic accelerator towards the muon acceleration with the RFQ.

The demonstration of the muon RF acceleration was carried out using this developed Mu^- source. In this experiment, the Mu^- source including the electrostatic accelerator was connected to the RFQ. The accelerated Mu^- was identified with the TOF measurement as well as the momentum selection using the BM to suppress the backgrounds. The clear signal was observed with the TOF measurement, when the RF power of the RFQ was turned on. On the other hand, no significant signal was observed, when the RF power was turned off. The measured event rate of the accelerated Mu^- was $(5.1 \pm 0.8) \times 10^{-4}$ /s, while the expected event rate was $(6.8 \pm 1.2) \times 10^{-4}$ /s from the result of the Mu^- production experiment. Then, the measured event rate was consistent with the expectation. Therefore, we concluded the Mu^- was exactly accelerated with the RFQ. It is the first muon RF acceleration in the world.

This method of the TOF measurement also is used to identify the accelerated Mu^- in the future accelerator commissioning. By adding the several improvements, the event rate of the Mu^- beam will be increased in the commissioning of the muon linac for the J-PARC E34. The successful demonstration of the muon RF acceleration greatly advances the realization of the low-emittance muon beam and the precision measurement of the muon dipole moments. This result opens the door for the various interesting applications using the low-emittance muon beam to develop the new scientific fields.

Appendix A

Physics of muon dipole moments

A.1 Precision measurement of muon dipole moments

The low-emittance muon beam with the muon RF acceleration permits the precision measurement of the muon dipole moments to search for the BSM. The physics motivation for the measurement of the muon dipole moments is described in this chapter.

A.1.1 Muon

The muon is one of the charged leptons with a spin 1/2. The muon belongs to a second generation and its mass is 207 times heavier than the mass of the electron but 1/9 lighter than that of the proton. Table A.1 shows the mass and mean life time of the muon. Since the mean life time of the muon is relatively longer than those of other unstable particles, the muon permits the precision measurement to search the BSM of the particle physics for the higher energy scale more than 1 TeV.

A lot of muons are artificially produced from the accelerated proton beam via the pion decay using the high-energy accelerator. This accelerator facility is called as the meson factory. The materials and life science experimental facility (MLF) in the J-PARC is one of such meson factories. When the muon is produced with pion decay at rest, the produced muon is intrinsically polarized, because the pion decay violates the parity conservation. This is the remarkable nature of the muon and makes the muon the strong probe not only to search the new phenomenon in the particle physics but also for the material and life science with the μSR.

Table A.1: Mass and the mean life time of the muon [64] [65].

Mass [MeV/c^2]	105.658 371 5±0.000 003 5
Mean life time [s]	$(2.196\ 981\ 1 \pm 0.000\ 002\ 2) \times 10^{-6}$

A.1.2 Muon anomalous magnetic moment

Muons can couple to other particles via quantum loops. All interactions appear in the quantum loops. The Hamiltonian for the spin 1/2 particle in the external electric and magnetic fields is described as

$$H = -\overrightarrow{\mu} \cdot \overrightarrow{B} - \overrightarrow{d} \cdot \overrightarrow{E}, \tag{A.1}$$

where $\overrightarrow{B}$ and $\overrightarrow{E}$ are external magnetic and electric fields, respectively. The magnetic moment of the muon is described as

$$\overrightarrow{\mu} = g\left(\frac{e}{2m}\right)\overrightarrow{s}, \tag{A.2}$$

where $\overrightarrow{\mu}$ is the magnetic moment, g is the g factor, e is the elementary charge, m is the muon mass and $\overrightarrow{s}$ is the spin. Although this g factor of the muon is calculated with the Dirac equation and equal to 2, it is slightly different from 2 from contributions of the quantum loop effects. The anomalous magnetic moment of the muon $(g-2)_\mu$ is defined as

$$a_\mu \equiv \frac{g-2}{2}. \tag{A.3}$$

The a_μ contains the information of interactions between the muon and all the other particles via the quantum corrections. If the clear discrepancy between the measured a_μ and the prediction from the SM is observed, it implies the evidence of the BSM.

The prediction of a_μ is precisely calculated in the SM. This SM prediction a_μ (SM) is conveniently divided into three parts, that is

$$a_\mu(\mathrm{SM}) = a_\mu(\mathrm{QED}) + a_\mu(\mathrm{EW}) + a_\mu(\mathrm{Had}), \tag{A.4}$$

where the first term is the quantum-electrodynamics (QED) contribution, the second term is the electroweak contribution (EW) and the third term is the hadronic contribution. Figure A.1 shows the several major types of the interactions to the muon described with Feynman diagrams.

The QED contribution a_μ (QED) includes the contributions of the diagrams which consist of the photon and the charged leptons. This contribution has been calculated up to and including 5-loop terms [66] as

$$a_\mu(\mathrm{QED}) = (11\ 658\ 471.8951 \pm 0.0080) \times 10^{-10}, \tag{A.5}$$

where the uncertainty is dominated from the error in the input value of the fine structure constant α. This α is determined with the measurement of the h/m_{Rb} [67], where h/m_{Rb} is the ratio between the Planck constant and the mass of ^{87}Rb atom.

The EW contribution a_μ (EW) includes the contributions of the diagrams which consist of at least one virtual $\mathrm{W}^{\pm}$, Z or Higgs bosons. This term has been computed up to and including 2-loop term, and leading-log term of 3-loop contributions [68]. The evaluation including the recent update of the the Higgs boson mass [69], is described as

$$a_\mu(\mathrm{EW}) = (15.36 \pm 0.10) \times 10^{-10}, \tag{A.6}$$

where the error is derived from the 3-loop contribution and the hadronic uncertainties.

The hadronic contribution a_μ (Had) includes the contributions of the diagrams which contain the hadronic (quark and gluon) loop contributions. It gives the main theoretical uncertainties for the a_μ (SM). The hadronic contribution is divided into the five terms, that is

$$a_\mu(\mathrm{Had}) = a_\mu(\mathrm{Had,\ LO}) + a_\mu(\mathrm{Had,\ NLO}) + a_\mu(\mathrm{Had,\ NNLO}) + a_\mu(\mathrm{Had,\ LBL}) + a_\mu(\mathrm{Had,LBL\ NLO}). \tag{A.7}$$

The first three terms are the hadronic leading-order (LO), next-to-leading (NLO) and next-to-next-to-leading order (NNLO) terms, respectively. The last two terms are the hadronic light-by-light term and its higher order correction, respectively.

The first term, a_μ (Had, LO) has been calculated by many groups. Here, we refer to this a_μ (Had, LO) as

$$a_\mu(\mathrm{Had,\ LO}) = (694.9 \pm 4.3) \times 10^{-10}\ [14]. \tag{A.8}$$

The uncertainties in this term dominate over the other uncertainties in the SM prediction. This terms is described as an integral over the total cross section of the "$\mathrm{e^+e^-} \rightarrow$hadrons" reaction, σ_{had}, with a known weight factor, that is

$$a_\mu(\mathrm{Had,\ LO}) = \frac{m_\mu^2}{12\pi^3} \int_{m_\pi^2}^{\infty} \frac{ds}{s} \hat{K}(s) \sigma_{\mathrm{had}}^0(s), \tag{A.9}$$

where $\sigma^0_{\rm had}$ is the undressed total cross section of the "$e^+e^- \rightarrow$hadrons" reaction, in which the vacuum polarization corrections are removed, and $\hat{K}(s)$ is a monotonically increasing function of $O(1)$ with $\hat{K}(m_\pi^2) = 0.40$, $\hat{K}(4m_\pi^2) = 0.63$, $\hat{K}(s) \rightarrow 1$ and $s \rightarrow \infty$. Note that the lower limit of this integral should be $s = m_\pi^2$, not $s = 4m_\pi^2$, taking into account a small contribution from the $\pi^0\gamma$ channel. The contribution of this integrand in the lower-energy region is important, since the cross section in lower-energy region is enraged by the factor of $1/s$. The important energy region in the "$e^+e^- \rightarrow$hadrons" reaction, is 0.305 GeV $< \sqrt{s} <$ 1.8 GeV. The most significant contribution comes from $\pi^+\pi^-$ channel. Therefore, the improvement of the experimental data for the pion form factor is required to improve the a_μ(Had, LO). Ongoing e^+e^- experiments such as SND and CMD-3 at VEPP-2000 [70] and BES III at BEPC II [71] will give more precise data to improve the contribution a_μ(Had, LO).

The second and third terms in equation (A.7), a_μ(Had, NLO LO), a_μ(Had, NNLO, are computed as

$$a_\mu(\text{Had, NLO}) = (-9.8 \pm 0.1) \times 10^{-10} \text{ [14] and} \tag{A.10}$$

$$a_\mu(\text{Had, NNLO}) = (1.24 \pm 0.01) \times 10^{-10} \text{ [72].} \tag{A.11}$$

Since the contribution a_μ(Had, NLO) contains the same hadronic vacuum polarization diagrams as that in a_μ(Had, LO), there is an almost -100 % correlation between the values of a_μ(Had, LO) and a_μ(Had, NLO). The uncertainty in this contribution a_μ(Had, NLO)partially cancels that in a_μ(Had, LO) as shown in [73].

For last two terms in equation (A.7), since it is hard to precisely evaluate these hadronic light-by-light terms from the first principles with the current computational techniques of the QCD, the calculation relies on a model of hadrons in some measure. These contributions are evaluated as

$$a_\mu(\text{Had, LBL}) = (10.5 \pm 2.6) \times 10^{-10} \text{ [74] and} \tag{A.12}$$

$$a_\mu(\text{Had, LBL NLO}) = (0.3 \pm 0.2) \pm 10^{-10} \text{ [75].} \tag{A.13}$$

Although the uncertainties with the calculations of the LO hadronic and light-by-light contributions using the lattice QCD are not as competitive as those with the conventional methods, these uncertainties calculated with the lattice QCD may be improved in the near future [76].

Taking into account all the contributions, the a_μ in the SM prediction is evaluated from equation (A.4) as

$$a_\mu(\text{SM}) = (11\ 659\ 184.4 \pm 4.9) \times 10^{-10}. \tag{A.14}$$

The current experimental value of a_μ (exp) is given by the BNL E821 experiment as described in section A.2, that is,

$$a_\mu(\text{exp}) = (11\ 659\ 208.0 \pm 6.3) \times 10^{-10} \text{ [15].} \tag{A.15}$$

To summarize, the deviation δa_μ between the SM prediction a_μ (SM) and the experimental value a_μ (exp) is

$$\delta a_\mu = a_\mu(\text{exp}) - a_\mu(\text{SM}) = (24.6 \pm 8.0) \times 10^{-10} \quad (3.1\sigma). \tag{A.16}$$

Figure A.2 shows the comparison between the theoretical expectation and experimental value of the $(g-2)_\mu$. More than three standard deviations of δa_μ is seen and may imply the evidence of the BSM.

The contribution of a_μ from the BSM is considered. Assuming that the energy scale of the BSM is enough heavier than the mass of the muon, the contribution of the BSM for the $(g-2)_\mu$

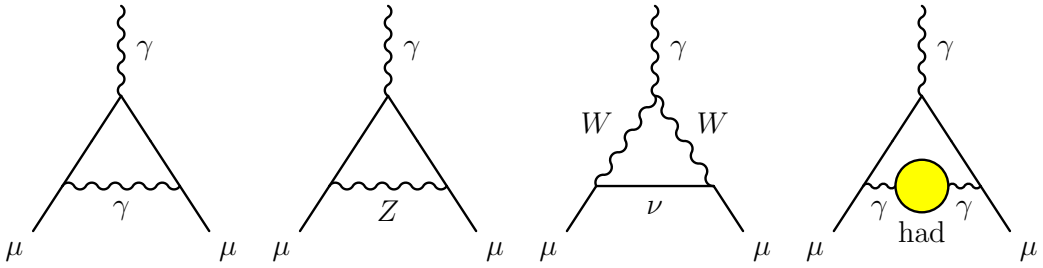

Figure A.1: Feynman diagrams of the interaction to the muon. From the left, the first order of the QED interaction, the lowest-order of the week interactions and the lowest-order of the hadronic interaction.This figure is taken from reference [77].

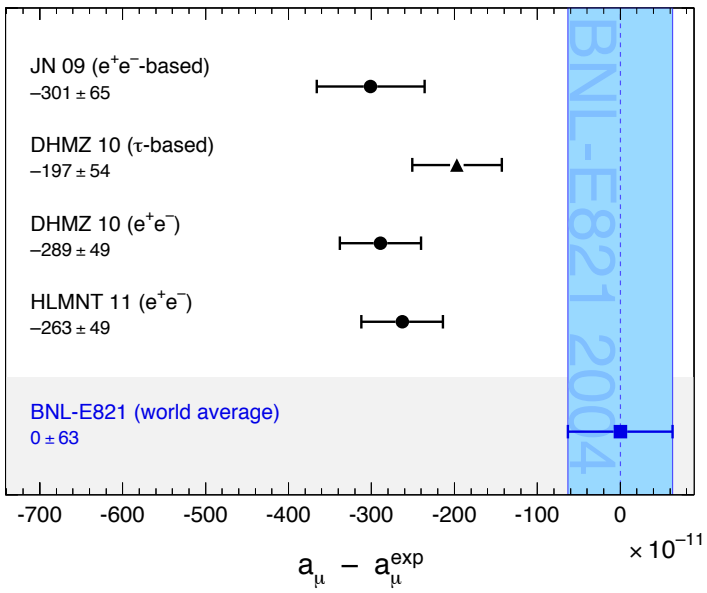

Figure A.2: Comparison between the theoretical expectation and experimental value of δa_μ. This figure is taken from reference [77].

is described in the low-energy effective Lagrangian [9]. Assuming the coupling between the muon and a new particle, this term in the effective Lagrangian is described as

$$L = \frac{e}{4m_\mu}\frac{m_\mu^2}{\Lambda_{\rm NP}^2}\overline{\psi_{\rm L}}\sigma_{\mu\nu}F^{\mu\nu}\psi_{\rm R} + \text{h. c.}, \tag{A.17}$$

where ψ is the field for the muon and $\Lambda_{\rm NP}$ is the scale of the new physics (NP). The effective interaction for this term is equivalent to the contribution $\delta V_{\rm NP}$ to the potential in the non-relativistic limit, which is described as

$$\delta V_{\rm NP} = -\overrightarrow{\mu}_{\rm NP}\cdot\overrightarrow{B}, \tag{A.18}$$

where $\overrightarrow{\mu}_{\rm NP}$ is the contribution for the NP to the magnetic moment of the muon. From equation (A.17) and (A.18), the $(g-2)_\mu$ contributes to the operator in equation (A.17). Therefore, the contribution of the $(g-2)_\mu$ for the NP, a_μ (NP) can be described as

$$a_\mu(\text{NP}) = \frac{m_\mu^2}{\Lambda_{\rm NP}^2}. \tag{A.19}$$

This scale of the $\Lambda_{\rm NP}$ is evaluated from equation (A.16) and (A.19) to be

$$\Lambda_{\rm NP} = 1.8 \sim 2.6 \text{ TeV}. \tag{A.20}$$

Although many BSM models to explain the contribution to a_μ are considered, the most typical and interesting model is the supersymmetric (SUSY) models. The magnitude of the contribution to a_μ is roughly evaluated based the minimal SUSY SM (MSSM). The leading SUSY contribution to a_μ is derived from the one-loop chargino-sneutrino and the neutralino-smuon diagrams. Assuming that all the SUSY particles have the typical mass $\tilde{m}$, the one-loop SUSY contribution to a_μ (SUSY) is described as [78]

$$a_\mu(\text{SUSY}) \simeq (\text{sgn }\mu)\times 130\times 10^{-11}\left(\frac{100\text{ GeV}}{\tilde{m}}\right)^2\tan\beta, \tag{A.21}$$

where sgn μ is the sign of the parameter in the SUSY model and $\tan\beta$ is the ratio of the vacuum expectation values of the two Higgs fields in the MSSM. Assuming $\tilde{m} = O(300)$ GeV, $\tan\beta = O(10)$ and sgn $\mu = +1$, the deviation of a_μ in equation (A.16) is explained with this magnitude of a_μ (SUSY). The improvement of the precision for the a_μ is quite important to search the BSM.

A.1.3 Muon electric dipole moment (EDM)

The muon electric dipole moment (EDM) is described as

$$\overrightarrow{d} = \eta\left(\frac{e}{2mc}\right)\overrightarrow{s}, \tag{A.22}$$

where η is the dimensionless constant, which is analogous to g in equation (A.2). Table A.2 shows the transformation properties of the magnetic and electric fields and the dipole moments under the party (P), charge (C) and time (T) reversal symmetries. The first term in equation (A.1), that is $\overrightarrow{\mu}\cdot\overrightarrow{B}$ is even under P, C and T reversal symmetries. However, the second term in equation (A.1), that is $\overrightarrow{d}\cdot\overrightarrow{E}$ is odd under both P and T reversal symmetries. Therefore, the EDM is the quantity which violate the P and T reversal symmetries under the CPT theorem. It means that the EDM violates the CP reversal symmetry.

Table A.2: Transformation properties of the magnetic and electric fields and dipole moments [79].

	$\overrightarrow{E}$	$\overrightarrow{B}$	μ or d
P	−	+	+
C	−	−	−
T	+	−	−

A large CP violation is predicted in the universe from the observation of the astrophysics [80]. Although the Kobayashi-Maskawa (KM) phase [81] describes the known CP violation with the Kaon and B meson, it is inadequate to explain the baryon asymmetry of the universe. As another candidate of the source of the CP violation, the searches for the permanent EDM's for the proton, neutron, ^{199}Hg and electron are reported [82] [83] [84]. The magnitude of the four-loop contribution to the electron EDM d_e(SM) is evaluated using the KM model to be

$$d_e(\mathrm{SM}) \approx 8 \times 10^{-41}\ e \cdot \mathrm{cm}\ [85]. \tag{A.23}$$

The SM prediction for the muon EDM d_μ(SM) is evaluated using this electron EDM to be

$$d_\mu(\mathrm{SM}) \approx \frac{m_\mu}{m_e} d_e(\mathrm{SM}) \approx 2 \times 10^{-38}\ e \cdot \mathrm{cm}. \tag{A.24}$$

On the other hand, the latest experimental value of the muon EDM d_μ(exp) is

$$d_\mu(\mathrm{exp}) = (-0.1 \pm 0.9) \times 10^{-19} e \cdot \mathrm{cm}\ [18]. \tag{A.25}$$

Since the SM prediction for the muon EDM d_μ(SM) is much smaller than the aimed sensitivity of the J-PARC E34 experiment, that is an order of 10^{-21} e·cm, the discovery of the finite EDM becomes the evidence of the BSM.

As shown in equation (A.17), the effect of the BSM for the muon EDM is also described with the effective Lagransian, when the energy scale of the BSM is enough heavier than the mass of the muon. After the integrating out the heavy BSM fields, the term of the BSM for the muon EDM in the effective Lagrangian is described as

$$L = -\frac{i}{2} d_\mu^{\mathrm{NP}} \overline{\psi} \sigma_{\mu\nu} \gamma_5 F^{\mu\nu} \psi, \tag{A.26}$$

where ψ is the field for the muon and the coefficient d_μ^{NP} is the BSM contribution to the muon EDM. This operator reduces to the correction δV_{NP} to the potential derived from the NP in the non-relativistic limit. The correction δV_{NP} is described as

$$\delta V_{\mathrm{NP}} = -d_\mu^{\mathrm{NP}} \overrightarrow{\sigma} \cdot \overrightarrow{E}, \tag{A.27}$$

where $\overrightarrow{\sigma}$ is the vector of Pauli matrices for the spin $\overrightarrow{s}$ of the muon, that is $\overrightarrow{s} = \frac{1}{2}\overrightarrow{\sigma}$. Taking into account the similarity relation between equation (A.17) and (A.26), the magnitude of d_μ^{NP} is evaluated as the naive estimation. To compare the coefficients in equation (A.17) and (A.26), the relation between the d_μ^{NP} and a_μ (NP) is described as

$$\left| -\frac{i}{2} d_\mu^{\mathrm{NP}} \right| \simeq \left| \frac{e}{4m_\mu} a_\mu(\mathrm{NP}) \right|. \tag{A.28}$$

Assuming the deviation of δa_μ in equation (A.16) is derived from the NP, if the value of a_μ (NP) is substituted into equation (A.28), the magnitude of the muon EDM for the NP is evaluated as

$$\left| d_\mu^{\mathrm{NP}} \right| \approx 2.5 \times 10^{-22}\ e \cdot \mathrm{cm}, \tag{A.29}$$

when the a_μ (NP) is assumed to be 25×10^{-10} [9].

A.2 BNL E821 experiment

The most precise experimental value of the $(g-2)_\mu$ was measured by the BNL E821 experiment. The brief of this experiment is explained in this section.

A.2.1 Principle of the experiment

The angular frequency of the muon spin precession in the external electric and magnetic fields is described as

$$\begin{aligned}\overrightarrow{\omega} &= \overrightarrow{\omega}_a + \overrightarrow{\omega}_\eta \\ &= -\frac{e}{m}\left[a_\mu \overrightarrow{B} - \left(a_\mu - \frac{1}{\gamma^2-1}\right)\frac{\overrightarrow{\beta}\times\overrightarrow{E}}{c} + \frac{\eta}{2}\left(\overrightarrow{\beta}\times\overrightarrow{B} + \frac{\overrightarrow{E}}{c}\right)\right],\end{aligned} \tag{A.30}$$

where $\overrightarrow{\omega}_a$ is the contribution of the spin precession for the a_μ and $\overrightarrow{\omega}_\eta$ is that for the EDM, e is the elementary charge, m is the muon mass, $\overrightarrow{B}$ and $\overrightarrow{E}$ are the external magnetic and electric fields in the storage ring, β and γ are relativistic β and γ, c is the speed of light. When the EDM contribution is enough small compared with the uncertainty of the a_μ, equation (A.30) is described as

$$\overrightarrow{\omega} = -\frac{e}{m}\left[a_\mu \overrightarrow{B} - \left(a_\mu - \frac{1}{\gamma^2-1}\right)\frac{\overrightarrow{\beta}\times\overrightarrow{E}}{c}\right] \tag{A.31}$$

If the momentum of the muon is $p_{\mathrm{magic}} \approx 3.094$ GeV/c, that is $\gamma = 29.3$, the coefficient of the $\overrightarrow{\beta}\times\overrightarrow{E}$ term vanishes. Then, equation (A.31) is simplified as

$$\overrightarrow{\omega} = -\frac{e}{m}a_\mu \overrightarrow{B}. \tag{A.32}$$

The a_μ is detemermined from the measurement of the spin precession of the muon and the measurement of the magnetic field in the storage ring as the naive description.

A.2.2 Experimental setup

The experimental setup and procedure are described briefly. Figure A.3 shows the overview of the beam lines. The bunched proton beam with the momentum of 24 GeV/c from the alternating gradient synchrotron (AGS) went into the nickel target and produced the pions. The number of the incident protons and the fraction of pions per proton captured with the subsequent beam line channel were 7×10^{12} protons per bunch and 10^{-5}, respectively. The bunch per cycle and the cycle repetition rate were 6–12 and 0.37 Hz, respectively. The pions were collected from the primary nickel target and transferred into a secondary pion-muon-decay channel. The pions decayed into the muons in the decay channel. The length of this decay channel is 80 m. K1-K2 and K3-K4 slits installed in the beam line as shown in figure A.3 were used to select the momentum of the beam, which was set to the magic momentum of 3.094 GeV/c. The beam line was adjusted to maximize the muon flux and minimize a pion contamination.

The longitudinally polarized muons were injected into the storage ring through the injector, which permits the muons to pass largely undeflected into the storage ring. The storage ring was made of a superconducting magnet. The radius in the central orbit was 7.1 m and the current of 5.2×10^3 A was applied. The magnet opened on the inside to permit the decay electrons to curl inward to the detectors. The magnetic field was designed to be vertical and uniform at a central value of 1.45 T. Since the net spin precession depends on the integrated field that the muon feels along its trajectory. The precision of the azimuthally averaged magnetic field in the storage volume had a uniformity of about 1 ppm after shimming. Electric quadrupoles to store

the muons in the storage ring were installed in the vacuum chamber. The muon life time in the storage ring is 64.4 μs. Twenty-four electromagnetic calorimeters were installed symmetrically around the inside of the storage ring to measure the arrival time and the energy of the decay electron.

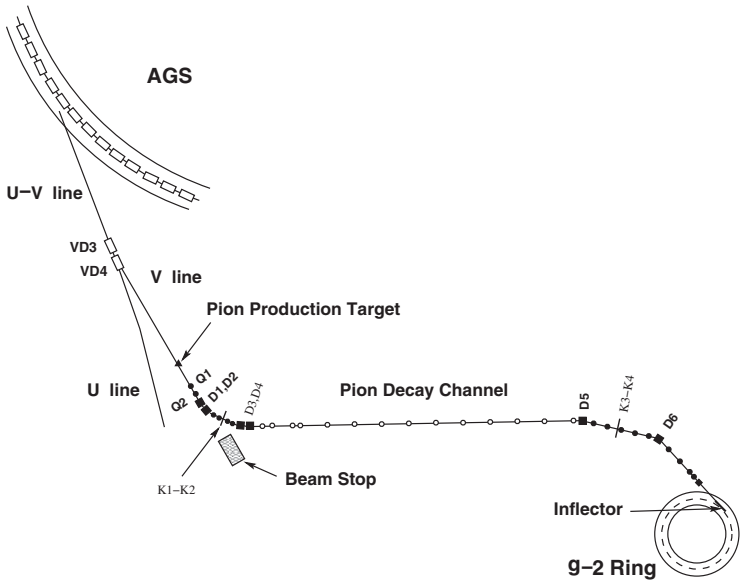

Figure A.3: Schematic drawing of the proton/pion/muon transport beam line in the BNL E821 experiment. This figure is taken from reference [15].

A.2.3 Result of the BNL E821 experiment

Since the muon decay is the weak interaction, the parity is violated. The muon spin direction is correlated with the probability of the emission of the decay electron. Using this correlation, the spin precession of the muon is described as the a function of the time by measuring the decay electron. The distribution of the integrated number of the measured decay electron is described as

$$N(t) = N_0 e^{-\frac{t}{\gamma\tau}}[1 - A\cos(\omega_a t + \phi)], \tag{A.33}$$

where N_0 is the initial number of decay positrons, τ is the muon mean lifetime, A is amplitude of the oscillation, and ϕ is the initial phase. The parameters, N_0, A and ϕ depend on the energy threshold, which was determined to the figure-of-merit.

The measured a_μ was determined by dividing ω_a by $\tilde{\omega_p}$, because the magnetic field measured using the NMR probe is proportional to the free-proton precession frequency ω_p. The ω_a was determined from the measurement of the decay electron. The $\tilde{\omega_p}$ is a measure of the average magnetic field which the muon saw. The a_μ is described as

$$a_\mu = \frac{\omega_a}{\omega_L - \omega_a} = \frac{(\frac{\omega_a}{\tilde{\omega_p}})}{(\frac{\omega_L}{\tilde{\omega_p}}) - (\frac{\omega_a}{\tilde{\omega_p}})} = \frac{R}{\lambda - R}, \tag{A.34}$$

where ω_L is the Larmor precession frequency of the muon. The ratio R is determined with this $(g-2)_\mu$ measurement and the magnetic moment ratio between the muon and the proton λ is determined with the muonium hyperfine level structure measurement [86] [87], that is

$$\lambda = \frac{\omega_L}{\omega_p} = 3.183\ 345\ 39 \pm 0.000\ 000\ 10. \tag{A.35}$$

In conclusion, the BNL E821 experiment gave the most precise value of a_μ and the upper limit of the muon EDM, those are

$$a_\mu(\text{exp}) = (11\ 659\ 208.0 \pm 6.3) \times 10^{-10}\ (0.54\ \text{ppm}) \text{ and} \tag{A.36}$$

$$|d_\mu| < 1.8 \times 10^{-19}\ \text{e} \cdot \text{cm}\ (95\%\ \text{C.L.}), \tag{A.37}$$

respectively.

As shown in equation (A.16), more than three standard deviation is seen from the result of the BNL E821 experiment. This is very interesting, because this discrepancy amy imply the BSM. Although the statistical uncertainty is dominant for the experimental value of the a_μ, the systematic uncertainties are also treated very carefully. The clear solution to confirm the discrepancy of the $(g-2)_\mu$ is to perform the independent measurement of the $(g-2)_\mu$. The new precision measurement containing different systematic uncertainties from the BNL E821 experiment will play the important role to search the BSM.

Appendix B

Muon g-2/EDM experiment at J-PARC

B.1 Principle of the experiment

The J-PARC muon g-2/EDM (J-PARC E34) experiment aims to measure the muon $(g-2)_\mu$ and EDM precisely with the novel techniques. The goals of sensitivities are 0.46 ppm for the $(g-2)_\mu$ and 1.5×10^{-21} $e\cdot$ cm for the EDM, respectively. Figure B.1 shows the overview of the J-PARC E34 experiment. The brief of the J-PARC E34 experiment is described in this chapter.

In the J-PARC E34 experiment, the general equation of the spin precession for the muon in the storage ring is simplified with another approach compared with the BNL E821 experiment. When the muon feels no static electric field in the storage ring, the second term of equation (A.30) is zero and third term can be simplified. The simplified equation of the spin precession under the no static electric field is described as

$$\overrightarrow{\omega} = -\frac{e}{m}\left[a_\mu \overrightarrow{B} + \frac{\eta}{2}\left(\overrightarrow{\beta} \times \overrightarrow{B}\right)\right]. \tag{B.1}$$

Figure B.2 shows the schematic of the muon spin and momentum directions in the horizontal plane. The first and second terms in equation (B.1) describe the contributions of the spin precessions with the $(g-2)_\mu$ and the EDM, respectively. Therefore, the horizontal and vertical components of the spin precessions give the $(g-2)_\mu$ and EDM contributions, with respect to the plain of the rotation for the muon in the storage ring. The $(g-2)_\mu$ and the EDM can be measured with these two components of the spin precessions at the same time. This approach is accomplished using the sharpen muon beam without the electric focusing, that is the muon beam with the low transverse emittance. Such muon beam is called as an ultra-cold muon (UCM) beam and plays an important role in the J-PARC E34 experiment. The UCM is produced from the conventional muon beam through the cooling process using the Mu production and the laser resonant ionization and the muon acceleration using the muon linac. The requirement of the UCM in the J-PARC E34 experiment is $\Delta p_T/p < 10^{-5}$.

B.2 Muon beam

The J-PARC consists of the three accelerators; H^- linear accelerator (LI), 3 GeV proton rapid cycle synchrotron (RCS) and 30 GeV synchrotron. First, the H^- is accelerated with the LI to 400 MeV and transported to the RCS. The H^- is converted to the H^+ (proton) with the stripping foil at the injection to the RCS. The proton is accelerated with the RCS to 3 GeV are transported to the MLF. Figure B.3 shows the delivery of the 3 GeV proton beam from the RCS to the MLF. A muon production target is made of the carbon and installed on the 3 GeV proton

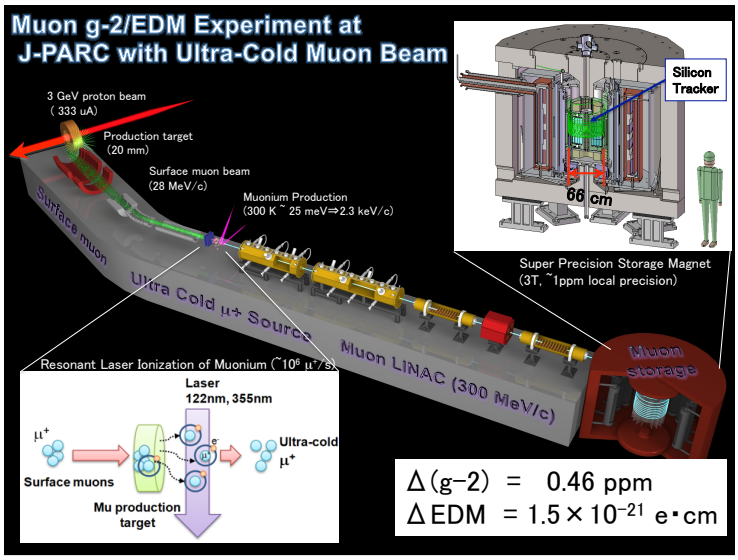

Figure B.1: Overview of the J-PARC E34 experiment. This figure is taken from reference [9].

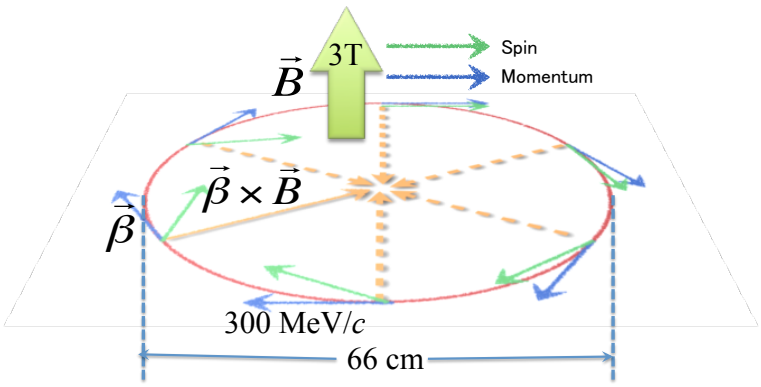

Figure B.2: Schematic of the spin and momentum directions of the muon in the horizontal plain.

beam line in the MLF. About 5 % of the total energy for the proton beam is consumed on the muon production target, when the 3 GeV proton beam penetrates through the muon production target.

The reaction to produce a charged pion in the muon production target is described as

$$p + N \to \pi^{\pm} + N. \tag{B.2}$$

The charged pion decays and the muon is produced, which are described as

$$\pi^{+} \to \mu^{+} + \nu_{\mu} \text{ and} \tag{B.3}$$
$$\pi^{-} \to \mu^{-} + \bar{\nu}_{\mu}. \tag{B.4}$$

The muon is produced from the pion decay in flight or at rest at the muon production target. The former and later are called as "decay muon" and "surface muon", respectively.

The surface muons are transported with the secondary muon beam line to the experimental area. Four muon beam lines will operates in the MLF muon facility; D-line, U-line, S-line and H-line [28]. Figure B.4 shows the schematic drawing of the muon beam lines in the MLF. The D-line is used in this thesis. The H-line is being constructed and the J-PARC E34 experiment will be carried out in this beam line. Other beam lines which are the U-line and the S-line are utilized for the studies of the material and life science with the μSR and the muonic X-ray.

The H-line is designed to obtain the high muon flux using a muon capture solenoid with a large aperture, a wide-gap bending magnet and a pair of two solenoid magnets with oppositely directed fields. Table B.1 shows typical muon beam parameters evaluated with the simulation. The expected muon beam intensity achieves 1.6×10^{8} μ^{+}/s, when the proton beam power is 1 MW.

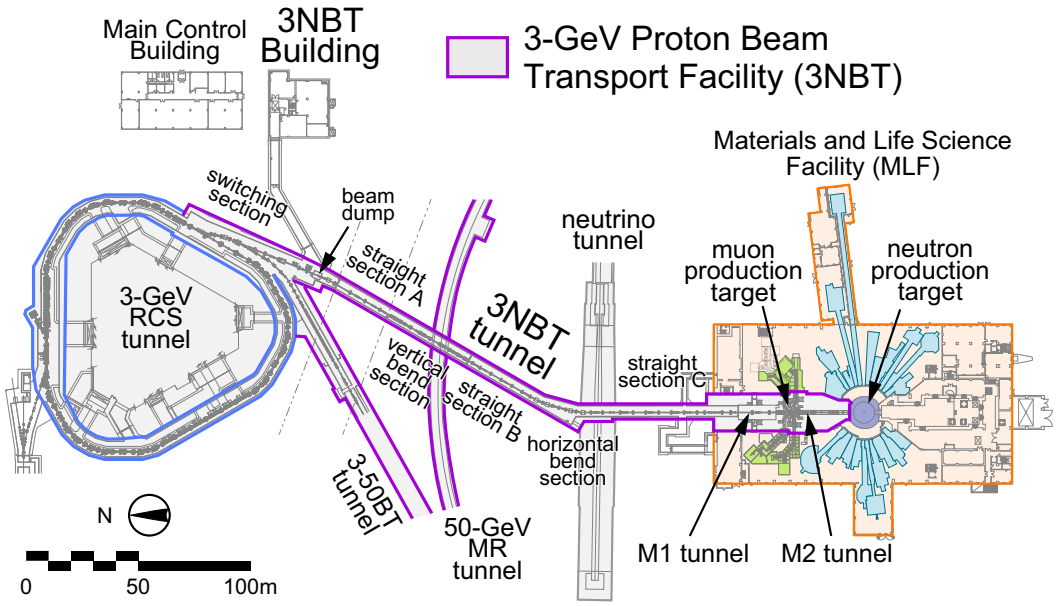

Figure B.3: Delivery of the 3 GeV proton beam from the RCS to the MLF. This figure is taken from reference [28].

B.3 Ultra-slow muon source

The conventional surface muon beam should be cooled to obtain the UCM beam. The ultra-slow muon (USM) production using a Mu production and the laser-ionization is described. Figure

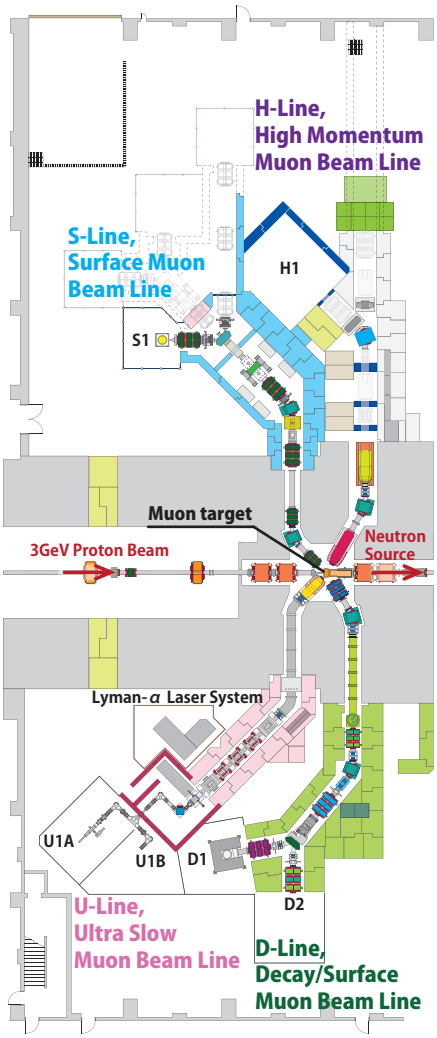

Figure B.4: Schematic drawing of the muon beam lines in MLF

Table B.1: Typical beam parameters of the H-line at the Mu production target [9]. The estimation of the beam intensity assumes the 1MW proton beam power.

Momentum [MeV/c]	27.3
Momentum bite [%]	5 (rms)
X [mm]	31.4 (rms)
Y [mm]	14.4 (rms)
Intensity [μ^+/s]	1.6×10^8

B.5 shows the schematic of the USM production. The incident surface muons are stopped at the Mu production target as shown in figure B.6 and the Mu's are produced [88]. This Mu target is the silica aerogel with the hole structure by the laser ablation. Much Mu emission into the vacuum is observed from this laser-ablated aerogel compared with the plane silica aerogel. The produced Mu's are evaporated to the downstream vacuum region. The Mu emission is simulated with the diffusion model based on the data [9].

Then, the Mu's in the vacuum are photo-ionized with two laser lights. One at the wavelength of the Mu Lyman-α (122 nm) photo-excites Mu from the ground to the 2P state, and then the other at the wavelength of 366 nm (or shorter) ionizes the excited Mu. This ionized μ^+ is called as the USM at the thermal energy ($E_k \sim 25$ meV). The USM's are extracted with the electrostatic accelerator installed in the USM production chamber and transported to the entrance of the RFQ.

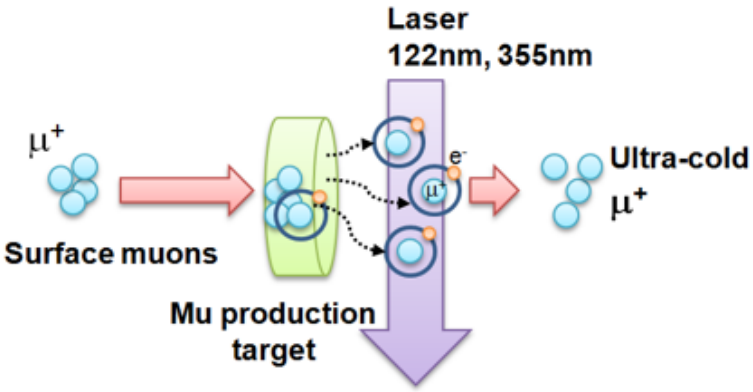

Figure B.5: Schematic of the muon cooling with the Mu production and the laser-ionization.

B.4 Muon linac

Extracted USM's are accelerated with the muon linac to 212 MeV. Figure B.7 shows the schematic of the muon linac. The detailed configuration of the muon linac is described in this section. The final kinetic energy comes from the requirement of the muon storage without the focusing. The ratio of the transverse component of the momentum to the longitudinal component of the momentum is less than 10^{-5} at the end of acceleration. In addition, since the muon decays with a mean life time of about 2.2 μs, it should be accelerated rapidly. To achieve the requirement and the effective acceleration, the muon linac are separated to four sections; the bunching and acceleration, the low β, the middle β, and the high β sections, where β is the relativistic velocity. The RF frequencies of the former two sections are 324 MHz and those

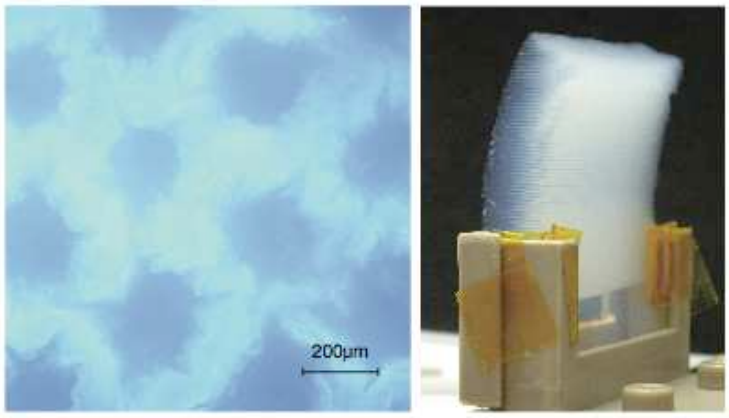

Figure B.6: Silica aerogel target as the Mu production target. This figure is taken from reference [88].

of the latter two sections are 1296 MHz, respectively. The proper structure for the effective acceleration should be selected in each section, because the β of the muon is rapidly increased.

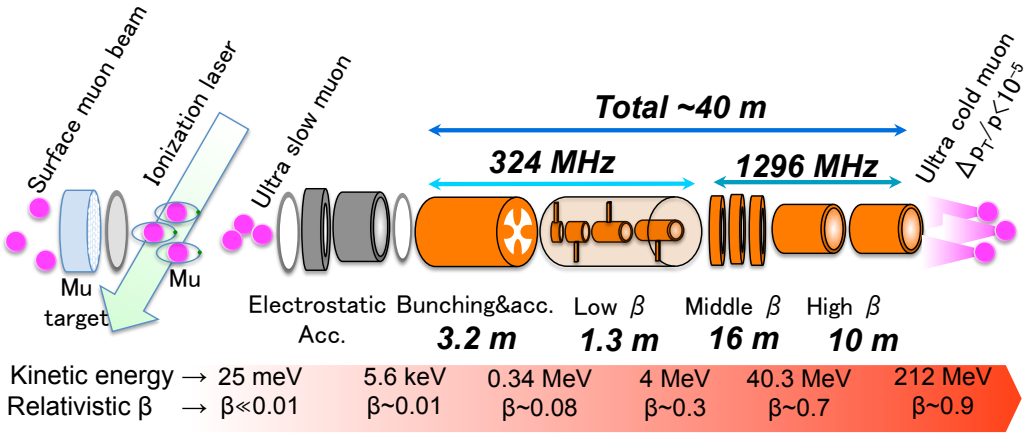

Figure B.7: Overview of the muon linac.

B.4.1 Electrostatic accelerator

The USM's are extracted from the Mu production target and transported to the entrance of the RFQ, using an electrostatic accelerator called as the Soa lens [29] [30] [31]. The Soa lens is described in chapter 2. Figures B.8 and B.9 show the schematic of the particle tracking simulation using GEANT4 for the Soa lens and the simulated phase-space distributions of the USM at the entrance of the RFQ, respectively. The transverse phase space of the extracted USM's is such enough to inject them into the input acceptance of the RFQ.

B.4.2 Bunching and acceleration

The RFQ is used for the bunching and the initial RF acceleration in the muon linac. The RFQ has four electrodes of an RF quadrupole with a modulation and can accelerate the beam with the longitudinal RF electric field and get the transverse focusing force. Figure B.10 shows the movement of the muons in the RFQ. In figure B.10, charged particles are moving from (1) to (4) in sequence.

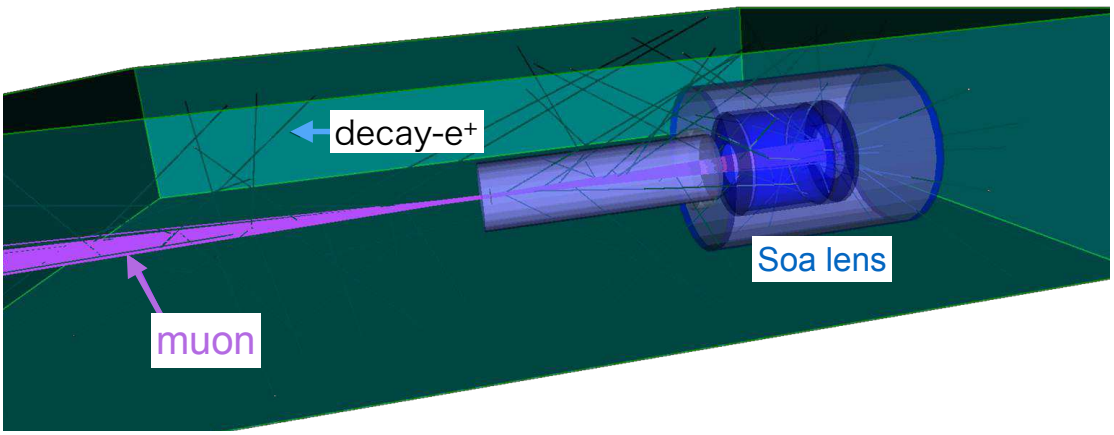

Figure B.8: Schematic of the particle tracking simulation using GEANT4 for the Soa lens. This figure is taken from reference [9].

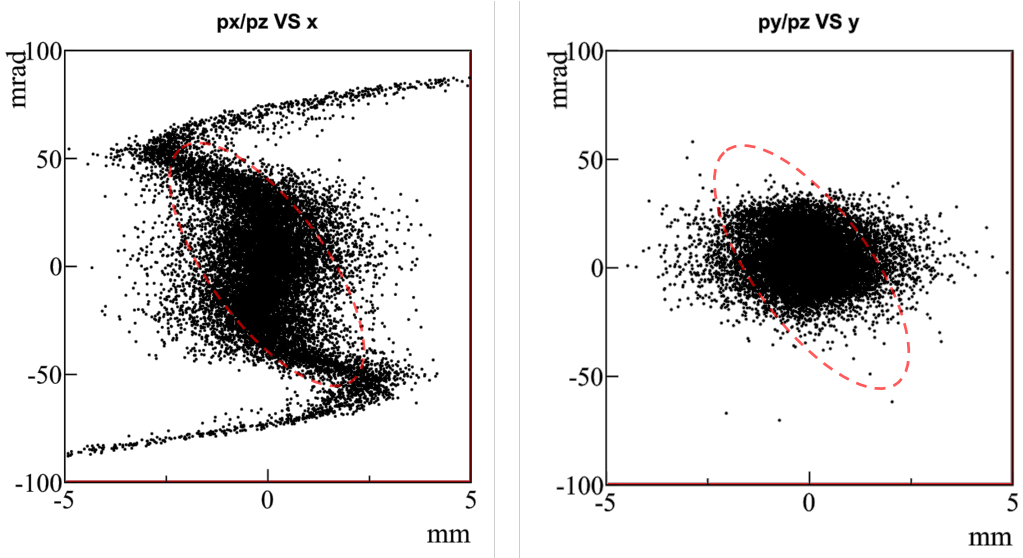

Figure B.9: Simulated phase-space distributions of the USM at the entrance of the muon linac. Red dotted line is the design input acceptance of the RFQ, which is the first accelerator in the RFQ. This figure is taken from reference [9].

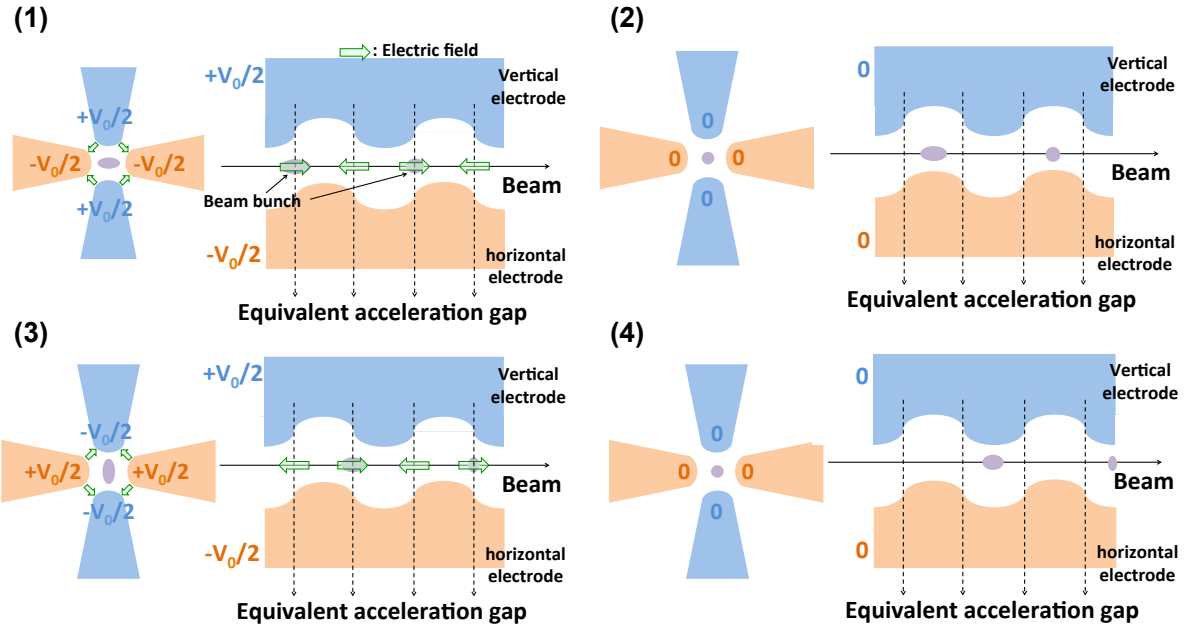

Figure B.10: Electric fields and the motion of the muons in the RFQ.

As for the transverse motion, the muons feel the quadrupolar electric field and focused transversely (figure B.10 (1)). The muons moving between acceleration gaps feel no transverse focusing force (figure B.10 (2) and (4)). When the muons go through the next acceleration gap, the polarity of the quadrupole is reversed. The muons feel the opposite quadrupolar electric field and are focused transversely along the opposite direction compared with that at the previous acceleration gap (figure B.10 (4)). As for the longitudinal motion, the muons feel the longitudinal electric field at the every acceleration gaps and are accelerated. The muons are bunched in the RFQ, since this longitudinal force is a restoring force.

The electric potentials are assigned to four electrodes in a quadrupolar-symmetric pattern and polarities of the potentials for the diagonal pair of the electrodes have the opposite sign each other. Then, the off-axis particles in the beam are focused transversely by the transverse electric field with the time evolution.

One of the advantages for the RFQ is the strong electric focusing in the low energy region. While the electric force is the velocity-independent, the magnetic force is the velocity dependent. Therefore, the electric focusing is stronger than the magnetic focusing lens, which is used in the conventional linac in the low β region. With introducing the RFQ, the input energy of the linac can be reduced and the length of the low β section in the linac can be short.

A spare RFQ of the J-PARC H^- linac, RFQII, will be used in the muon linac [89]. Figure B.11 shows the photograph of the RFQII. The RFQII was designed to accelerate the H^- from β =0.01 to 0.08. The resonant frequency of the RFQII is 324 MHz.

Table B.2 shows the comparison of parameters when the H^- and the muon are accelerated with the RFQII. When the muon is accelerated with the RFQII, the input and output energy of muons are calculated from the input and output β, those are 5.6 keV and 340 keV. The intervane voltage and the nominal power with the muon are scaled by a mass ratio and a squared mass ratio between the H^- and muon [24]. The phase-space distribution in the RFQII is simulated using

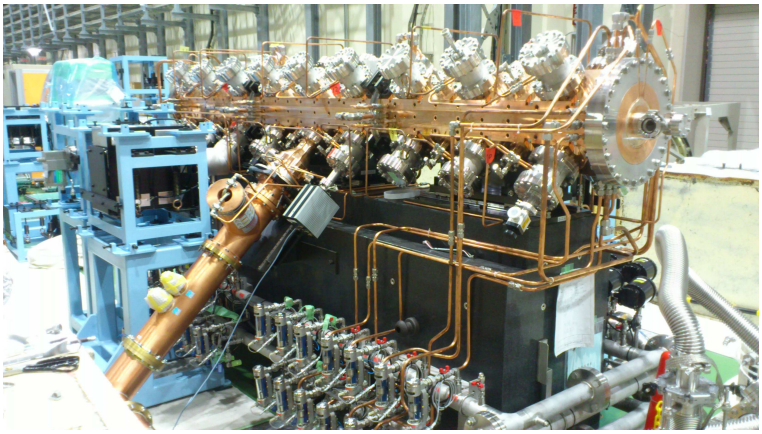

Figure B.11: Photograph of the RFQII. This figure is taken from reference [9].

PARMTEQM [55]. Figure B.12 shows the evolution of the phase-space distributions through the RFQII and simulated phase-space distributions at the exit of the RFQII. Table B.3 shows the result of the simulation for the USM using the RFQII. Normalized transverse and longitudinal rms emittances at the exit end of the RFQ are $\varepsilon_{n,rms,x} = 0.30\pi$ mm mrad, $\varepsilon_{n,rms,y} = 0.17\pi$ mm mrad and $\varepsilon_{n,rms,z} = 0.038\pi$ MeV deg, respectively.

Table B.2: Comparison of parameters when the H^- and the muon are accelerated with the RFQII.

Beam species	H^-	Muon
Mass [MeV/c^2]	939.3	105.7
Injection β	0.010	
Injection energy [keV]	50.0	5.6
Extraction β	0.080	
Extraction energy [MeV]	3.0	0.3
Intervane voltage [kV]	82.9	9.3
Nominal power [kW]	330	4.2

B.4.3 Low β section

The muon in the low β section is accelerated from 340 keV to 4.3 MeV. The short cavity is desired to reduce the decay loss of the muon, because the β is low. Therefore, an interdigital-H mode drift tube linac (IH-DTL) is utilized in the low β section. Figure B.13 shows the schematic of the IH-DTL cavity.

The IH-DTL was first proposed in 1956 [90]. The conventional Alvarez DTL excites the axial accelerating field with a TM010 mode and operates with 2π-mode. On the other hand, the IH-DTL operates with a TE110 mode, which doesn't have the axial acceleration field with the ordinary cylindrical cavity resonator as shown in figure B.14. If the interdigital structure is implemented in the cylindrical cavity, the axial accelerating field arises in the gap between the drift tubes as shown in the figure B.15. The operating with TE110 mode has the advantage of the effective acceleration with the π-mode and the short length of the cavity in the IH-DTL.

As for the transverse focusing, a quadrupole magnet is used in the conventional DTL. However, the implementation of the quadrupole magnet magnet increases the production cost and

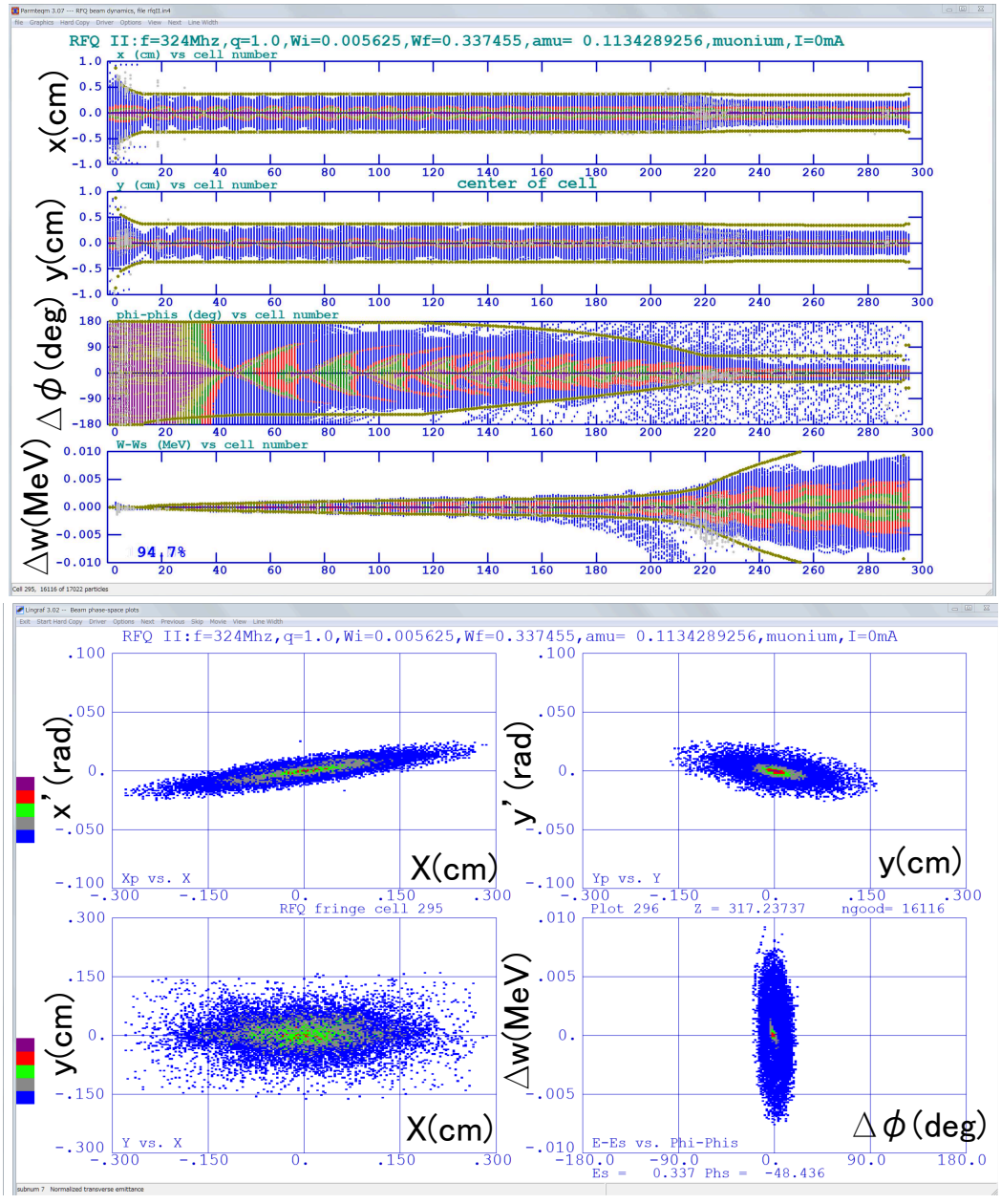

Figure B.12: Evolution of the phase space distributions through the RFQII (top) and phase-space distributions at the exit of the RFQII (bottom) simulated with PARMTEQM. These figures are taken from reference [9].

Table B.3: Result of the simulation for the USM using the RFQII. Parameters $\varepsilon_{n,rms,x}$, $\varepsilon_{n,rms,y}$ and $\varepsilon_{n,rms,z}$ describe normalized rms transverse and longitudinal emittances, respectively.

	Input	Output
$\varepsilon_{n,rms,x}$ [π mm mrad]	0.38	0.30
$\varepsilon_{n,rms,y}$ [π mm mrad]	0.11	0.17
$\varepsilon_{n,rms,z}$[π MeV $\cdot$ deg]	–	0.038
Transmission [%]	94.7	
Beam transit time [ns]	455	
Survival rate [%]	81.3	
Total transmission [%]	77.0	

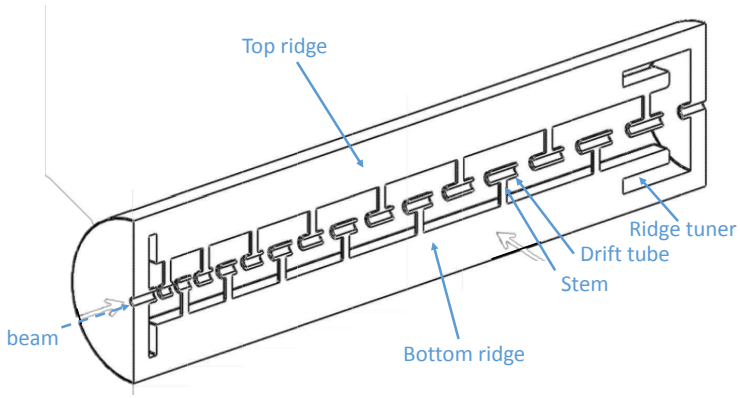

Figure B.13: Schematic of the IH-DTL cavity. This figure is taken from reference [9].

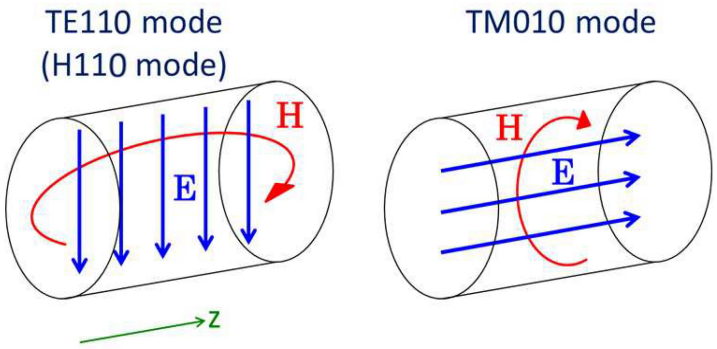

Figure B.14: TM010 mode and TE110 mode. This figure is taken from reference [9].

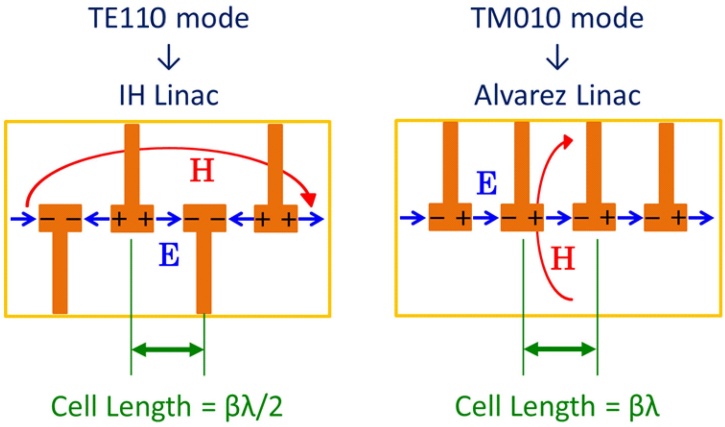

Figure B.15: Comparison of the electric and magnetic fields in the IH-DTL and the conventional Alvarez DTL. This figure is taken from reference [9].

decreases the shunt impedance. Therefore, the alternative phase focusing method (APF) is used to obtain the transverse focusing with reducing the production cost and without increasing the length of the cavity. When the synchronous phase is negative at the center of an accelerating gap, particles are focused longitudinally but defocused transversely. On the other hand, the synchronous phase is positive at the center of the gap, particles are focused longitudinally but defocused longitudinally. If the sign of the synchronous phase is changed periodically, the alternating-focusing forces are obtained in all directions without violating of the Earnshaw's theorem which is the incompatibility of the transverse and longitudinal focusing at the same time with the RF field.

Figure B.16 shows simulated phase-space distributions at the exit of the IH-DTL [91]. Table B.4 shows the result of the simulation for the IH-DTL using the output of the RFQII simulation. The total length of the cells is 1.29 m and the resonant frequency is 324 MHz. Normalized transverse and longitudinal rms emittances at the exit end of the IH-DTL are $\varepsilon_{n,rms,x} = 0.32\pi$ mm mrad, $\varepsilon_{n,rms,y} = 0.19\pi$ mm mrad and $\varepsilon_{n,rms,z} = 0.030\pi$ MeV deg, respectively. The quality factor and the shunt impedance are calculated to be 1.03×10^4 and 58 MΩ/m, respectively. The maximum surface field is also calculated to be 35.7 MV/m at the outer surface of the downstream drift tube. This value corresponding to less than 2.0 times the Kilpatrick limit [92] [93].

B.4.4 Middle β section

The muon is accelerated from 4.3 MeV to 40 MeV in the middle β section. The bi-periodic L-support disk-and-washer (DAW) coupled-cavity linac is utilized in this section [94] [95]. Figure B.17 shows the schematic of the DAW structure. A high shunt impedance and a large coupling between accelerating and coupling cells are obtained with the DAW structure. The large fabrication tolerance and field stability against the beam loading effects are obtained with the large coupling. The L-shape supports perpendicular to the electric field in the accelerating mode avoid the field distortion.

The accelerating cell and the coupling cell operate under the confluence condition, which is $f_a = f_c$, where f_a is the frequency of the accelerating mode and f_c is the frequency of the coupling mode. The electro-magnetic fields are stable at the confluence condition. The cell length and the cell geometry depend on β of the accelerated particle.

The cell designs were carried out for the typical velocities; β = 0.3, 0.4, 0.5 and 0.6. The cavities were designed to satisfy the confluence condition, maximize the shunt impedance and minimize the peak-to-average ratio of the electric field. Table B.5 shows parameters of the

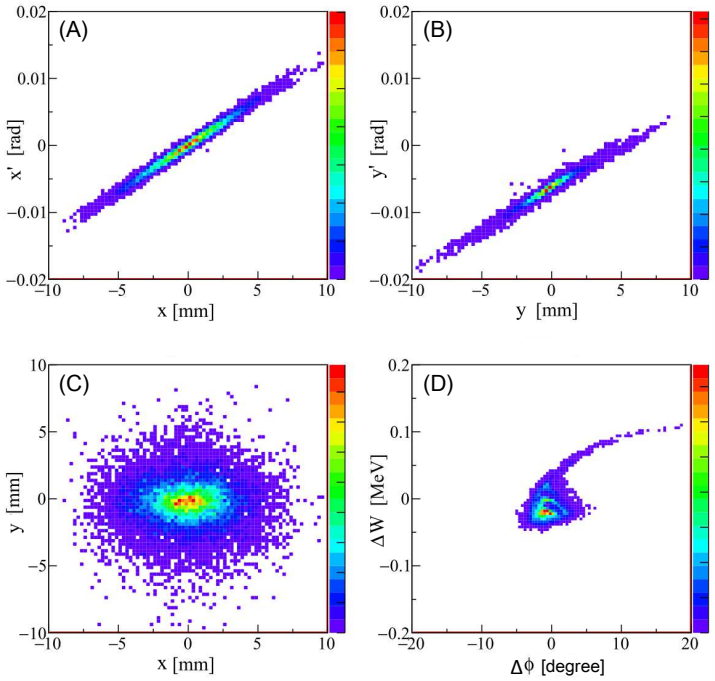

Figure B.16: Simulated phase-space distributions at the exit of the IH-DTL. (A) Horizontal divergence angle x′ vs x, (B) vertical divergence angle y′ vs y, (C) y vs x, and (D) difference of the kinetic energy ΔW(W − 4.5 MeV) vs difference of the phase $\Delta\phi$. This figure is taken from reference [9].

Table B.4: Result of the simulation for the IH-DTL using the output of the RFQII simulation.

	Input	Output
β	0.08	0.28
Energy [MeV]	0.34	4.3
ε_x [π mm mrad]	0.30	0.32
ε_y [π mm mrad]	0.17	0.19
ε_z [π MeV · deg]	0.018	0.030
Transmission [%]	99.9	
Beam transit time [ns]	25	
Survival rate [%]	98.9	
Total transmission [%]	98.7	
Quality factor	1.03×10^4	
Shunt impedance [MΩ/m]	58	
Operation power [kW]	320	
Maximum surface field [MV/m]	35.7	

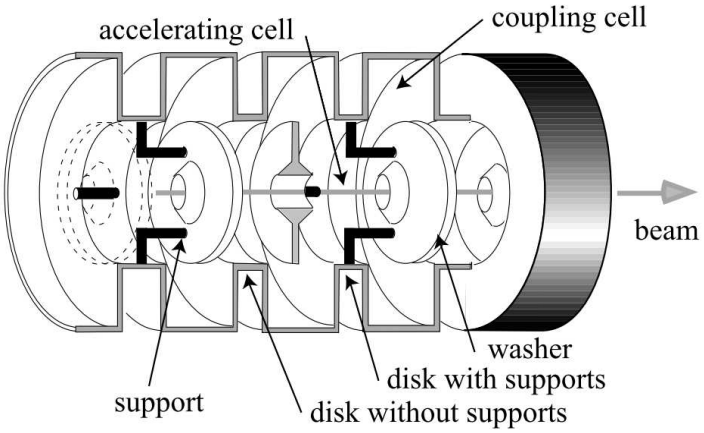

Figure B.17: Schematic of the cavity of the DAW. This figure is taken from reference [95].

cavities for the DAW using CST MW Studio [58]. Figure B.18 and table B.6 show simulated phase-space distributions at the exit of the DAW section and the result of the simulation for the DAW section, respectively, using PARMILA [60]. The total length of the DAW section is 16.3 m with 15 modules, which corresponds to 138 $\beta\lambda$. The resonant frequencies of the cavities are 1296 MHz. Normalized transverse and longitudinal rms emittances at the exit end of the DAW section are $\varepsilon_{n,rms,x} = 0.32\ \pi$ mm mrad, $\varepsilon_{n,rms,y} = 0.22\ \pi$ mm mrad and $\varepsilon_{n,rms,z} = 0.047\ \pi$ MeV deg, respectively.

Table B.5: Parameters of the cavities for the DAW in each β region. The f_a and the f_a are resonant frequencies of the accelerating cell and coupling cell, respectively.

β	0.6	0.5	0.4	0.3
f_a [GHz]	1.300	1.300	1.299	1.301
f_c [GHz]	1.299	1.301	1.302	1.301
Shunt impedance [MΩ/m]	57.8	46.3	33.8	18.0
Quality factor	2.91×10^4	2.41×10^4	1.91×10^4	1.42×10^4

B.4.5 High β section

A disk-loaded traveling wave accelerating structure (DLS) is used to accelerate muons from 40 MeV to 212 MeV in the high β section [96]. This DLS is a similar structure used in the electron linac. The advantage of the DLS is a high acceleration gradient of about 20 MV/m. The RF frequency is 1296 MHz, which is same as the DAW. Since the $2\pi/3$ mode is used for the DLS, the cell length is $\beta\lambda/3$. The DLS consists of four accelerating structures and total length of the high β section is 10 m. Figure B.19 shows simulated phase-space distributions at the exit of the DLS.

B.4.6 Summary of the beam dynamics simulation in the muon linac

The simulation results for the muon linac are simulated in this section. Figure B.20 shows the evolution of the transverse emittance in the muon linac. Table B.7 shows the summary of beam parameters in the the muon linac. The results of the simulations shows the good transmission in each section and the no serious emittance growth in the muon linac.

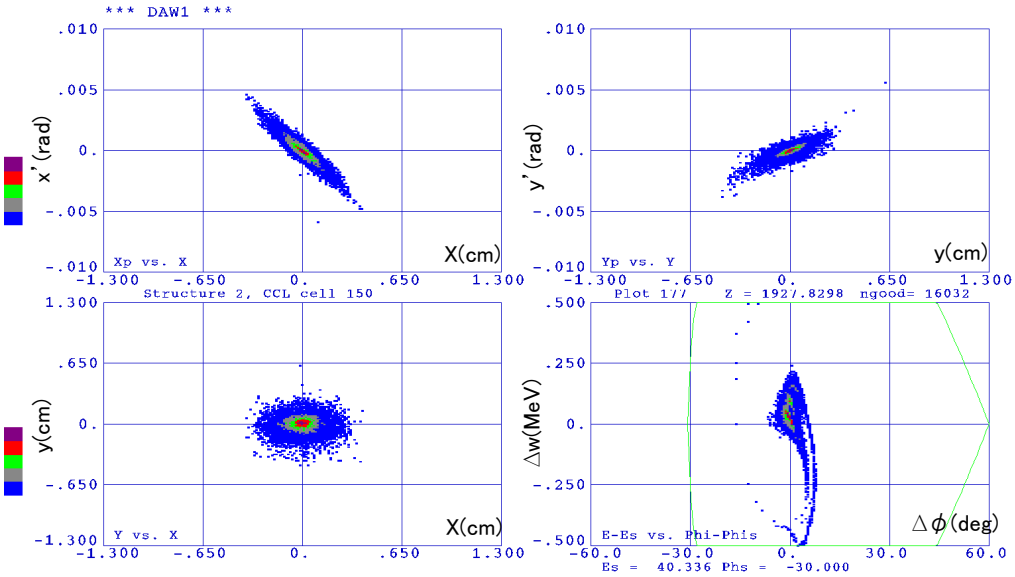

Figure B.18: Simulated phase-space distributions at the exit of the DAW using PARMILA [60]. This figure is taken from reference [9].

Table B.6: Result of the simulation for the DAW.

	Input	Output
β	0.28	0.68
Energy [MeV]	4.49	40.3
ε_x[π mm mrad]	0.32	0.32
ε_y[π mm mrad]	0.20	0.22
ε_z[π MeV $\cdot$ deg]	0.12	0.47
Transmission [%]	99.5	
Beam transit time [ns]	106	
Survival rate [%]	96.1	
Transmission total [%]	95.6	

Table B.7: Summary of beam parameters in the muon linac.

	Soa lens.	RFQ	IH-DTL	DAW	DLS
Transmission [%]	87	95	100	100	100
Decay loss [%]	17	19	1	4	1
$\varepsilon_{n,rms,x}$ [π mm mrad]	0.38	0.30	0.31	0.32	0.33
$\varepsilon_{n,rms,y}$ [π mm mrad]	0.11	0.17	0.20	0.21	0.21

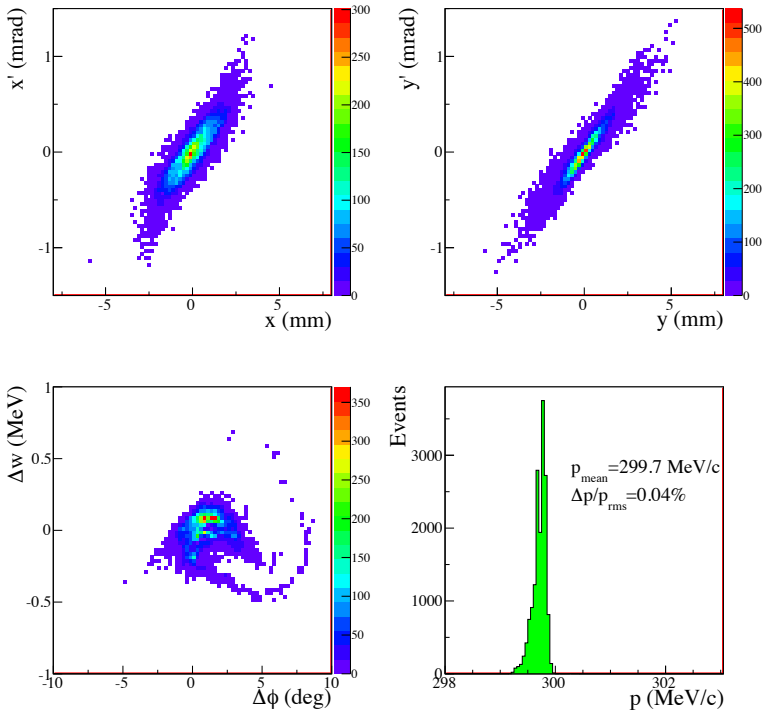

Figure B.19: Simulated phase-space distributions at the exit of the DLS.

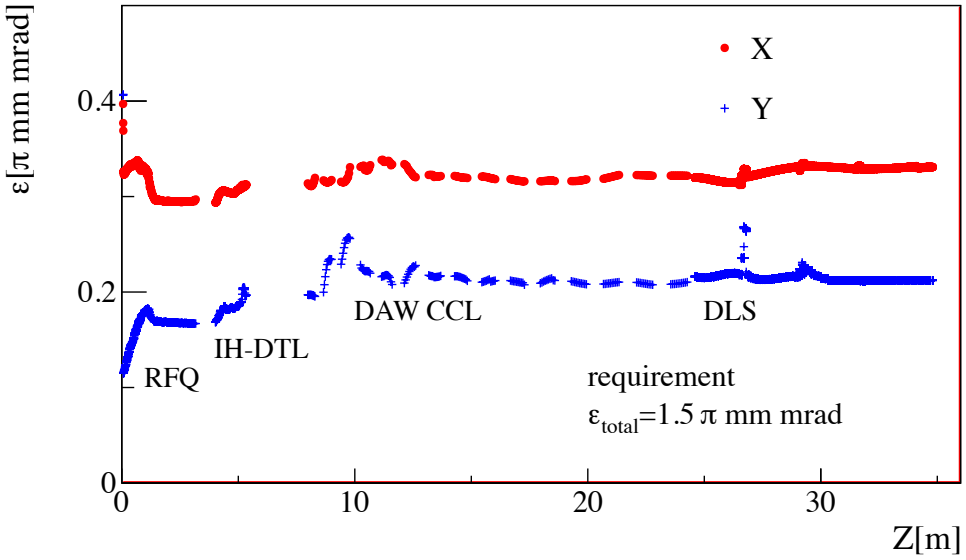

Figure B.20: Transverse emittance growth in the muon LINAC.

B.5 Injection and storage magnet

The accelerated muons are injected with a three-dimensional spiral injection system, which consists of a high-energy beam transport, a kicker system and a very-weak focusing system [97]. The very-weak focusing system is used to avoid the inappropriate oscillation of the muon trajectory for the precession measurement of the muon spin. Figure B.21 shows the schematic of the three-dimensional spiral injection system.

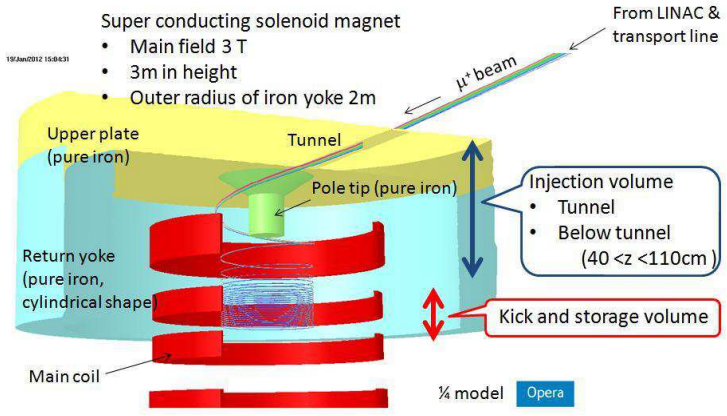

Figure B.21: Schematic of the three-dimensional spiral injection system. This figure is taken from reference [9].

The injected muons are stored in a storage ring. Figure B.22 shows the overview of the storage magnet and the detector. This storage ring uses an MRI-type super conducting magnet to obtain the uniform magnetic field of 3 Tesla [98]. This magnetic field can be controlled very precisely, because the diameter of the storage ring is smaller than that in the storage ring for the BNL E821 experiment. The noise level of the magnetic field will be less than 20 ppb in the operation. The amplitude of the electric field in the muon storage region should be smaller than 10 mV/cm to measure the ω_a with less than 0.1ppm [9].

B.6 Detector

The muons stored in the storage ring decay with the life time of 6.6 μs. Decay positrons from the stored muons are detected with a series of silicon strip detectors installed around the inner section in the storage ring [99]. Figure B.23 shows the schematic view of this decay positron detecter. The large silicon strip detector gives a large acceptance, a good time resolution and a good track-back ability with the high spacial resolution. The detector is highly segmented to reduce the pile-up at the beginning of the detection. In addition, the muon beam trajectory in the storage ring can be reconstructed from the track-back information of detected positrons. It contributes to reduce the uncertainty caused with the electric and magnetic field in the storage region. When the energy threshold cut over 200 MeV of detected positrons is used, the time distribution of the decay positrons is obtained. Figure B.24 shows the simulated time distribution of decay positrons. The ω_a is extracted from this time distribution.

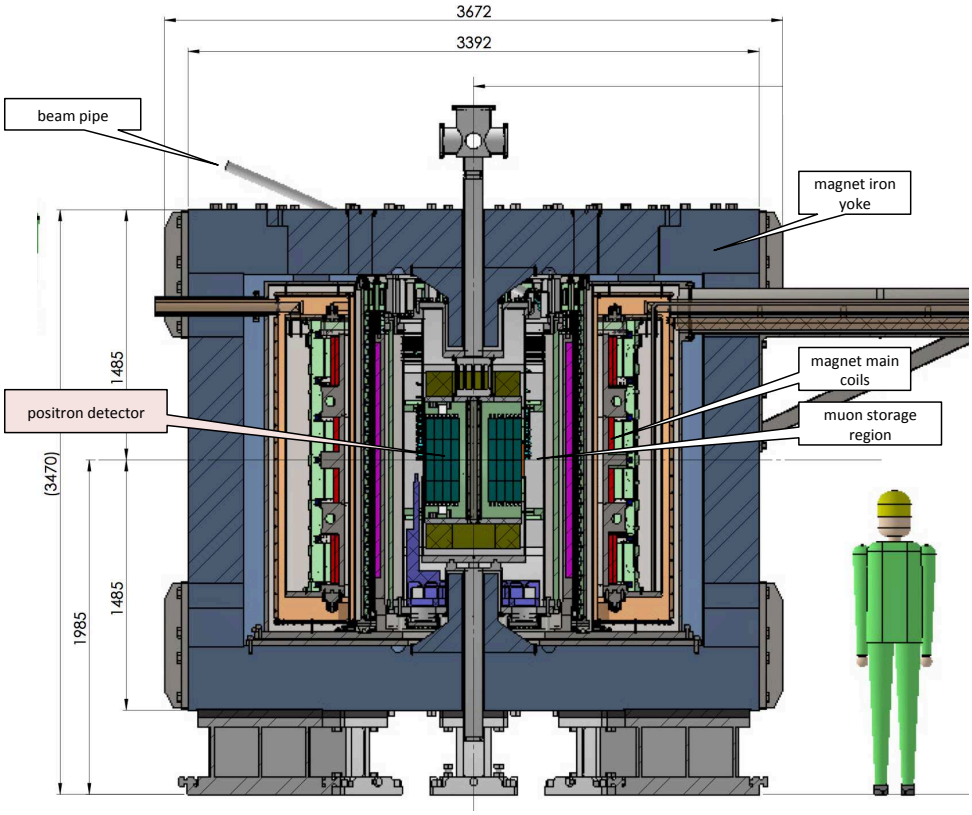

Figure B.22: Overview of the storage magnet and the detector. This figure is taken from reference [9].

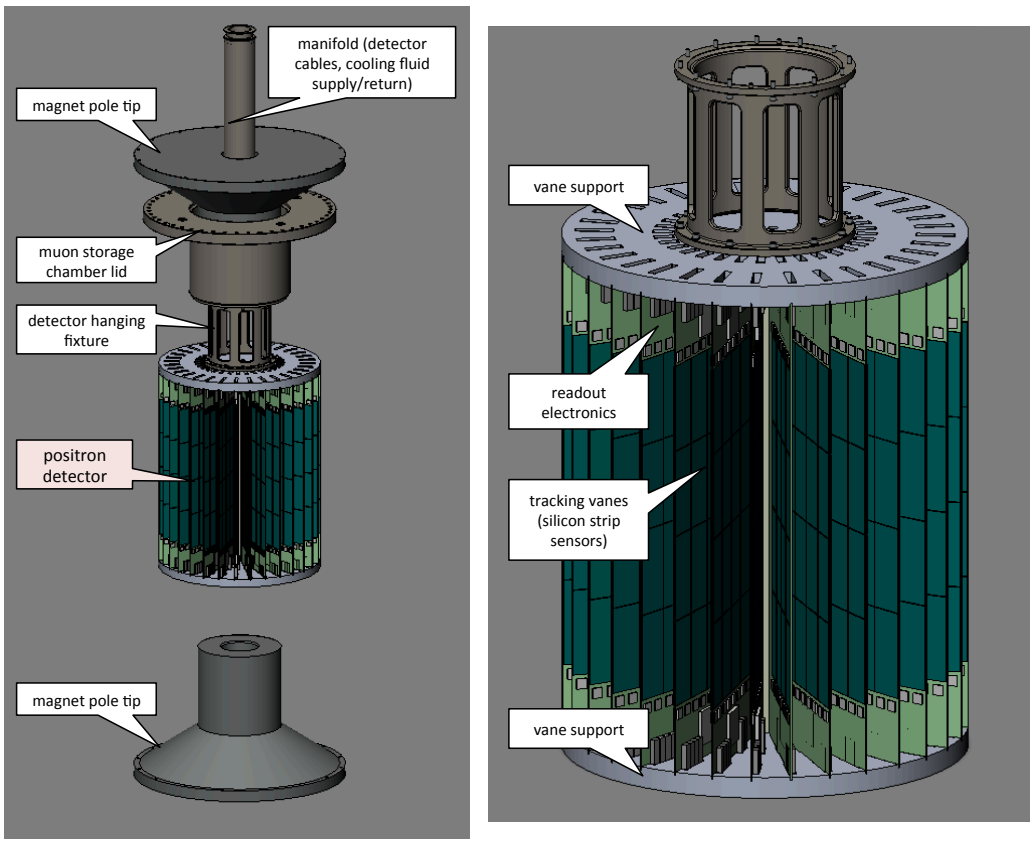

Figure B.23: Schematic view of the decay positron detecter. This figure is taken from reference [9].

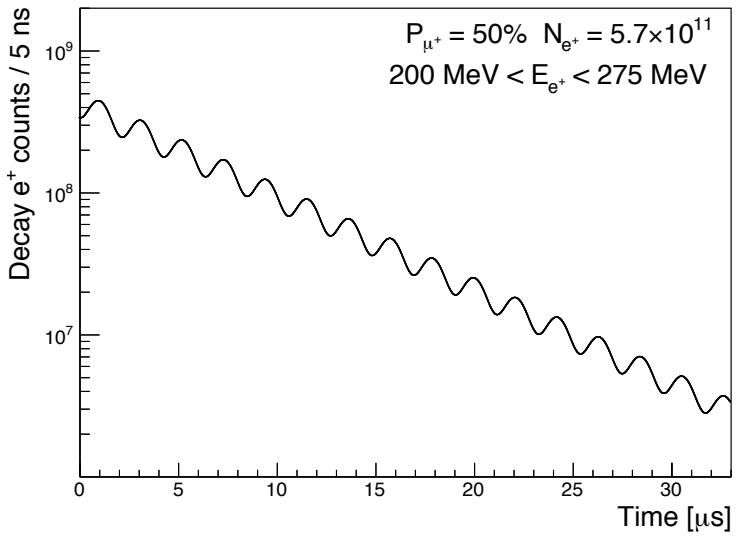

Figure B.24: Time distribution of decay positrons detected with silicon strip detectors for the J-PARC E34 experiment.

B.7 Comparison between the J-PARC experiment and BNL/FNAL experiments

The improved measurement of the BNL E821 experiment is ongoing in the Fermi National Laboratory (FNAL E989) [79]. The FNAL E989 experiment aims to measure the $(g-2)_\mu$ with the precision of 0.1 ppm. The principle of the measurement for the FNAL E989 experiment is same as that for the BNL E821 experiment. Therefore, the FNAL E989 experiment contains the same sources of the systematic uncertainties as those in the BNL E821 experiment. Since the systematic uncertainties of the J-PARC E34 experiment is completely different from these BNL/FNAL experiments, the J-PARC E34 experiment is important to confirm the discrepancy of the $(g-2)_\mu$. Table B.8 shows the comparison between the BNL E821, the FNAL E989 and the J-PARC E34 experiments. Goals of the sensitivities for the $(g-2)_\mu$ in both of the J-PARC and FNAL experiment are same, but their experimental conditions are quite different. Although the dominant limitation of the sensitivity for the $(g-2)_\mu$ in the BNL E821 experiment was the lack of the statistic, the understanding systematic uncertainties is very important to achieve the ultimate sensitivity of the measurement.

Table B.8: Comparison between the BNL E821, the FNAL E989 and the J-PARC E34 experiments.

	BNL-E821	FNAL-E989	J-PARC-E34
Muon momentum	3.09 GeV/c		0.3 GeV/c
γ	29.3		3
Polarization	100 %		50 %
Storage field	$B = 1.45$ T		$B = 3.0$ T
Focusing field	Electric quadrupole		Very-weak magnetic
Cyclotron period	149 ns		7.4 ns
Spin precession period	4.37 μs		2.11 μs
Statistical precision (a_μ)	0.46 ppm	0.14 ppm	0.46 ppm
Statistical precision (EDM)	0.9×10^{-19} e·cm	10^{-21} e·cm	10^{-21} e·cm

Appendix C

Commissioning with the H^- beam

C.1 Beam profile monitor

The measurement of the beam profile is necessary to tune the beam. A MCP-based beam profile monitor (BPM) was developed to measure the beam profile of the muon beam with the low energy region [100]. Figure C.1 shows the schematic of the BPM. When the muon enters the BPM-MCP, secondary electrons are produced. Secondary electrons are extracted with the potential gradient between the BPM-MCP and the phosphor screen, then strike the phosphor screen. The phosphor screen converts the output secondary electrons from the BPM-MCP into photons. The photon distribution is optically transported to the CCD sensor. Tables C.1 and C.2 show the specification of the BPM-MCP and the CCD camera (PCO1600) [101] for the BPM, respectively. The BPM-MCP has almost the same specification of the single-anode MCP. The position resolution of the BPM is 0.30 mm [100].

Table C.1: Specification of the BPM-MCP

Model of MCP assembly	F2225-21P308
MCP type	F1217-01
Thickness per plate (L) [μm]	480
Channel diameter (d) [μm]	12
Channel pitch [μm]	15
Channel length-to-diameter ratio (L/d=α)	40
Bias angle [degree]	8
Effective area [mm]	ϕ40
Number of stages	2
Typical gain (Min.)	1×10^6
Plate resistance per MCP [MΩ]	10$\sim$200
Dark count (Max.) [s^{-1}·cm^{-2}]	3
Operating vacuum pressure (Max.) [Pa]	1.3×10^{-4}
Open aperture ratio [%]	60
Phosphor screen	P47 (ITO)
10 % decay time [μs]	0.11
Peak emission wavelength [ns]	430

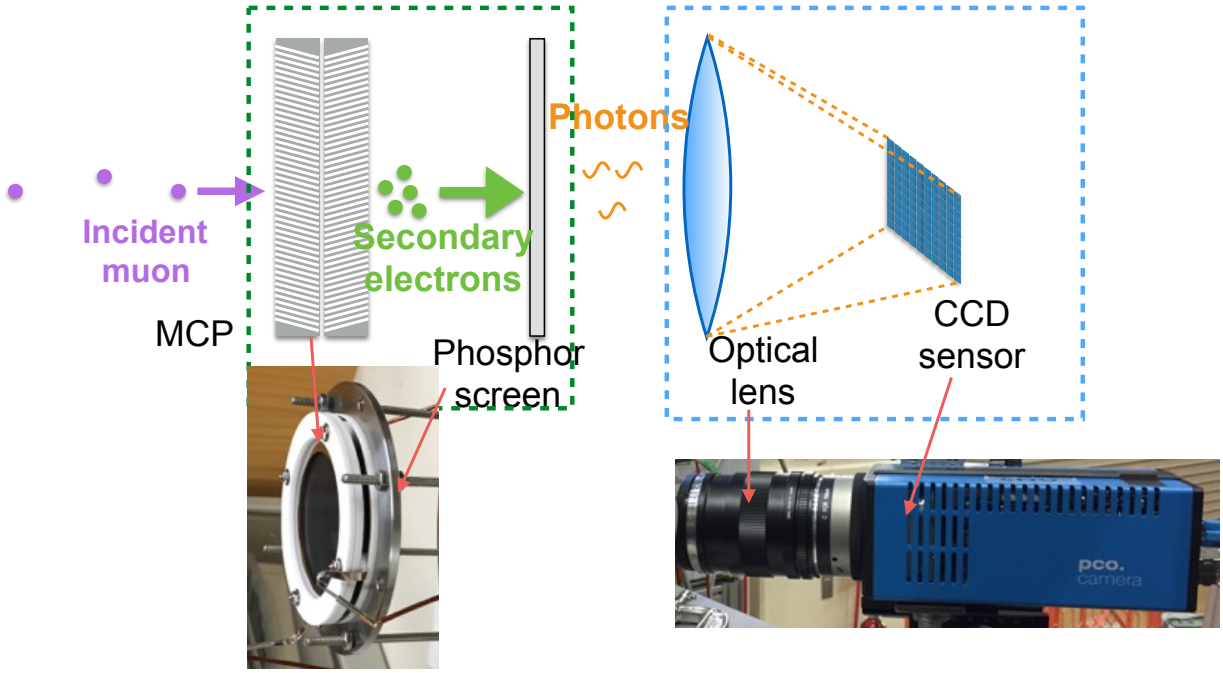

Figure C.1: Schematic of the BPM.

Table C.2: Specification of the CCD camera for the BPM.

Model	PCO1600
Image sensor	KAI-2001
Resolution	1600×1200 pixel (normal mode)
Pixel size	7.4 μm ×7.4 μm
Readout noise	17 e^- rms (40 MHz, typ.)
Dark count	0.01 e^-/pixel/s (-20 °C, typ.)
Exposure time (min.)	500 ns
Dynamic range A/D	14 bit
Number of A/D converters	2
Pixel scan rate	2×40 MHz
Binning (hor.×ver.)	2×2
Cooling method	Peltier cooler
Frame rate table	53.4 fps (2×2 binning, 2 A/D converters, 40 MHz)
Model of the optical lens	Distagon T* 2/28 ZF.2 (ZEISS)
Focal length	28 mm

C.1.1 Data acquisition system

In terms of the BPM, the CCD data is recorded with a commercial DAQ [101]. This raw data is converted to the two-dimensional histogram in the ROOT format using analysis codes. A cluster is defined to identify the signal. A single cluster region is defined as 9×9 pixels in which a pixel with the maximum ADC counts is the center of he signal. The signal cluster is identified by detecting 3×3 pixels with ADC counts above the primary threshold. Then, the signal is identified from the selected cluster using the maximum ADC counts of the pixel in the cluster. The typical threshold for the maximum ADC counts to identify the signal was set to be 1000 ADC counts.

C.2 Commissioning of the transport beam line with the H^- beam in the Mu^- production experiment

C.2.1 H^- source

The responses of the EQ3 and 4 and the beam transport in the transport beam line for the Mu^- production experiment were confirmed using the BPM and the H^- beam. The H^- beam is generated using the UV light. If the metal target is exposed to the UV light, the proton in the the residual material on the surface of the target is released as the H^-. The Xenon flash lamp module (Xe lamp, L9455-12 Hamamatsu photonics Co.) [102] was used to produce the UV light. Table C.3 shows the specification of the Xe lamp. The UV light is sent into the vacuum chamber through the optical fiber. Figure C.2 shows the schematic of the setup for the production of the H^- beam using the UV light. The output end of the optical fiber is fixed on the hole in the metal target. Figure C.3 shows the metal target plate made of the aluminum installed in the target holder. The produced H^- at the metal target plate is emitted through the hole with a diameter of 3 mm. These H^-'s are extracted with the Soa lens as the H^- beam.

Table C.3: Specification of the Xe flash lamp.

Model	L9455-12
Window material	UV grass
Emission wavelength range [nm]	185∼2000
Main discharge capacitor [μF]	0.11

C.2.2 Commissioning of the transport beam line

The beam axis of the Soa lens was aligned using a laser marker to fit the beam axis of the downstream apparatus before the tuning. The BPM was set at the straight section in the BM as shown in figure 2.2. The accelerating energies for the H^- beam were set to 7 keV and 14 keV as the typical settings. The EQ3 and the EQ4 were tuned in this commissioning . Figure C.4 shows the measured beam widths (rms) of the H^- beam for the y direction with changing voltages of the EQ3. Figures C.5 show the measured beam profiles of the H^- beam before and after tuning voltages of the EQ3 and EQ4. In figures C.5, the beam axis of the H^- beam was shifted for about 5 mm from the center of the BPM, due to the misalignment of the chamber. Table C.4 shows the best settings of the applied voltages with the 7 keV and 14 keV settings for the transport beam line to obtain the focused beam. Both of rms's of x and y were minimized in the best setting. From figures C.5, the beam profiles focused on the BPM after the tuning. As a result, the EQ3 and 4 were operated and the beam transport with the H^- beam was confirmed.

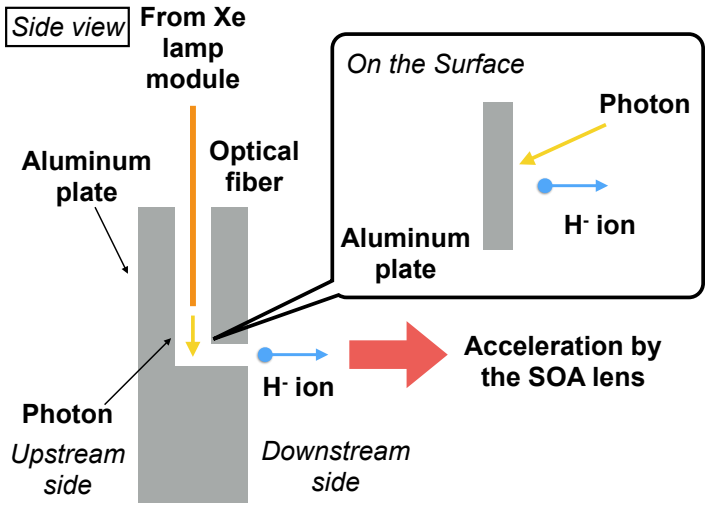

Figure C.2: Schematic of the setup for the production of the H^- beam using the UV light.

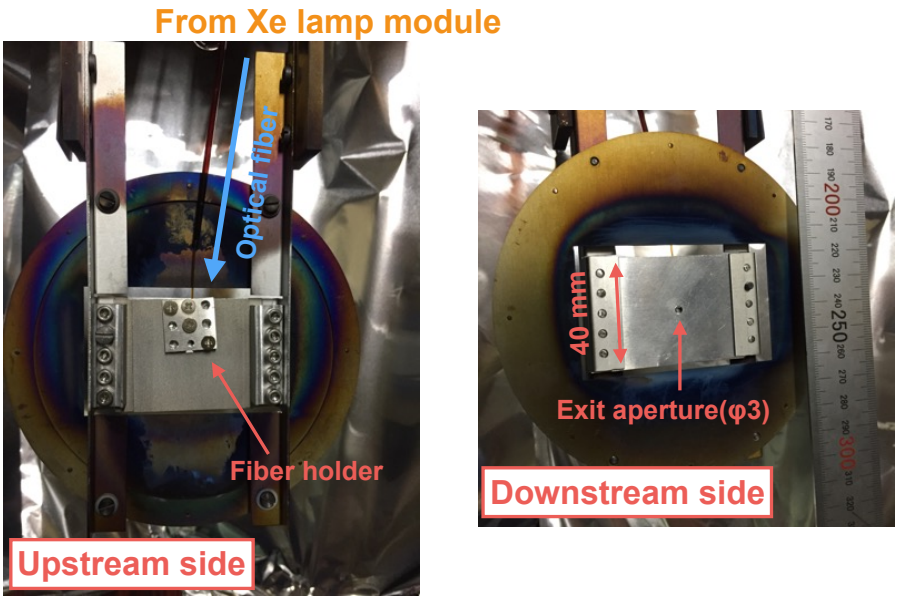

Figure C.3: Metal target plate to produce the H^- using the UV light.

Table C.4: The best settings of the applied voltages for the transport beam line. The polarity for the transport beam line was negative to transport the H^- beam.

Accelerating energy	7 keV	14 keV
T [kV]	7.0	14.0
S1 [kV]	6.8	13.7
S2 [kV]	6.7	13.4
S3 [kV]	6.1	12.1
ED [kV]	1.7	3.4
EQ1 [kV]	0	0
EQ2 [kV]	0	0
EQ3 [kV]	0.20	0.40
EQ4 [kV]	0.10	0.13

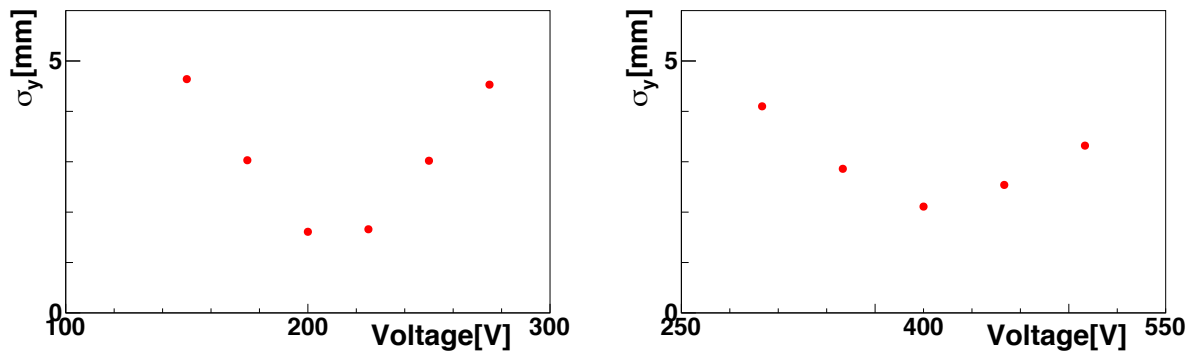

Figure C.4: Measured beam widths (rms) of the H^- beam for the y direction σ_y with changing voltages of the EQ3 when the accelerating energy is 7 keV (left) and 14 keV (right).

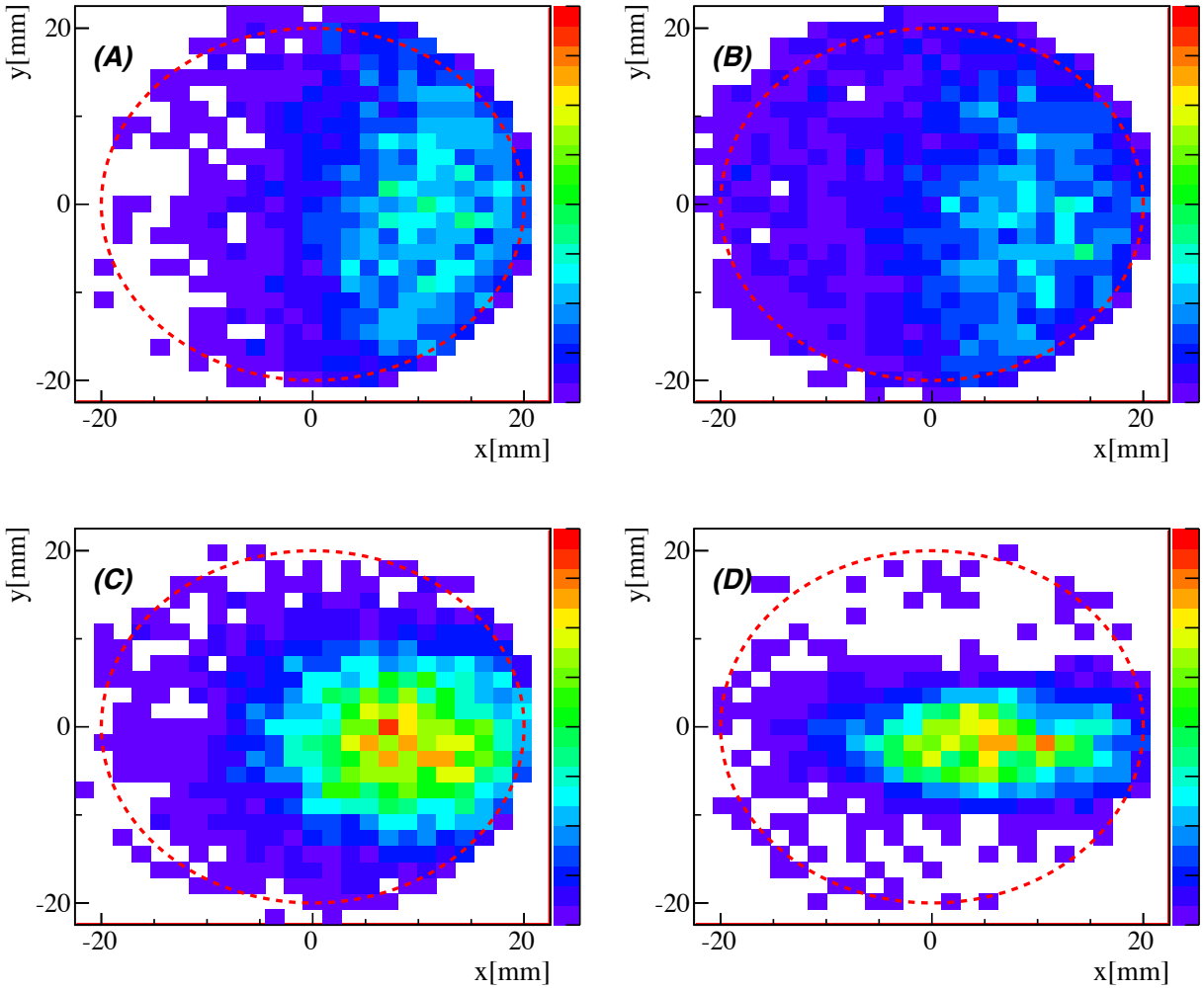

Figure C.5: Measured beam profiles of the H^- beam before and after tuning the transport beam line. (A) the beam profile with the 7 keV setting before the tuning, (B) the beam profile with the 14 keV setting before the tuning, (C) the beam profile with the 7 keV setting after the tuning (D) the beam profile with the 14 keV setting after the tuning. Red dotted circle shows the effective area of the MCP.

C.3 Commissioning of the diagnostic beam line with the H^- beam in the muon acceleration experiment

Since the event rate of the accelerated Mu^- is expected to be approximately 10^{-3} /s and the beam time is limited within a few days, it is quite difficult to tune the diagnostic beam line with the accelerated Mu^- beam. Therefore, the operation test of the diagnostic beam line was carried out using the H^- beam produced from the UV light before the muon acceleration experiment. The same Xe lamp module was used as shown in chapter 2. If the kinetic energy of the H^- is set to be 10 keV, the momentum of the H^- beam is equivalent to that of the accelerated Mu^-, that is 4.3 MeV/c. The applied voltage to the Soa lens was set to be 10 kV to accelerate the H^- beam to 10 keV. The H^- beam was tuned to come to the center of the BPM with changing the current to the BM. The applied currents of QM's were set to be zero. Since Twiss parameters of the H^- beam is different from those of the accelerated Mu^-, the applied currents of QM's are determined from the result of the simulation described in chapter 6. Figure C.6 shows the measured beam profile of the H^- with changing the applied current of the BM. The H^- beam was transported to the center of the BPM, when the applied current of the BM was 11.1 A in which the average of the horizontal position of the beam profile was minimized. The difference of the applied current between the measurement and the calculation using the effective length is 3 %. The current obtained from the measurement was used for the muon acceleration experiment.

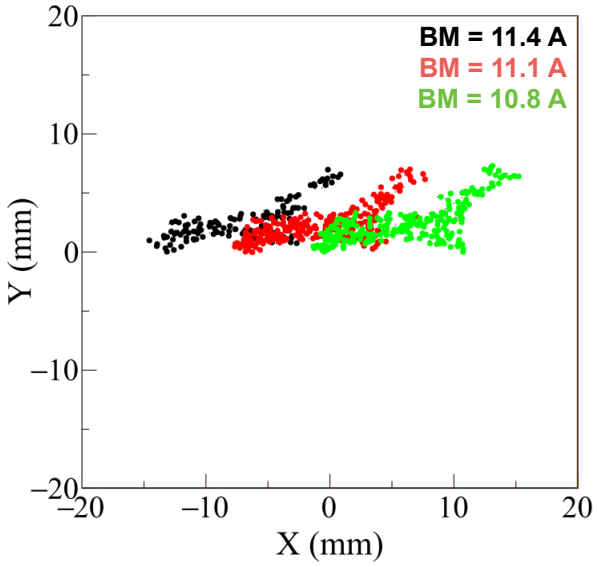

Figure C.6: Beam profiles of the H^- beam at the BPM after the BM. The momentum of the H^- was set to be 4.3 MeV/c.

Appendix D

Deceleration of the positive muon

D.1 Simulation of the deceleration for the μ^+

The deceleration of the μ^+ is simulated using musrSim [46], which is a simulation program for the μSR based on GEANT4. The incident surface muons penetrate the SUS foil window with a thickness of 50 μm, the Kapton degrader with a thickness of 150 μm, and the aluminum foil target as the Mu^- production target with a thickness of 200 μm, respectively, as shown in figure D.1. The incident surface muons are decelerated with these materials and some fractions of incident muons are converted to the Mu^-.

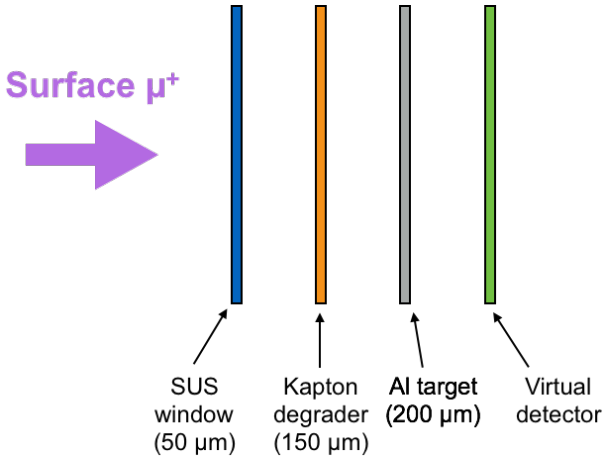

Figure D.1: Schematic of the deceleration simulation.

To generate a lot of events, the incident surface muons is generated at just upstream of the SUS foil window. The mean of the momentum of the generated μ^+'s is 25 MeV/c. The means of the beam position x and y are the center of the target. Sigmas of the momentum, x and y with the Gaussian are assumed to be 0.75 MeV/c, 19 mm and 27 mm, respectively, because the momentum bite in the D-line is 5 % (RMS) with 30 MeV/c and those of x and y are referred from the measurement [45]. The angle distributions x' and y' are assumed to be zero, because the multiple scattering dominates the angle distributions of the output beam.

The total number of generated events is 2.9×10^8. Figures D.2 and D.3 show the kinetic energy distribution of the decelerated μ^+'s less than 10 keV and the phase-space distributions of less than 2 keV, respectively. Figure D.4 shows the two-dimensional distribution of the kinetic energy w and the angle θ for the decelerated μ^+ with less than 10 keV in the deceleration simulation, where θ is the angle forms the momentum vector with respect to the beam axis. The decelerated μ^+ is defined a the μ^+ which has the energy less than 2 keV. These μ^+'s can be accelerated with

the RFQ in the acceleration experiment. The cooling efficiency of the decelerated μ^+ is defined as $\varepsilon_{\rm cool} = N_{{\rm LE}\mu}/N_{\rm gen}$, where $N_{{\rm LE}\mu}$ is the number of decelerated μ^+'s and $N_{\rm gen}$ is the number of generated events in the deceleration simulation. Since the number of the decelerated μ^+'s is 9.4×10^3 events, the cooling efficiency of the decelerated μ^+ is $\varepsilon_{\rm cool} = 3.2 \times 10^{-5}$.

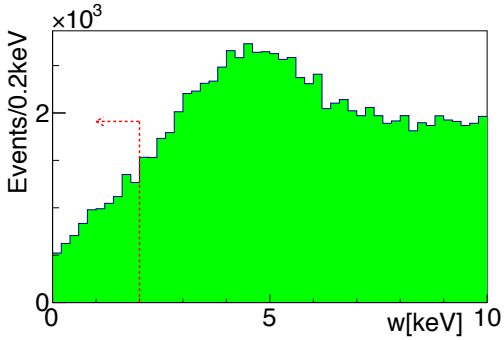

Figure D.2: Simulated kinetic energy distribution of the decelerated μ^+ with less than 10 keV after the deceleration. The number of events with less than 2 keV is used to evaluate the cooling efficiency of the μ^+ as indicated with the red dotted arrow.

Next, to save the computing time, the phase-space distribution of the decelerated μ^+'s for the subsequent beam transport simulation is regenerated from the result of the deceleration simulation. The kinetic energy w (i.e. the momentum) and the angle θ are generated to reproduce the two-dimensional distribution as shown in figure D.4. Figure D.5 shows the generated two-dimensional distribution of the kinetic energy w and the angle θ for the decelerated. The momentum vector are defined as

$$\begin{pmatrix} p_x \\ p_y \\ p_z \end{pmatrix} = \begin{pmatrix} p\sin\theta\cos\phi \\ p\sin\theta\sin\phi \\ p\cos\theta \end{pmatrix}, \tag{D.1}$$

where p is the generated momentum of the decelerated μ^+ and ϕ is the azimuthal angle. Here, ϕ is assumed to be uniform. Then, the angle distributions x′ and y′ are calculated from the momentum vector of the decelerated μ^+. The means and the sigmas of the positions x and y are same as those obtained with the deceleration simulation. The number of generated events is 1×10^6 events. Figure D.6 shows generated kinetic energy distribution of the decelerated μ^+. The events with less than 2 keV in figure D.6 are used for the beam transport simulation. Figure D.7 shows generated phase-space distributions of the decelerated μ^+ with less than 2 keV.

D.2 Beam transport simulation with the decelerated μ^+ in the Mu^- production experiment

The beam transport of the decelerated μ^+ is simulated using musrSim. Figures D.8 and D.9 show simulated phase-space distributions of the decelerated μ^+ at the MCP. Table D.1 shows the number of generated and detected events for the μ^+ in the beam transport simulation. From table D.1, the transport efficiency of the μ^+ is 5.7×10^{-3}. From the time distributions in figures D.8, the mean TOF of the decelerated μ^+ are 664.5 ns. Figure D.10 shows the transport efficiencies for the initial kinetic energy of the decelerated μ^+, when the kinetic energy distribution is uniform from 0 keV to 4 keV and assuming the position and angle distributions are those of the decelerated μ^+. From figure D.10, the muons with the initial kinetic energy of less than 2 keV can be transported with this transport beam line.

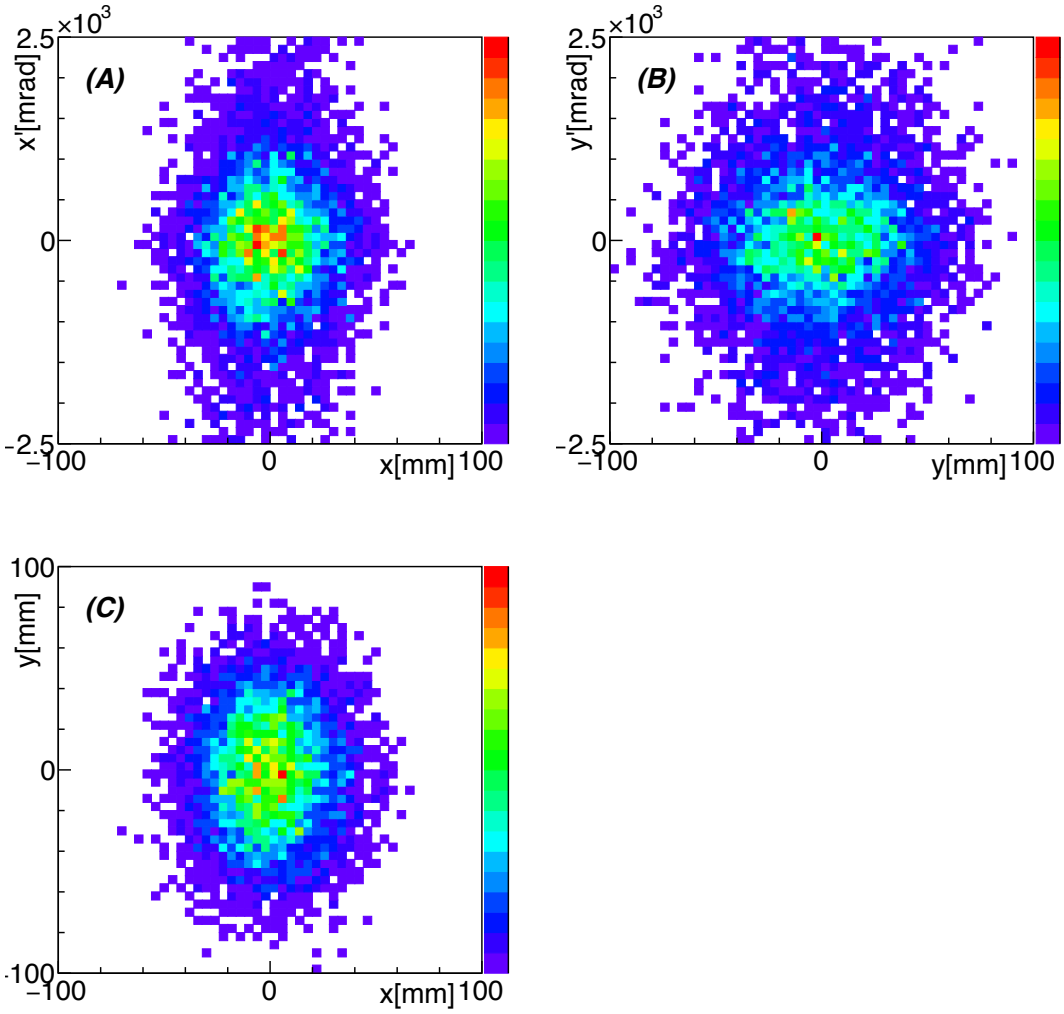

Figure D.3: Simulated phase-space distributions of the decelerated μ^+ with less than 2 keV after the deceleration. (A) the horizontal divergence angle x$'$ vs the horizontal position x, (B) the vertical divergence angle y$'$ vs vertical position y, and (C) y vs x.

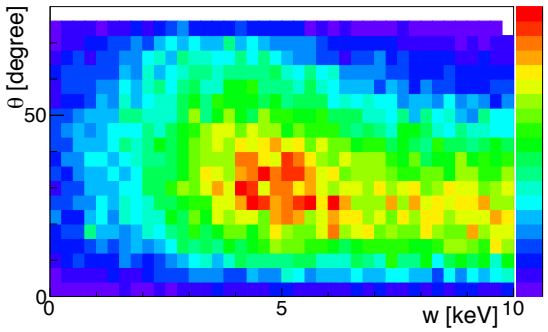

Figure D.4: Simulated two-dimensional distribution of the kinetic energy w and the angle θ for the decelerated μ^+ with the deceleration simulation. The angle θ is formed the momentum vector with respect to the beam axis.

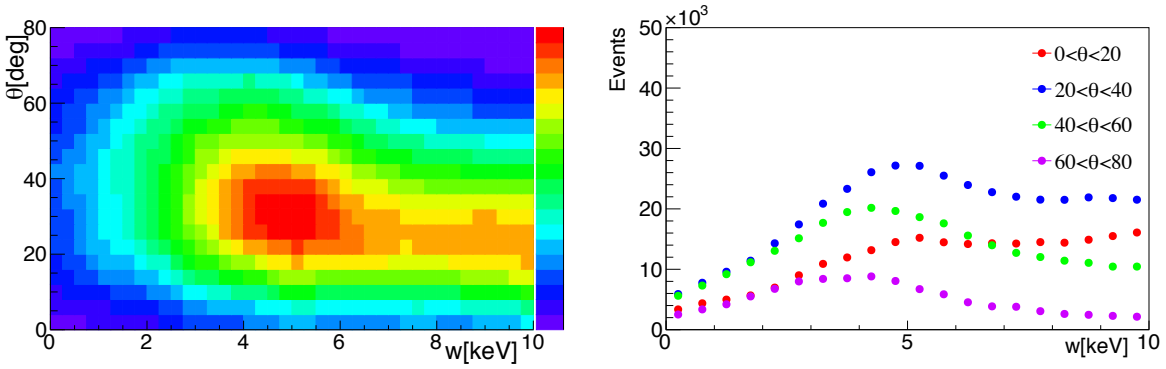

Figure D.5: Generated two-dimensional distribution of the kinetic energy w and the angle θ for the decelerated μ^+ with the deceleration simulation (left) and the kinetic energy distribution for each angle region (right). The angle θ is formed the momentum vector with respect to the beam axis.

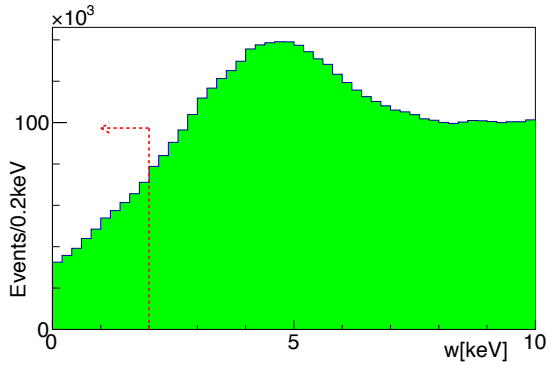

Figure D.6: Generated kinetic energy distribution of the decelerated μ^+ at the Mu^- production target. Events with less than 2 keV are used as indicated with the red dotted arrow.

Table D.1: Number of generated events and detected events for the μ^+ in the beam transport simulation.

N_{gen}	1×10^6
N_{det}	5699
Transmission	5.7×10^{-3}

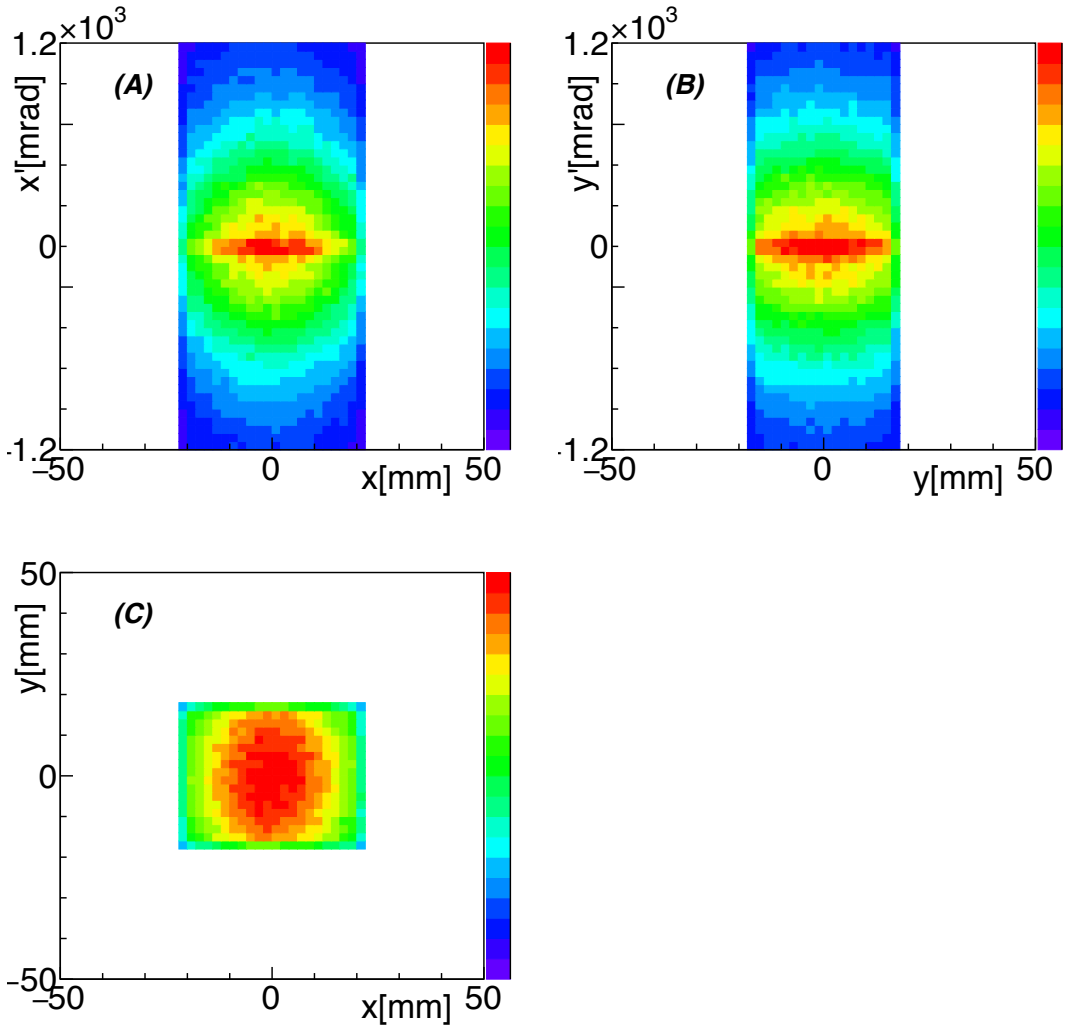

Figure D.7: Generated phase-space distributions of the decelerated μ^+ with less than 2 keV at the Mu^- production target. (A) the horizontal divergence angle x′ vs the horizontal position x, (B) the vertical divergence angle y′ vs vertical position y, and (C) y vs x.

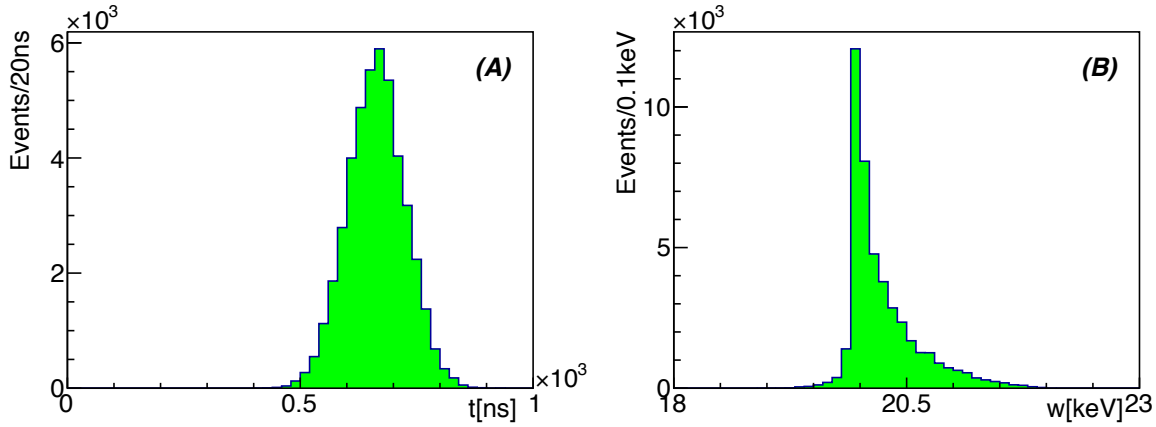

Figure D.8: (A) simulated time distribution t and (B) kinetic energy distribution w for the decelerated μ^+ at the MCP.

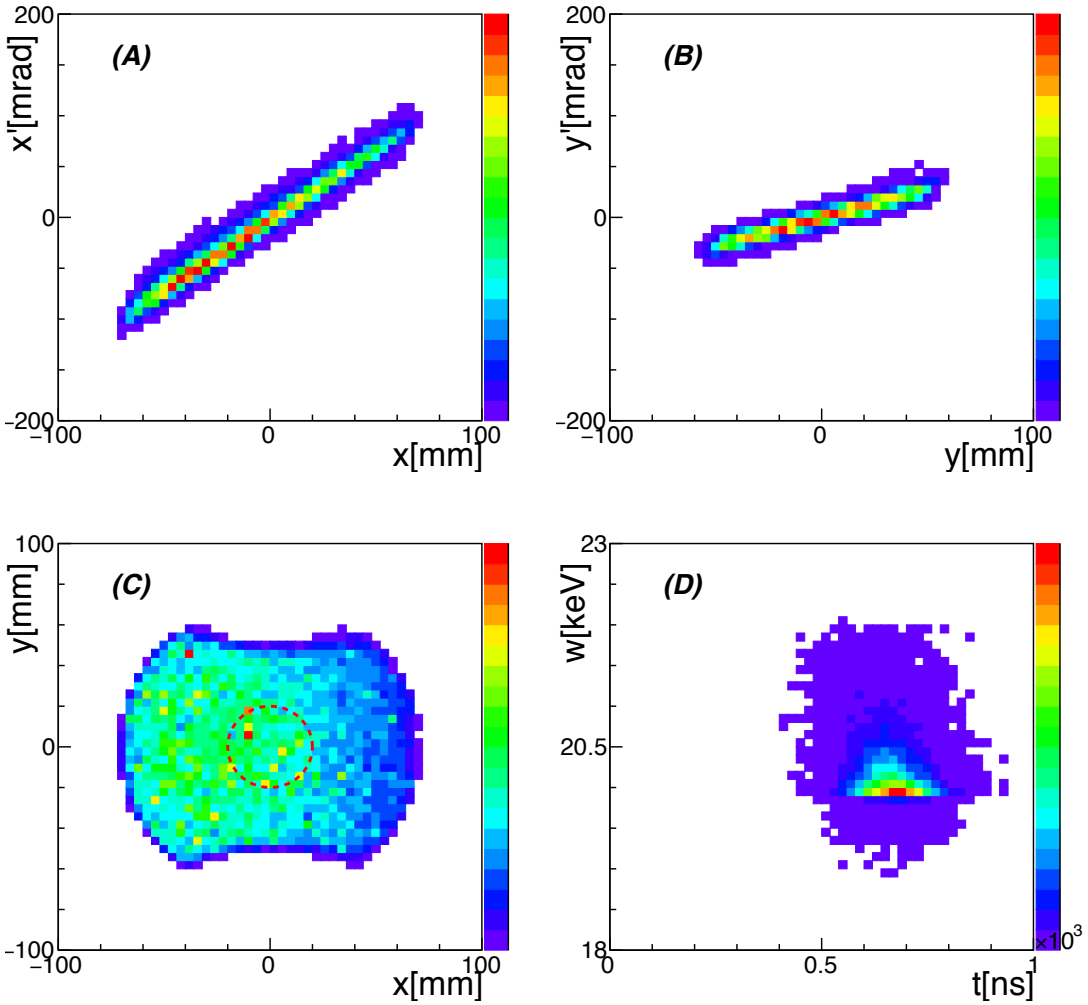

Figure D.9: Simulated phase-space distributions of the decelerated μ^+ at the MCP. (A) the horizontal divergence angle x′ vs the horizontal position x, (B) the vertical divergence angle y′ vs vertical position y, (C) y vs x, and (D) the kinetic energy distribution w vs the time distribution t. Red dotted circle in the x-y distribution shows the effective area of the MCP.

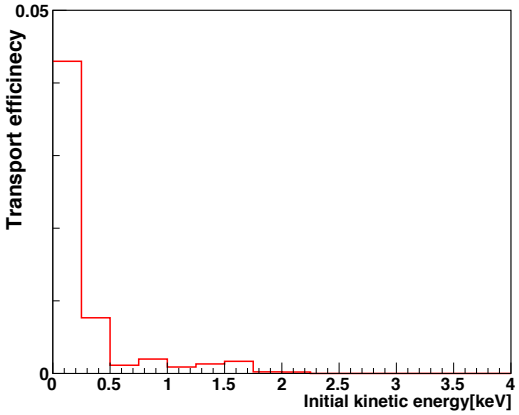

Figure D.10: Transport efficiency vs initial kinetic energy for the decelerated μ^+.

D.3 Result of the decelerated μ^+ in the Mu^- production experiment

From the fitting as described in section 4.3, the number of the signal events for the decelerated μ^+ is evaluated to be 128.7 ± 13.6 events, taking into account the selection efficiency of the pulse height cut. The total number of the triggers for the positive extraction is 6.5×10^5. Therefore, the measured event rate of the decelerated μ^+ is $(5.0 \pm 0.5) \times 10^{-3}$ /s.

List of Tables

List of Figures

Bibliography

[1] Y. Kuang *et al.*, Phys. Rev., A **35**, 3172 (1987).

[2] Y. Kuang, Ph.D. thesis, College of William and Mary (1989).

[3] S.Bae *et al.*, Phys. Rev. Accel. Beams, **21** 050101 (2018).

[4] K. Horigane *et al.*, Phys. Rev. B. **97** (2018) 064425(1-8).

[5] K. Ninomiya *et al.*, J. Radioanal. Nucl. Chem. 316 (2018) 1107-1111.

[6] K. Nagamine and E. Torikai, J. Phys.: Condens. Matter **16** S4797 (2004).

[7] C. L. Morris *et al.*,Science and Global Security, 16:pp.37–53 (2008).

[8] K. Nagamine, Proc. Jpn. Acad., Ser. B **92** No.8 pp.265–289(2016).

[9] T. Mibe and edit., J-PARC E34 Conceptual Design Report, Technical Design Report (KEK, 2011).

[10] Mohammad M. Alsharo ' a *et al.*, Phys. Rev. STAB, **6**, 081001 (2003).

[11] R. B. Palmer, Rev. Accl. Sci. Tech., **07**, 137 (2014).

[12] G. Aad *et al.* [ATLAS Collaboration], Phys. Lett. B **716**, 1 (2012) [arXiv:1207.7214 [hep-ex]].

[13] S. Chatrchyan *et al.* [CMS Collaboration], Phys. Lett. B **716**, 30 (2012) [arXiv:1207.7235 [hep- ex]].

[14] K. Hagiwara, R. Liao, A. D. Martin, D. Nomura and T. Teubner, J. Phys. G **38**, 085003 (2011) [arXiv:1105.3149 [hep-ph]].

[15] G.W. Bennett *et al.*, Phys. Rev. D **73**, 072003 (2006).

[16] F. Hoogeveen, Nucl. Phys. B **341** pp.322–340 (1990).

[17] B. L. Roberts, J. Phys. Soc. Jpn. **76**, 111009 (2007).

[18] G.W. Bennett *et al.*, Phys. Rev. D **80**, 052008 (2009).

[19] MICE collaboration, http://mice.iit.edu.

[20] M. Bogomilov *et al.*, Phys. Rev. ST Accel. Beams. **20**, 063501 (2017).

[21] R. C. Fernow and 3. C. Gallardo, Phys. Rev. E **52**, 1,1039 (1995).

[22] D. Neuffer, AIP Conf. Proc., **156**, 201 (1987).

[23] K. Nagamine *et al.*, Phys. Rev. Lett. **74**, 4811 (1995).

[24] Thomas P. Wangler,"*RF Linear Accelerators* ", 2008, Wiley-VCH Verlag GmbH & Co.

[25] I. M. Kapchinkiy and V. A. Teplyakov, "Linear Ion Accelerator with Spatially Homogeneous Strong Focusing", Prib. Tech. Eksp., **2**, 19-22 (1970).

[26] P. Bakule *et al.*, NIM B **266**, 355 (2008).

[27] *MCP ASSEMBLY* technical information, TMCP9002J02, HAMAMATSU Photonics Co (2007).

[28] W. Higemoto *et al.*, Quantum Beam Sci., **1**, 11 (2017).

[29] K. F. Canter, P. H. Lippel, W. S. Crane, and A. P. Mills Jr., "Positron studies of solids, surfaces and atoms " (World Scientific, Singapore, 1986) p.199.

[30] E. A. Soa, Janaer Jahrbuch, **1**, 115 (1959).

[31] J. E. Simpson and K. E. Kuyatt, Rev. Sci. Inst. **34**, 265 (1963).

[32] R. Kitamura, Master thesis, The Univ. of Tokyo (2015).

[33] *MCP assembly F9892-21/-22* data sheet, TMCP1037E01, HAMAMATSU Photonics Co (2009).

[34] *MCP(microchannel plate) and MCP assembly* reference document, TMCP0002J04, HAMAMATSU Photonics Co. (2016).

[35] ROOT, https://root.cern.ch.

[36] CAEN 2014 Product catalog, pp.64–67 (2014).

[37] CAEN Mod. V1720 *8 CHANNEL 12 BIT 250 MS/S DIGITIZER* technical information manual, revision no.26 (2014).

[38] EPICS,http://www.aps.anl.gov/epics/

[39] Spellman High Voltage Corporation, *High voltage reference manual SL series* (2000).

[40] G4beamline, http://public.muonsinc.com/Projects/ G4beamline.aspx

[41] Geant4, http://geant4.cern.ch/

[42] P. A. Piroue and A. J. S. Smith, Phys. Rev. **148**, 1315 (1966).

[43] Particle Data Group, http://pdg.lbl.gov/2017/reviews/rpp2017-rev-passage-particles-matter.pdf.

[44] M. Gonin, R. Kallenbach and P. Bochsler, Rev. Sci. Instrum. **65** 648(1994).

[45] S. Kanda, private communication.

[46] musrSim, https://www.psi.ch/lmu/geant4-simulations

[47] OPERA 3D Software for electro-magnetic design by Vector Field.

[48] G. Cowan, Statistical Data Analysis, Oxford University Press (1998).

[49] F. James., MINUIT function minimization and error analysis–reference manual, version 94.1, CERN Program Library Long Writeup D506, https://root.cern.ch/download/minuit.pdf

[50] Y. Kondo, K. Hasegawa, and A. Ueno, in *Proceedings of LINAC2006* (Knoxville, Tennessee USA, 2006) pp. 749–751.

[51] J.H.BillenandL.M.Young, "POISSON SUPERFISH ", LA-UR-96-1834 (1996).

[52] M. Reiser, Theory and Design of Charged Particle Beams (Wiley, New York, 1994), p.89.

[53] Y. Nakazawa, Graduation thesis, Ibaraki university (2018).

[54] High-intensity Proton Accelerator Project Team, "*Accelerator technical design report for High-intensity Proton Accelerator Facility Project, J-PARC*", JAERI-Tech 2003-044 (2003).

[55] K. R. Crandall *et al.*, "RFQ Design Codes ", LA-UR-96-1836 (1996).

[56] General Particle Tracer, Pulsar Physics. http://www.pulsar.nl/gpt/

[57] Autodesk Inventor, https://www.autodesk.co.jp/products/inventor/overview.

[58] CST Studio Suite, Computer Simulation Technology (CST), https://www.cst.com/products/cstems.

[59] K. R. Crandall and D. P. Rusthoi, "Trace 3-D Documentation ", LA-UR-97-886 (1997).

[60] H. Takeda, "*Parmila* ", LA-UR-98-4478 (1998).

[61] K. W. Ehlers and K. N. Leung, Rev. Sci. Instrum., **51**, 721 (1980).

[62] N. Kawamura *et al.*, Journal of Phys.: Conf. Series **408** 012072 (2013).

[63] Y. Kondo *et al.*, FRXGBF1 in *Proc. of IPAC2018*, Vancouver, BC, Canada (2018).

[64] Peter J. Mohr, Barry N. Taylor, and David B. Newell, Rev. Mod. Phys. **84**, 1527 (2012)).

[65] K.A. Olive *et al.* (Particle Data Group), Chin. Phys. **C38**, 090001 (2014) (URL: http://pdg.lbl.gov).

[66] T. Aoyama, M. Hayakawa, T. Kinoshita and M. Nio, Phys. Rev. Lett. **109**, 111808 (2012) [arXiv:1205.5370 [hep-ph]].

[67] R. Bouchendira, P. Clade, S. Guellati-Khelifa, F. Nez and F. Biraben, Phys. Rev. Lett. **106**, 080801 (2011) [arXiv:1012.3627 [physics.atom-ph]].

[68] A. Czarnecki, W. J. Marciano and A. Vainshtein, Phys. Rev. D **67**, 073006 (2003) [Erratum-ibid. D **73**, 119901 (2006)] [hep-ph/0212229].

[69] C. Gnendiger, D. Stöckinger and H. Stöckinger-Kim, Phys. Rev. D **88**, 053005 (2013) [arXiv:1306.5546 [hep-ph]].

[70] V. Golubev, talk at the 13th International Workshop on Tau Lepton Physics (Tau 2014).

[71] A. Denig [BESIII Collaboration], arXiv:1412.2951 [hep-ex].

[72] A. Kurz, T. Liu, P. Marquard and M. Steinhauser, Phys. Lett. B **734**, 144 (2014) [arXiv:1403.6400 [hep-ph]].

[73] K. Hagiwara, A. D. Martin, D. Nomura and T. Teubner, Phys. Rev. D 69, 093003 (2004) [hep- ph/0312250].

[74] J. Prades, E. de Rafael and A. Vainshtein, (Advanced series on directions in high energy physics. 20) [arXiv:0901.0306 [hep-ph]].

[75] G. Colangelo, M. Hoferichter, A. Nyffeler, M. Passera and P. Stoffer, Phys. Lett. B **735**, 90 (2014) [arXiv:1403.7512 [hep-ph]].

[76] T. Blum, A. Denig, I. Logashenko, E. de Rafael, B. Lee Roberts, T. Teubner and G. Venanzoni, arXiv:1311.2198 [hep-ph].

[77] Particle Data Group, http://pdg.lbl.gov/2013/reviews/rpp2013-rev-g-2-muon-anom-mag-moment.pdf.

[78] A. Czarnecki and W. J. Marciano, Phys. Rev. D **64**, 013014 (2001).

[79] J. Grange *et al.*, arXiv:1501.06858v1 (2015).

[80] A. D. Sakharov, JETP Lett. **5**, 24 (1967).

[81] M. Kobayashi and T. Maskawa, Prog. Theor. Phys. **49**, 652 (1973).

[82] W.C. Griffith, *et al.*, Phys. Rev. Lett. **102**, 101601 (2009).

[83] C.A. Baker, *et al.*, Phys. Rev. Lett. **97**, 131801 (2006).

[84] J. Baron *et al.*, Science, **343** 6168, pp.269–272 (2013).

[85] M. J. Booth, arXiv:hep-ph/9301293.

[86] W. Liu *et al.*, Phys. Rev. Lett. **82**, 711 (1999).

[87] The Particle Data Group: D.E. Groom *et al.*, The European Physical Journal **C15**, 1 (2000).

[88] G.A. Beer *et al.*, Prog. Theor. Exp. Phys. 2014 (2014) 091.

[89] Y. Kondo *et al.*, High-power test and thermal characteristics of a new radio frequency quadrupole cavity for the japan proton accelerator research complex linac, Phys. Rev. ST Accel. Beams, **16** 040102(2013).

[90] J.P. Blewett, Symposium du CERN sur les Accelerateurs de Haute Enegie et la Physique des Mesons π v.1, Regenstreif and Edouard (CERN, 1956), p.162.

[91] M. Otani *et al.*, Phys. Rev. Accel. Beams **19**, 040101 (2016).

[92] W. D. Kilpatrick, Criterion for vacuum sparking designed to include both rf and dc, Rev. Sci. Instrum. **28**, 824 (1957).

[93] T. J. Boyd Jr., Los Alamos Group AT-1 Report No. AT- 1:82-28, 1982.

[94] M. Otani *et al.*, PASJ2014-SAP039 (2014).

[95] H. Ao *et al.*, Jpn. J. Appl. Phys., **39**, pp.651–656 (2000).

[96] Y. Kondo *et al.*, Proc. of the 14th annual meeting of PASJ, Sapporo, Japan, TUP036(2017).

[97] H. Iinuma *et al.*, Nuclear Inst. and Methods in Physics Research, A **832** pp.51–62 (2016).

[98] M. Abe *et al.*, Nuclear Inst. and Methods in Physics Research, A **890** pp.51–63 (2018).

[99] S. Nishimura *et al.*, JPS Conf. Proc. **8**, 025015 (2015).

[100] B. Kim *et al.*, Nuclear Inst. and Methods in Physics Research, A 899 (2018) 22–27.

[101] pco. 1600, https://www.pco.de/specialized-cameras/pco1600/

[102] *5W Xenon flash lamp modules*,TLSZ1006E04/J07, HAMAMATSU Photonics Co. (2015).